

# **Optimization of Phase-Engineered a-Si:H-based Multi-junction Solar Cells**

**C. R. Wronski, R. W. Collins,  
G. M. Ferreira, J. M. Pearce, J. Deng,  
V. Vlahos, C. Chen, A. Lawrence**

**Center for Thin Film Devices  
The Pennsylvania State University  
University Park, PA 16802**

**Final Technical Status Report  
January 2002 – April 2003**

**Subcontract No. NDJ-1-30630-01**

**NREL Technical Monitor: Bolko von Roedern**

## Table of Contents

1. Table of Contents .....	2
2. Executive Summary .....	3
Task 1.....	3
Task 2.....	4
Task 3.....	6
Task 4.....	8
3. Task 1.....	10
Multi-step i layer.....	10
n-i-p Solar Cell Structures .....	10
Equivalence between p-i-n and n-i-p Cell Structures .....	14
Figures 2 – 10.....	15
4. Task 2.....	21
Process Deposition Phase Diagrams for the Optimization of a-Si:H-Based .....	21
Materials and Solar Cells .....	21
Overview.....	22
Amorphous Roughening Transition During Film Growth.....	24
Crystalline Silicon Wafers and Amorphous Silicon Film Substrates .....	26
Optimization Principles for Optimum Solar Cell Fabrication .....	27
Figures 11 – 17.....	29
5. Task 3.....	36
Device Loss Mechanisms .....	36
1 Sun Open Circuit Voltage Characteristics .....	42
Correlations between Solar Cell and Thin Film a-Si:H Properties.....	42
Figures 18 – 32.....	45
6. Task 4.....	60
Novel Analysis of RTSE applied to Amorphous-to-Microcrystalline Phase Transition Region.....	60
Analysis of the Evolution of (a+ $\mu$ c)-Si:H films.....	60
Devices Comparisons.....	62
Phase Diagrams for p-Type Doped Si:H Films .....	63
New Dual Beam Photoconductivity Apparatus .....	64
Figures 33 – 43.....	65
7. List of Publications .....	77

## Executive Summary

The scope of the work under this subcontract entails investigation of engineering improvements in the performance and stability of solar cells in a *systematic* way. It consists of the following four tasks.

**Task 1.** Materials research and device development

**Task 2.** Process improvement directed by real time diagnostics

**Task 3.** Device loss mechanisms

**Task 4.** Characterization strategies for advanced materials

Not unexpectedly in the work performed there is extensive overlap between the tasks, but in this report it is summarized using these categories.

### Task 1.

Task 1 explored the possibility of improving the stabilized performance of cell structures using a layer-by-layer technique to deposit the intrinsic layers of p-i-n cells with guidance from real time optics. It was also directed at developing “state-of-the-art” n-i-p (substrate) solar cells and address their apparent inherent differences from p-i-n (superstrate) cell structures.

Although an effective strategy for optimizing the i-layer is to ensure that the growth process remains just on the amorphous side of the amorphous-to-mixed-phase boundary, multi-step dilution is deleterious if the bandgaps of the materials differ appreciably. The results indicate that even if the bandgap discontinuities are small their aggregate influence results in an increase in recombination in the bulk – thereby lowering FF. The initial results in this study were not encouraging and further studies will be delayed until results are obtained which indicate that this can be applied without reducing the initial performance of the cells. The improved stability of protocrystalline material deposited closer to the amorphous-to-mixed phase transition could then be further explored.

Phase diagrams developed using real time spectroscopic ellipsometry (RTSE) to characterize thin film growth and microstructure, have been successful in explaining the nature of p-Si:H films doped with  $\text{BF}_3$  and guiding the development of high  $V_{\text{OC}}$  in n-i-p solar cells. It has been proposed for a long time that the optimum p-layers are high conductivity doped microcrystalline Si:H ( $\mu\text{c-Si:H}$ ). We find that this earlier work is flawed and that the protocrystalline nature of the p-type Si:H layers -- *and not their microcrystalline* -- is responsible for obtaining high  $V_{\text{OC}}$ s in n-i-p a-Si:H solar cells. Phase diagrams plotted as a function of  $R=[\text{H}_2]/[\text{SiH}_4]$  were obtained that describe the microstructural evolution with thickness of the protocrystalline p-layers having different doping gas flow ratios  $D=[\text{BF}_3]/[\text{SiH}_4]$ . From the phase diagrams it was established that the highest open circuit voltage is obtained by incorporating a protocrystalline Si:H layer with the transition to mixed phase amorphous + microcrystalline Si:H structure at the very top of the layers. As a result, a small volume fraction of nanocrystals are expected to be present in the p-layer just prior to its transition into the (a+ $\mu\text{c-Si:H}$ ) mixed phases. This expectation is further confirmed with AFM and TEM results.

The detrimental contributions of the microcrystalline phase underscore the widely held misconception that microcrystalline Si:H is responsible for the high  $V_{OC}$ . In addition, these studies explain why the attempts to obtain  $V_{OC}$  values in superstrate p-i-n cells as high as in n-i-p ones using *microcrystalline* p-layers failed. Because of the microstructure evolution in the protocrystalline p-layers into a mixed (a+ $\mu$ c-Si:H) phase, such a transition at the p/i interface in these cell structures has a very large effect on lowering  $V_{OC}$  and FF, as has been shown for the case of p-i-n cells<sup>1</sup>. The results also lead to the conclusion that in order to maximize  $V_{OC}$ , it is necessary to deposit the p-layers at the maximum R values that allows the desirable thickness to be obtained without crossing the transition into the mixed phase growth regime.

The possible mechanisms responsible for the differences in 1 sun  $V_{OC}$  obtained with the p-Si:H layers, as well as their reported higher than those with p a-SiC:H layers, were also investigated. Studies were carried out on both types of n-i-p cell structures with identical i-layers. Carrier recombination in both types of cell structures was characterized with  $J_D$ -V measurements and the recombination in their p/i interface regions was identified and quantified. The systematic studies clearly established that the lowest p/i interface recombination is obtained with *protocrystalline a-Si:H* and not layers containing any *microcrystalline* phase. This p/i interface recombination is found to be significantly lower than that achieved with the optimum a-SiC:H structure and for all the cell structures such recombination could be directly correlated to their 1 sun  $V_{OC}$  values. This points to the reason why open circuit voltages obtained with protocrystalline p-Si:H layers are higher than those with p a-SiC:H. The results also substantiate the mechanisms discussed under Task 3 for the limitations imposed by carrier recombination in high quality a-Si:H cells. The significantly lower p/i interface recombination in the protocrystalline p-Si:H cells is attributed in large part to the subsurface modification of the intrinsic layer during the deposition of the p-contact. Evidence is found that the high concentrations of atomic hydrogen present during the deposition of the protocrystalline p-Si:H layer are responsible for this beneficial effect. In addition, unlike a-SiC:H, it allows the protocrystalline p-layer to be used in fabricating solar cell structures without any adverse effect of exposing the i-layers to air.

The same solar cell characteristics have been obtained with p-i-n (superstrate) and n-i-p (substrate) solar cell structures incorporating a-SiC:H p-layers. This is found for cell structures with R=0 and R=10 i-layers and different p/i and i/p interfaces. The absence of such equivalence between the two types of cell structures with the so-called microcrystalline p-contacts, is attributed to the microstructural evolution of the protocrystalline layers into a mixed (a+ $\mu$ c-Si:H) phase at the p/i interface of the p-i-n cell structures. The observed equivalence between p-i-n and n-i-p cells is inconsistent with defect state distributions and electric fields predicted by the widely promoted defect pool model (discussed in Task 3).

## Task 2.

In Task 2 real time spectroscopic ellipsometry has been applied to develop deposition phase diagrams that can guide the fabrication of hydrogenated silicon (Si:H) thin films at low temperatures (<300°C) for high performance solar cells. The simplest

---

<sup>1</sup> R. J. Koval, C. Chen, G.M. Ferreira, A.S. Ferlauto, J.M. Pearce, P.I. Rovira, C.R. Wronski and R.W. Collins, *Appl. Phys. Lett.* **81**, 1258 (2002).

phase diagrams have been extended to include the thickness at which a roughening transition is detected in the amorphous film growth regime. From the results obtained on the amorphous roughening transition during the growth, it is proposed that optimization of a-Si:H in higher rate rf PECVD processes require the maximum possible thickness onset for this roughening transition.

The surface microstructure and the phase of hydrogenated silicon (Si:H) thin films prepared by rf PECVD at low temperature evolve as a function of thickness, as is evident from continuous RTSE measurements and analysis. The evolutionary processes that have been established and detailed in previous studies<sup>2,3</sup> include (i) a nuclei coalescence effect in the initial stages of growth [surface smoothening], (ii) a surface morphological transition in the bulk growth regime without a change in phase [ $a \rightarrow a$ , surface roughening], (iii) a nucleation transition in the bulk regime in which microcrystallites evolve from the growing amorphous phase [ $a \rightarrow (a+\mu c)$ ; surface roughening], and (iv) a process of crystallite contact and coalescence in the bulk regime involving a transition from mixed-phase  $(a+\mu c)$ -Si:H to single-phase  $\mu c$ -Si:H [ $(a+\mu c) \rightarrow \mu c$ ; surface smoothening]. The thicknesses at which these transitions occur, as well as the magnitudes of the effects in some cases, correlate one with another, as well as with the optical, electrical, and device properties of the Si:H films.

Among the surface microstructural and phase transitions, the  $a \rightarrow a$  roughening transitions, the  $a \rightarrow (a+\mu c)$  roughening transitions, and the  $(a+\mu c) \rightarrow \mu c$  smoothening transitions have been incorporated into deposition phase diagrams. In these diagrams, the Si:H bulk layer thicknesses at which these transitions occur can be plotted as continuous functions of a key deposition variable that is used to control the phase, typically the  $H_2$ -to- $SiH_4$  gas flow ratio  $R=[H_2]/[SiH_4]$ . The phase diagram depends not only on the other fixed deposition conditions, such as plasma power, substrate temperature, and total gas pressure, but also on the substrate since the latter exerts a strong influence over crystallite nucleation. Deposition phase diagrams are very convenient in the design of devices since they describe the regimes of layer thickness and deposition parameter space within which single-phase a-Si:H,  $(a+\mu c)$ -Si:H, and single-phase  $\mu c$ -Si:H are obtained. As a review of such phase diagrams, Fig. 1 shows the proposed schematic structure of  $\sim 5000$  Å thick Si:H films on  $R=0$  a-Si:H substrate films, given as a continuous function of  $R$  along with the thicknesses of the  $a \rightarrow (a+\mu c)$  and  $(a+\mu c) \rightarrow \mu c$  transition boundaries. In such structures, the cone angle for crystallite growth is relatively constant at  $15$ - $20^\circ$  and the nucleation density increases rapidly with increasing  $R$  as is discussed in task 4.

Correlations of the phase diagrams for intrinsic Si:H layers with the corresponding electronic properties and p-i-n device performance demonstrate that the optimum i-layers are obtained at the maximum possible  $R$  value for the desired thickness without crossing the  $a \rightarrow (a+\mu c)$  boundary of the phase diagram into the mixed-phase growth regime. It should be emphasized that because the  $R$  value at this phase boundary depends on both the nature of the substrate and the i-layer thickness, these aspects of the materials or device structure must be specified in order to identify the optimum conditions. For i-layers deposited on amorphous film substrates (such as the p or n-layers of p-i-n or n-i-p solar cells), the optimum a-Si:H i-layer material has been described as *protocrystalline* Si:H. As its name implies, protocrystalline Si:H ultimately evolves into  $(a+\mu c)$ -Si:H if the film is allowed to grow beyond the desired thickness for which the deposition process

<sup>2</sup> J. Koh, Y. Lee, H. Fujiwara, C. R. Wronski, and R. W. Collins, Appl. Phys. Lett. **73** (1998) 1526.

<sup>3</sup> A. S. Ferlauto, R. J. Koval, C. R. Wronski, and R. W. Collins, Appl. Phys. Lett. **80** (2002) 2666.

was optimized. The unique characteristic of protocrystalline Si:H is its higher stability to light induced degradation as measured for both materials and devices. Finally, because the  $a \rightarrow (a+\mu c)$  transition decreases in thickness with increasing  $R$ , two-step and even multi-step i-layer processes can be designed on the basis of the phase diagram in order to optimize solar cells. Performance levels beyond those accessible in one-step processes have been demonstrated.

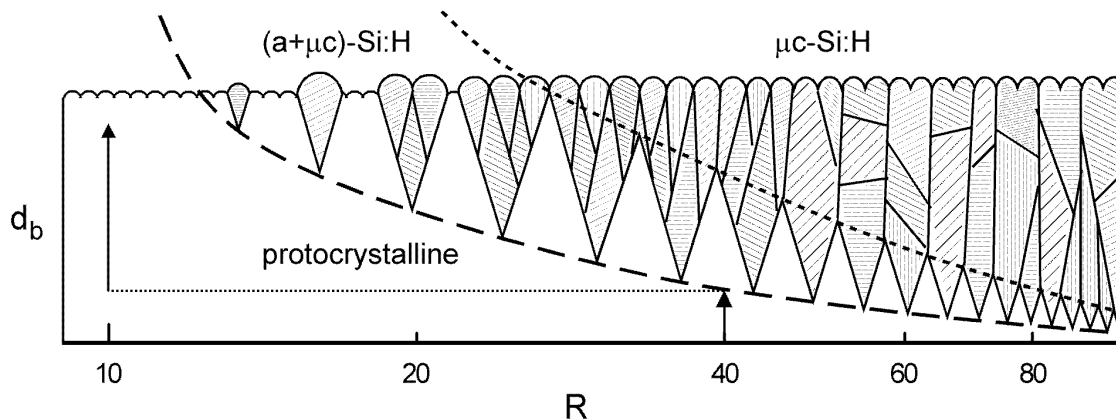


**Figure 1.** Schematic of the structure of Si:H films prepared as a function of  $R$ . The dashed and dotted lines identify the  $a \rightarrow (a+\mu c)$ , and  $(a+\mu c) \rightarrow \mu c$  transitions, respectively. The arrows denote the two-step protocrystalline Si:H i-layer process found to optimize the performance of p-i-n and n-i-p solar cells.

### Task 3.

The work carried out under Task 3 was directed at: development of a reliable methodology for characterizing the intrinsic and light induced defects for intrinsic a-Si:H materials in thin films and solar cell structures; establishing the “elusive” direct correlations between thin film properties and corresponding solar cells; as well as improving the understanding of SWE.

Several issues were addressed in this research regarding the mechanisms and defects determining a-Si:H solar cell characteristics that have not yet been clearly resolved. These include: (i) identifying and then quantifying the contributions to carrier recombination occurring at the interfaces and in the bulk of the i-layers; (ii) assessing the serious consequences that result from interpreting solar cell characteristics based on the assumption of spatially non-uniform distributions of defects in the i-layers as predicted by the defect thermodynamics model; (iii) self consistently correlating carrier recombination to different cell characteristics; and (iv) characterizing the nature of the different light induced defects responsible for SWE.

The important issues raised by the predictions of the defect thermodynamic model on the operation of solar cells have been addressed. The spatially non-uniform distribution of defects, such as have recently been inferred from drive level capacitance profiling<sup>4</sup> and dark current voltage characteristics<sup>5</sup>, have very serious consequences on

<sup>4</sup> R. S. Crandall, J. Yang and S. Guha, *Mat. Res. Soc. Symp. Proc.*, **664**, A.19.2.1 (2001).

<sup>5</sup> M. A. Kroon and R. A. C. M. M. Van Swaaij, *J. Appl. Phys.*, **90**, 994 (1992).

the interpretation of results on solar cells as well as the ability to correlate these results with those on corresponding intrinsic thin films.

Detailed studies were carried out on the forward bias dark current ( $J_D - V$ ) characteristics of both p-i-n (superstrate) and n-i-p (substrate) p a-SiC:H solar cell structures. By controlling the recombination at the p/i interfaces through changing the band gap of the 200 Å a-Si:H i-layers adjacent to the a-SiC:H p-contact it was possible to clearly separate the contributions of the intrinsic layers from those of the p/i interfaces to the  $J_D - V$  characteristics.

The clearly established contributions of carrier recombination in the i-layers to the  $J_D - V$  characteristics are found to be consistent with diffusive currents whose recombination is governed by the Shockley-Read-Hall (SRH) recombination model. These dark current characteristics are also found to be consistent with a uniform distribution of defects in the i-layers that have a continuous energy distribution of gap states. The “elusive” dependence of  $J_D - V$  characteristics on the thickness of the i-layer is found, which excludes the existence of large densities of defect states in the regions of the i-layers adjacent to the n and p-contacts. Furthermore, equivalence in the  $J_D - V$  characteristics and recombination in the i-layers is found between the p-i-n and n-i-p solar cell structures – which is excluded by the defect pool model.

These results clearly point to the presence of *homogeneity with i-layer depth* and the *absence* of the large spatially non-uniform densities of defects as predicted by thermodynamic equilibration of dangling bonds. In view of this, it is possible to utilize such characteristics in the study of different defect states whose contribution to the recombination currents changes as the quasi-Fermi level splitting increases with forward bias. In addition such results can be directly correlated with those on the corresponding i-layers since both p-i-n and n-i-p cells also have *homogenous* defect distributions.

Studies were carried out on understanding the mechanisms responsible for solar cell characteristics and their dependence on both bulk i-layer properties as well as those of the p/i and n/i interface regions. Emphasis was given to obtain self-consistent interpretations for the different characteristics and their dependence on SWE. This was addressed first by investigating the correlations between  $J_{sc} - V_{oc}$  and  $J_D - V$  characteristics over a wide range of voltages and light intensities. The reported absences of superposition between these characteristics have been attributed to large difference in the recombination occurring in the dark and under illumination<sup>6</sup>. Results were obtained on  $J_{sc} - V_{oc}$  characteristics for a variety of p-i-n and n-i-p solar cell structures exhibiting superposition with  $J_D - V$  characteristics over a wide range of voltages. This and the observed separation and its dependence on the light induced defects in the i-layer are consistent with arguments based on first principles for the drift transport of photo-generated carriers and the diffusive currents from the n and p contact regions. The conclusions drawn about the role of the lifetimes of the photo-generated carriers, the densities of defects and the potential barriers in the i-layers adjacent to the n and p contacts were confirmed by numerical simulations. These potential barriers, which depend on the densities of defects in this region, play a key role in carrier transport even when their densities are those of the i-layer and not those associated with the defect pool. Inadvertent high densities of defects there can lead to the observed absences of superposition between  $J_{sc} - V_{oc}$  and  $J_D - V$  characteristics as well as diode quality factors greater than two. The results also suggest

---

<sup>6</sup> S. Hegedus, N. Salzman, and E. Fagen, J. Appl. Phys. **63**, 5126 (1988).

that in interpreting the beneficial effects of higher bandgaps in these regions of a-Si:H cells the role of the corresponding densities of defects should be taken into account<sup>7</sup>.

The limitations imposed by the p/i interfaces in p a-SiC:H cell structures on the 1 sun  $V_{OC}$  have been identified as well as the effects on their stability. Evidence has been found that the p/i interface recombination at the protocrystalline p/i interfaces is lower, which has allowed the limitations of bulk recombination on the 1 sun  $V_{OC}$  to be addressed. The limitations of 1 sun  $V_{OC}$ 's were identified from the degradation kinetics, which could be related to the kinetics obtained at lower light intensities where the  $V_{OC}$ 's are limited by bulk recombination. Studies are being carried out on identifying the limitation imposed by the recombination in the tail states from that in the defect states.

Correlations have been obtained between solar cell fill factors and the electron recombination in films with a similar quasi-Fermi level splitting as that in solar cells which are highly significant. Apart from establishing the long-sought correlations between results on thin films and those on corresponding solar cells, the results point to the importance of further addressing the many unanswered questions that remain concerning the nature and energy distribution of the different light induced defect states in a-Si:H. This is being carried out with detailed studies on cell  $J_D$ -V characteristics and the subgap absorption on corresponding thin film i-layers.

#### Task 4.

In Task 4 work was carried out to identify and quantify the development of crystallinity across the amorphous-to-microcrystalline transition from the evolution of the dielectric functions during growth. Also the photon energy range in the dual beam photoconductivity measurements was extended down to 0.5 eV in order to allow detailed studies to be carried out on both a-Si:H and a-SiGe:H materials. In addition assistance was given to the NREL amorphous silicon group to develop RTSE measurements of hot wire CVD Si:H films.

Owing to the importance of Si:H deposition near the  $a \rightarrow (a+\mu c)$  and  $(a+\mu c) \rightarrow \mu c$  boundaries of the phase diagram for the optimization of the intrinsic (i) layers in a-Si:H and  $\mu c$ -Si:H solar cells, techniques are needed to determine the evolution of the crystalline Si:H content as a continuous function of the accumulated thickness. For this purpose the application of real time spectroscopic ellipsometry (RTSE) has been developed for a Si:H films that undergo the  $a \rightarrow \mu c$  transition. The evolution of the surface roughness layer thickness ( $d_s$ ) and the bulk layer thickness ( $d_b$ ) is obtained by a self-consistent analysis procedure based on a two layer (surface-roughness/bulk) optical model. During the growth there is a increase in the values of  $d_s$  that reflect the preferential growth of the  $\mu c$ -Si:H phase in the mixed-phase regime. As the films further evolve in thickness, the Si crystallites eventually cover the entire film surface and a transition to a single-phase  $\mu c$ -Si:H growth regime is observed. This transition is reflected in the data as a peak and subsequent smoothening effect in  $d_s$ .

A self-consistent method based on a virtual interface (VI) approach was developed to analyze the RTSE measurements of Si:H films that undergo these  $a \rightarrow \mu c$  transitions. This method can provide the continuous evolution of the  $\mu c$ -Si:H volume fraction ( $f_{\mu c}$ ) and the surface roughness layer thickness ( $d_s$ ) in the mixed-phase  $(a+\mu c)$ -Si:H regime, as well as the optical properties of the Si:H film in the a-Si:H, mixed-phase  $(a+\mu c)$ -Si:H,

---

<sup>7</sup> D. Lundszein, F. Finger, and H. Wagner, 17<sup>th</sup> European PSEC, 2001

and single-phase  $\mu\text{c-Si:H}$  regimes. The novel analysis developed in this research project can provide quantitative information about the evolution of the microstructural and optical properties of Si:H films that undergo the  $\text{a} \rightarrow \mu\text{c}$  transition. This information is used in the understanding and optimization of intrinsic and doped Si:H layer growth processes in thin film Si:H solar cells.

## Task 1

### Multi-step i layer

Correlations obtained between the RTSE results and the cell characteristics reported previously<sup>8</sup> indicate that an effective strategy for optimizing the i-layer is insuring the growth process remains just on the amorphous side of the amorphous-to-mixed-phase boundary. These materials, known as *protocrystalline*, exhibit improved short range ordering and a different microstructure than the standard amorphous films. The purpose of this task was to explore the use of a layer-by-layer technique to deposit the intrinsic layers of p-i-n cells for improved stabilized performance of cell structures.

Several deposition schemes were attempted using a high R (e.g. R=40) material sandwiched in between various thickness' of low R (e.g. R=10, 5) where two of these are summarized in Table I. These cells have lower initial FFs than a homogeneous i-layer as can be seen in Fig. 2. As the thickness of the R=40 layers is increased in proportion to the R=10 layer the FF is further reduced. In order to explain such decreases in performance numerical simulations were carried out for the cells in Table 1 using multiple layers with different hydrogen dilutions and thus slightly different bandgaps. The results indicate that even in the case of the bandgap discontinuities being relative small their cumulative influence results in an increase of the photo-generated carrier recombination in the bulk over that of a homogeneous material – thereby lowering the FF. It appears that in order to avoid the deleterious effect of even small bandgap discontinuities indicated by simulations, the multi-layer deposition must be controlled in such a way as to prevent the onset of any phase transition. Because the initial results of this approach were not encouraging, it was delayed until a better understanding was obtained for both the properties of these phase transitions as well as their growth and evolution (discussed under Task 2).

Sample ID	D(R=40)	D(R=5)	# of cycles	i-layer thickness
T2C	100Å	300Å	5	~2000Å
T2D	200Å	200Å	5	~2000Å

Table I. Deposition conditions for multi-layer bulk i-layers in p-i-n structures.

### n-i-p Solar Cell Structures

State of the art n-i-p solar cell structures have been developed. Initially the Si:H p-layers intended for use in n-i-p cells were developed for high nucleation density and single-phase microcrystallinity on a-Si:H i-layer substrates using the single chamber system and guidance from RTSE. In this study, the surface of the i-layer was subjected to an initial 2 min H<sub>2</sub>-plasma treatment in order to generate nanocrystalline nuclei. Three different doping gases were investigated, including B<sub>2</sub>H<sub>6</sub>, B(CH<sub>3</sub>)<sub>3</sub>, and BF<sub>3</sub>. Then, different doping gas flow ratios D were employed to ensure high conductivity in thin layers, and different plasma power levels and R values were utilized to ensure single-

<sup>8</sup> C.R. Wronski, R.W. Collins, J.M. Pearce, R.J. Koval, A.S. Ferlauto, G.M. Ferreira, and C. Chen, "Stable a-Si:H based Multijunction Solar Cells with Guidance from Real-Time Optics", *Phase III Technical Status Report*, (Subcontract No. XAF-8-17619-22 – November 2002).

phase  $\mu\text{c-Si:H:B}$ . A very robust process with a wide window for single phase  $\mu\text{c-Si:H:B}$  was found using  $\text{BF}_3$  doping gas with  $D=0.2$  and  $R=200$ . This preferred p-layer process was then adapted to the multi-chamber deposition system for n-i-p solar cell fabrication on Cr-coated glass substrates using an  $R=10$  i-layer and sputtered ITO top contacts.

After fabrication of n-i-p solar cells with p-layers designed for dense, single-phase  $\mu\text{c-Si:H}$  structure, a number of n-i-p devices were prepared in a multi-chamber PECVD system under a variety of p-layer and p/i interface-layer conditions. For all such cells, the i-layer was  $4000 \text{ \AA}$  thick and prepared with  $R=10$ , but the 2 min  $\text{H}_2$ -plasma treatment was eliminated in order to avoid any direct substrate-induced microcrystallinity in the overlying p-layers. In this approach,  $\text{BF}_3$  doping gas was used with  $D=0.1$  and  $0.2$ , and  $R$  was varied over the range  $50 \leq R \leq 200$ . Solar cells were also compared with and without a  $200 \text{ \AA}$  thick  $R=40$  protocrystalline i-layer region deposited just prior to the p-layer. In this way, i-layer substrate-dependent effects on the p-layer could be assessed. Additional information is presented in Task 4.

This is illustrated by the 1-sun light J-V characteristic in Fig. 3 of an a-Si:H n-i-p solar cell incorporating the p-layer process with  $D=[\text{BF}_3]/[\text{SiH}_4]=0.2$  and  $R=200$ , yielding single-phase  $\mu\text{c-Si:H:B}$ . Also shown for comparison is the light J-V characteristic of a cell in which the  $\mu\text{c-Si:H}$  p-layer process is replaced by a standard a-SiC:H p-layer. It is clear that incorporation of the single-phase  $\mu\text{c-Si:H}$  p-layer leads to a reduction in  $V_{oc}$  (by  $0.12 \text{ V}$ ) relative to the a-SiC:H p-layer, but the fill factor and short-circuit current ( $J_{sc}$ ) remain essentially unaffected.

It was found that p-layer deposition processes designed to maximize the crystallinity and density of a  $200 \text{ \AA}$  p-layers do not optimize the performance of high-quality solar cells. The fact that a significant reduction of  $V_{oc}$  is observed record efficiencies are unlikely for cells incorporating p-layers that are *purely microcrystalline*. The approach taken was then to focus on n-i-p cells, in which the volume fraction of crystallinity has been determined from ex situ SE measurements of the p-layer in the actual device structure rather than from RTSE during deposition.

From the results a phase diagram was obtained for the evolution of the microstructure with thickness in the p-Si:H layers deposited with different  $R$ . The phase diagram for layers having doping ratio of  $D=0.2$  is shown in Fig. 4 where the regions of protocrystalline a-Si:H, mixed (a+ $\mu\text{c}$ )-Si:H, and purely microcrystalline Si:H phases can be clearly identified. Also shown in Fig. 4 are the 1 sun  $V_{oc}$  values obtained from corresponding n-i-p solar cell structures fabricated with  $\sim 200 \text{ \AA}$  of these p-layers. The highest  $V_{oc}$  is achieved by the cell having a  $R=150$  p-layer which is in the protocrystalline a-Si:H phase and where its growth is terminated at or close to the transition into the mixed (a+ $\mu\text{c}$ )-Si:H phase. In the case of  $R=100$ , the p-layer is amorphous throughout its thickness and the  $200 \text{ \AA}$  thickness is nowhere close to the transition into a mixed phase. On the other hand for the  $R=200$  cell, the p-layer is in the form of a mixed (a+ $\mu\text{c}$ )-Si:H phase right from the beginning and evolves into a purely microcrystalline phase at the thickness of  $\sim 200 \text{ \AA}$ . In the optimized protocrystalline p-layers the volume fraction of crystallites in the films is found to be below 2%, which is the detection limit of SE. In order to confirm the actual microstructure of these p-layers, a series of AFM and TEM studies were carried out on cell structures deposited on crystalline silicon in the form of c-Si substrate/  $1000 \text{ \AA}$   $\text{SiO}_2$ /  $1000 \text{ \AA}$  evaporated Cr/  $250 \text{ \AA}$  n a-Si:H/  $1000 \text{ \AA}$  i ( $R=10$ ) a-Si:H/  $250 \text{ \AA}$  p protocrystalline-Si:H. The above cell structure was examined in a non-contact mode with a Park Scientific M5 Atomic Force

Microscope (AFM). The surface topography, which is shown in Fig. 5, characterizes a  $1\ \mu\text{m} \times 1\ \mu\text{m}$  area. The RMS surface roughness was 2.36 nm and is within the range of the surface roughness values measured for known amorphous films on smooth c-Si substrates, as studied in the same manner. The AFM results are consistent with those of RTSE which indicated that the presence of any crystalline phase is limited to a low density ( $< 2\ \text{vol.}\%$ ) and/or very small crystallites. The lack of any significant crystallite volume fraction in the optimized protocrystalline p-layer material was further confirmed with TEM performed by M. Al-Jassim and K. Jones at NREL. By combining the results of electrical measurements of devices with RTSE, AFM, and -- most persuasively -- with TEM, it can now be firmly concluded that the optimized protocrystalline-p contact layer is right on the phase transition boundary between amorphous and mixed phase Si:H growth as characterized by the appearance of a low density of nanocrystallites.

These results clearly point to the highest  $V_{\text{OC}}$  being obtained with a protocrystalline a-Si:H p-layer which is deposited at a maximum R value that allows the desired thickness to be obtained without crossing the transition into the mixed (a+ $\mu\text{c}$ )-Si:H phase growth regime.

A study was carried out to identify the mechanisms limiting 1 sun  $V_{\text{OC}}$  values with the different p-Si:H layers as well as the higher values obtained with protocrystalline Si:H than with a-SiC:H p-layers. In this study  $J_{\text{D}}-V$  characteristics were used to investigate the carrier recombination that could be limiting 1 sun  $V_{\text{OC}}$  in both the p-Si:H and p a-SiC:H n-i-p cell structures. In the a-SiC:H n-i-p cell structures which had different p/i interfaces, but identical p- and bulk i-layers, the respective contributions of bulk and p/i interfaces to carrier recombination could be clearly identified and quantified from their  $J_{\text{D}}-V$  characteristics. The beneficial effects of incorporating a thin protocrystalline region prior to the deposition of the a-SiC:H p-layer is in agreement with the results reported for p-i-n structures<sup>9</sup>. Fig. 6 shows the forward  $J_{\text{D}}-V$  characteristics of two a-SiC:H n-i-p structures with different p/i interface regions, where the recombination at the p/i interface can be clearly identified. The bandgaps ( $\alpha_{2000}$ ) of the R=10 and R=40 p/i interface regions incorporated in these cells are 1.86 and 1.95 eV respectively.

From the two regimes in the  $J_{\text{D}}-V$  characteristics in Fig. 6 the carrier recombination in forward bias currents that occurs in the bulk and at the p/i interface can be clearly separated as in the case of corresponding p-i-n cell structures (discussed under Task 3). At the lower voltages there is a diode quality factor of  $m=1.4$  which then decreases to values closer to 1 at the higher voltages. The regimes where  $m=1.4$  correspond to bulk recombination and as expected there is overlap in the currents over an extended voltage region. As the p/i interface is improved by introducing the R=40 p/i layer, the bulk recombination regime extends to a higher bias and the currents corresponding to the p/i interface recombination become lower. The key role played by this recombination in the p/i interface regions in determining the 1 sun  $V_{\text{OC}}$  is reflected in their systematic decrease as R at the p/i interface is increased from 0 to 10 to 40 the corresponding 1 sun  $V_{\text{OC}}$  increases from 0.86 to 0.90 to 0.92 V.

Shown in Fig. 7 are the forward bias  $J_{\text{D}}-V$  characteristics of the n-i-p solar cells with R=100, 150 and 200. In Fig. 8 the corresponding 1 sun light I-V's are shown. In Fig. 7 the contribution of the p/i interface to recombination can be distinguished from those of the bulk. Just as in the case of the results in Fig. 6, the overlap in the characteristics at the

<sup>9</sup> J. Koh, Y. Lee, H. Fujiwara, C.R. Wronski and R.W. Collins, *Appl. Phys. Lett.*, **73**, 1526 (1998).

lower voltages reflects the bulk recombination which is the same in all three cells. At the higher voltages the relative contribution of the recombination at the p/i interface regions in the three cells can be identified. This recombination can be seen to be the lowest for the R=150 cell, highest for the R=200 cell and in between those for the R=100 cell. It is important to note here that the differences in 1 sun  $V_{OC}$  in these cells can again be directly attributed to the changes in these recombination currents. In addressing the mechanisms limiting  $V_{OC}$  in p-Si:H cells, unlike the case of the p-a-SiC:H cell structures, the effects of the changes in the p-layer have to be also considered. In addition to the effect of R on microstructural changes just discussed, there are also differences in bandgaps and the doping efficiencies of the p-layers, as well as subsurface reactions due to the very high hydrogen dilution used in the deposition of the p-layers.

The recombination at the p/i interface depends on parameters which include: the densities of defects at the interface itself as well as the p/i region, the bandgap in the p/i region and its alignment with that of the p-layer, and the built-in potential ( $V_{bi}$ ) which depends on both bandgap alignment between the i- and p-layers as well as its doping efficiency. When R is increased from 100 to 150 in the two protocrystalline p-layers there is an increase in the gap as well as the doping efficiency which could increase the  $V_{bi}$ . An increase in  $V_{bi}$  contributes to the reduction of recombination at the p/i interface since it decreases the concentration of electrons in the interface region, thus lowering the recombination there<sup>10</sup>. It should be noted here that the effect of moving the Fermi level as a consequence of the higher doping efficiency is counteracted by the increase in the p-a-Si:H bandgap. Another possible reason for the significant reduction in recombination seen in Fig. 7 is due to the differences in the p/i interfaces themselves in addition to those of the interface regions. The higher R, which improves the microstructure of the protocrystalline p-layer, can also result in a p/i interface with a lower density of defects that reduces the p/i interface recombination velocity.

Another consequence of the higher R is its effect in subsurface reactions which improve the i-layer adjacent to the p/i interface in an analogous way to that obtained with the protocrystalline a-Si:H buffer layers used in a-SiC:H cells. That this occurs is indicated by significant changes in the bandgap of  $\sim 200$  Å in the intrinsic a-Si:H that are observed during the deposition of the protocrystalline p-layers. When R is increased from 150 to 200 and the p-layer is immediately formed in the mixed (a+ $\mu$ c)-Si:H phase not only does the nature of the p/i interface change but there is also a decrease in the gap of the p-layer. This decrease is fairly symmetrical for the conduction and valence band<sup>11</sup> so even though the doping efficiency remains high, the net band misalignment can in fact lead to a decrease of  $V_{bi}$  and further enhance the p/i interface recombination, as indicated by the results in Fig. 7. The low recombination that is obtained at the p/i interface with the R=150 protocrystalline p-layer is significantly smaller than that for the R=40 buffer layer in the a-SiC:H n-i-p cells which was the lowest achieved for those cells. This is illustrated in Fig. 9 which shows the  $J_D$ -V characteristics between 0.6 and 1.0 V, where also as a consequence of this low p/i interface recombination in the protocrystalline p-Si:H cell the bulk recombination regime extends to higher voltages. It also explains why the 1 sun  $V_{OC}$  increases from 0.92 to 0.96 V and suggests that in the latter case it could now actually be limited by bulk recombination in the i-layer. In comparing the

<sup>10</sup> J. Deng, J.M. Pearce, R.J. Koval, V. Vlahos, R.W. Collins and C.R. Wronski, *Appl. Phys. Lett.* (May 2003, in press).

<sup>11</sup> J. Koval, A. S. Ferlauto, J. M. Pearce, R. W. Collins, and C. R. Wronski, *J. of Non-Cryst. Solids* **299-302**, 1136 (2002).

recombination at the p/i interfaces in these two cell structures it is important to note the difference in the way they are formed. In the case of the a-SiC:H cell the top 200 Å of the i-layer is modified by increasing R from and subsequently depositing the p-layer. The deposition conditions under which the protocrystalline p-layer is grown are such that there are modifications in the subsurface region of the i-layer as discussed earlier. These are attributed to the very large concentrations of atomic hydrogen which is generated by the very high R and power levels utilized for the deposition of the p-layer.

A consequence of such concentration of atomic hydrogen is that the p/i interface region become far less sensitive to the presence of a barrier layer on the intrinsic a-Si:H than in the case of n-i-p a-SiC:H cell structures. This is illustrated in Fig. 10 where the light I-V characteristics are shown for the two types of cells with and without exposure of the i-layer to air for 24 hours before the p-layer deposition. It can be seen in Fig. 10a that the air exposure introduced to the p-a-SiC:H n-i-p cell has a drastic effect on its performance by significantly lowering the  $V_{OC}$  and FF values as compared to an identical cell completed without an air-gap. Exposure of the sensitive p/i interface region to air leads to the formation of a thin native oxide whose effect is *not* eliminated by the subsequent deposition of a-SiC:H. On the other hand, virtually the same p/i interface regions are obtained in the protocrystalline cells with and without the exposure to air as is indicated by the identical light I-V characteristics, as shown in Fig. 10b.

### Equivalence between p-i-n and n-i-p Cell Structures

The often suggested inherent differences between p-i-n and n-i-p a-Si:H solar cells was addressed by investigating such cells with identical i- and p-layers. The extensively-reported differences between p-i-n and n-i-p cells with so called “microcrystalline” p-layers are believed to be a consequence of the observed protocrystalline nature of the highest  $V_{OC}$  contacts and their rapid evolution with thickness into the mixed amorphous + microcrystalline phase. In the p-i-n (substrate) configuration, the phase transition into the mixed amorphous + microcrystalline phase occurs right at the p/i interface rather than at the TCO contacts as in the case of n-i-p (substrate) cells. The large effects on carrier recombination of the phase transitions from protocrystalline a-Si:H to the mixed (a+ $\mu$ c-Si:H) phase, have been demonstrated through the incorporation of intrinsic-Si:H buffer layers on a-SiC:H p-i-n and n-i-p structures<sup>12</sup>. The phase transition makes it extremely difficult to control the p/i interface reproducibly. Such control is possible only with real-time spectroscopic-ellipsometry and such a capability is being established at Penn State in a multi-chamber system that allows the fabrication and study of high performance cells.

In the case of a-SiC:H cells equivalence is found between the cell characteristics of p-i-n (superstrate) and n-i-p (substrate) cells having a-SiC:H p-contacts with both undiluted (R=0) and diluted (R=10) protocrystalline i-layers. Results of a detailed study on carrier transport and recombination for a variety of p-i-n and n-i-p cell structures incorporating p-type a-SiC:H are presented in Task 3, where this equivalence is further established. Such conclusions point to the absence of defect distributions predicted by the widely-promoted thermodynamic equilibrium model.

---

<sup>12</sup> R.J. Koval, J.M. Pearce, A.S. Ferlauto, P.I. Rovira, R.W. Collins, and C.R. Wronski, *IEEE Photovoltaics Specialists Conf. Proc.*, (IEEE, 2000), pp. 750-753 (2000).

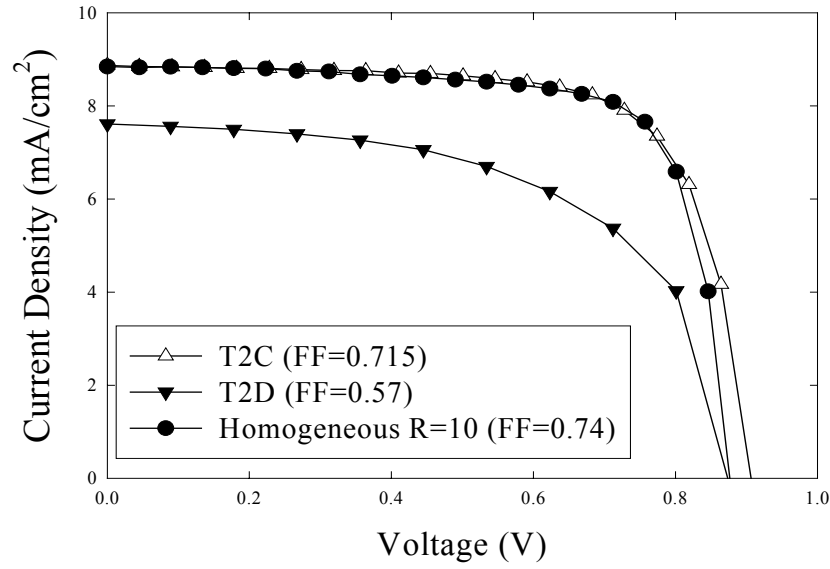


**Figure 2.** Light I-V characteristics for a homogeneous R=10 i layer p-i-n cell and two cells containing multi-layers shown in Table I.

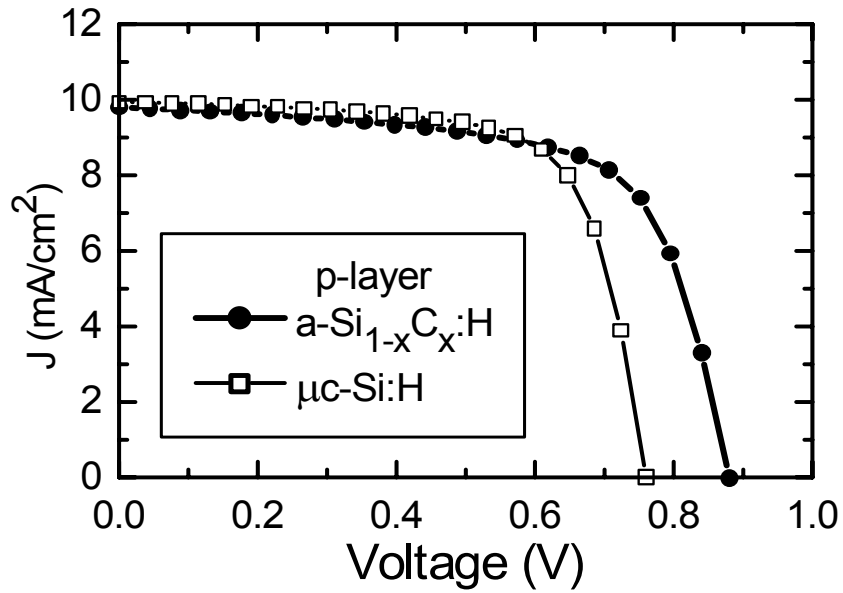


**Figure 3.** Light J-V characteristics for two a-Si:H n-i-p solar cells deposited at 200°C, one incorporating a single-phase  $\mu\text{c-Si:H}$  p-layer prepared with  $D=[\text{BF}_3]=0.2$  and  $R=200$  (open symbols) and the other incorporating an  $\text{a-Si}_{1-x}\text{C}_x\text{:H}$  p-layer prepared with  $D=[\text{B}(\text{CH}_3)_3]/[\text{SiH}_4]=0.0125$  and  $R=0$  (solid symbols).

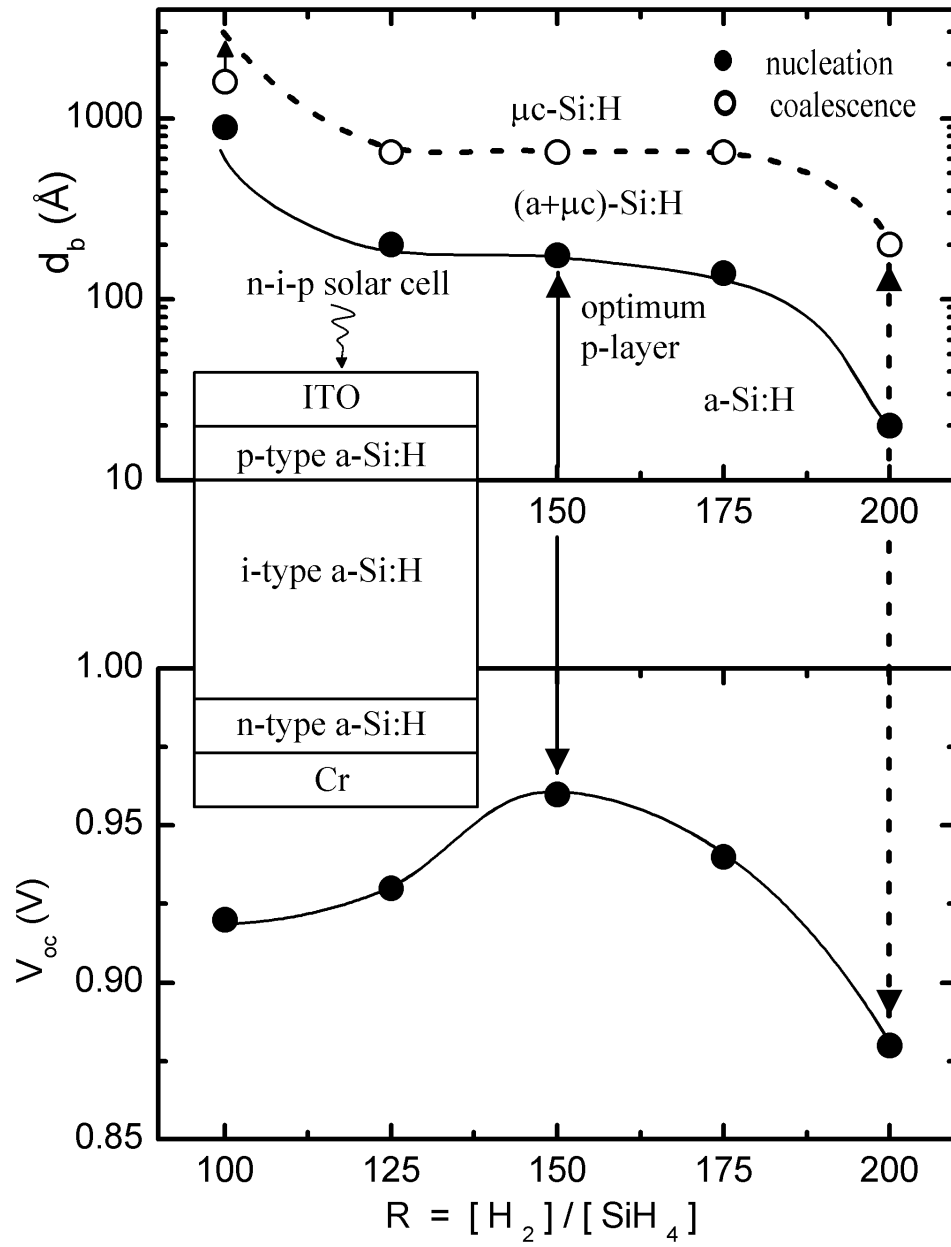


**Figure 4.** Extended phase diagram for  $D=0.2$ , p-Si:H as a function of  $R$  and thickness. Also shown is the 1 sun  $V_{oc}$  for cells with corresponding  $\sim 200$  Å p-layers.



**Figure 5.** A 1  $\mu\text{m}$  x 1  $\mu\text{m}$  AFM image of an optimized protocrystalline p-layer

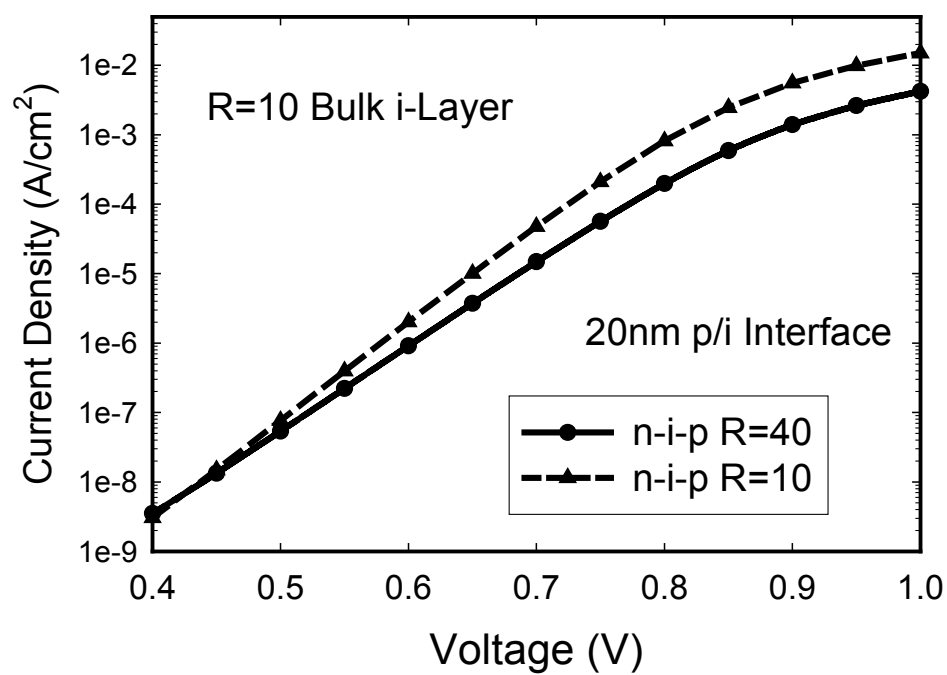


**Figure 6.** The  $J_D$ -V characteristics for p-a-SiC:H n-i-p cells with different p/i interface regions

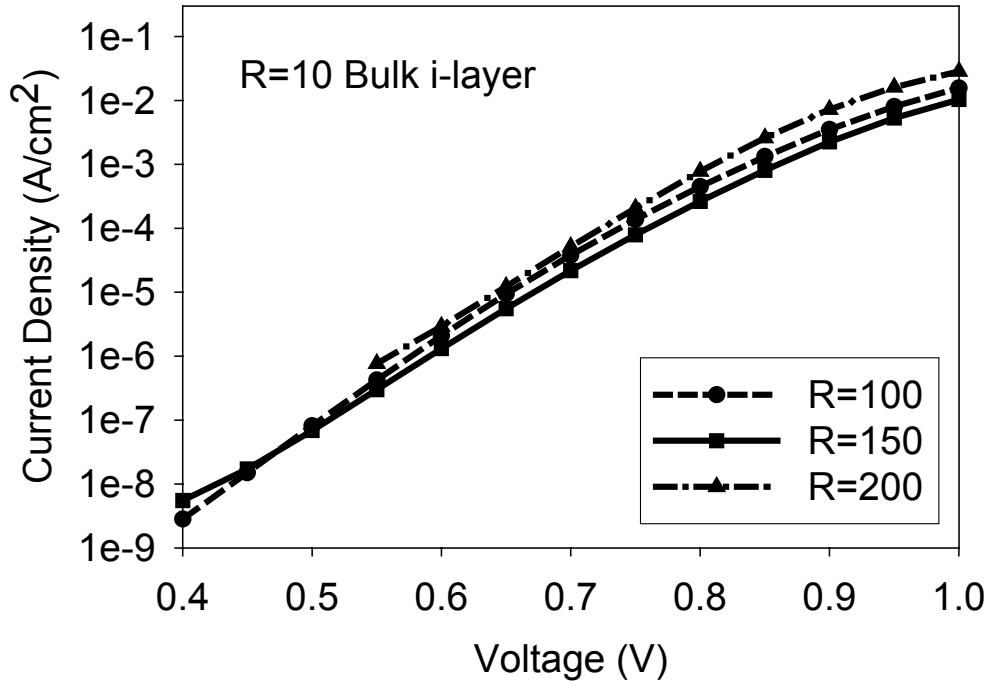


**Figure 7.**  $J_D$ -V characteristics of highly-diluted p-Si:H n-i-p cells with  $D=0.2$  for different R.

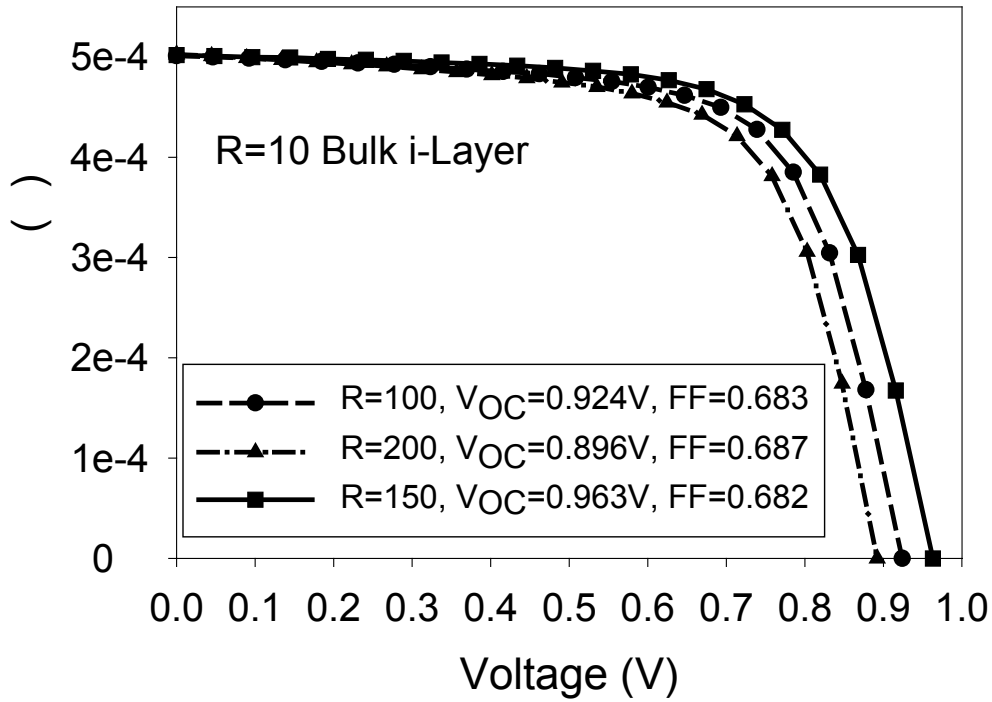


**Figure 8.** Current-Voltage characteristics under 1 sun illumination for n-i-p solar cells having p-layers prepared with  $D=0.2$  and with R values of 100, 150 and 200.

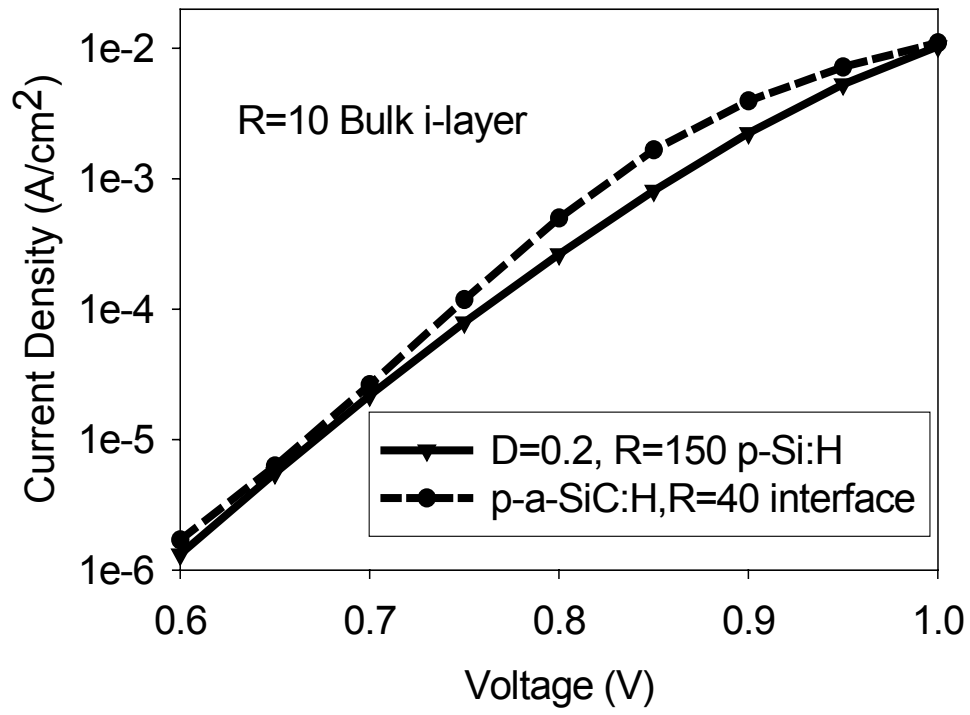


**Figure 9.**  $J_D$ -V characteristics of the best protocrystalline p-Si:H and p a-SiC:H cells.

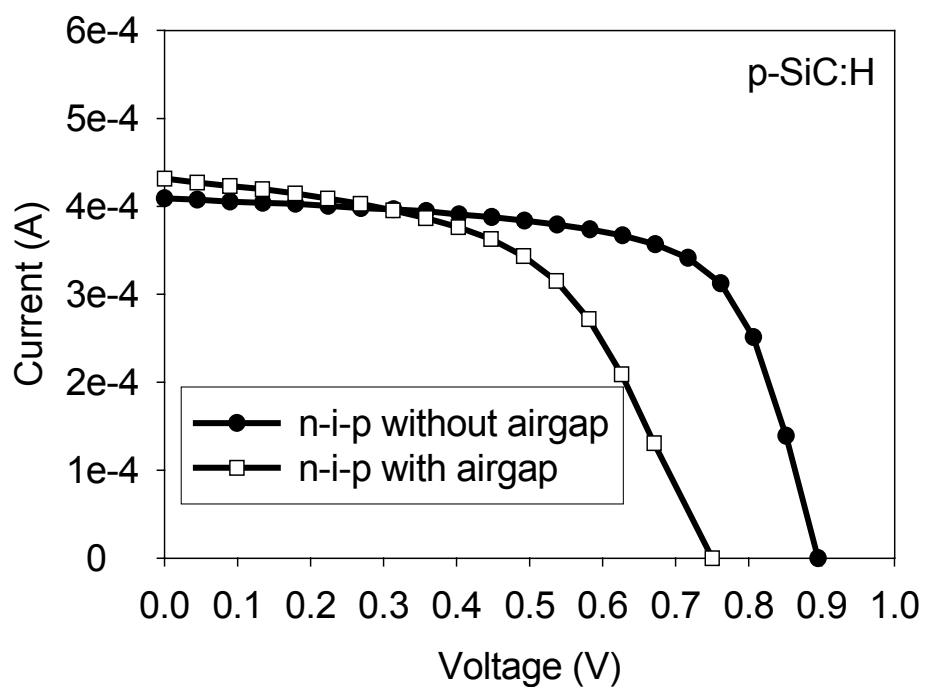


**Figure 10a.** 1 sun light I-V characteristics of p-SiC:H n-i-p solar cells with and without a vacuum break between the deposition of the i- and p-layers.

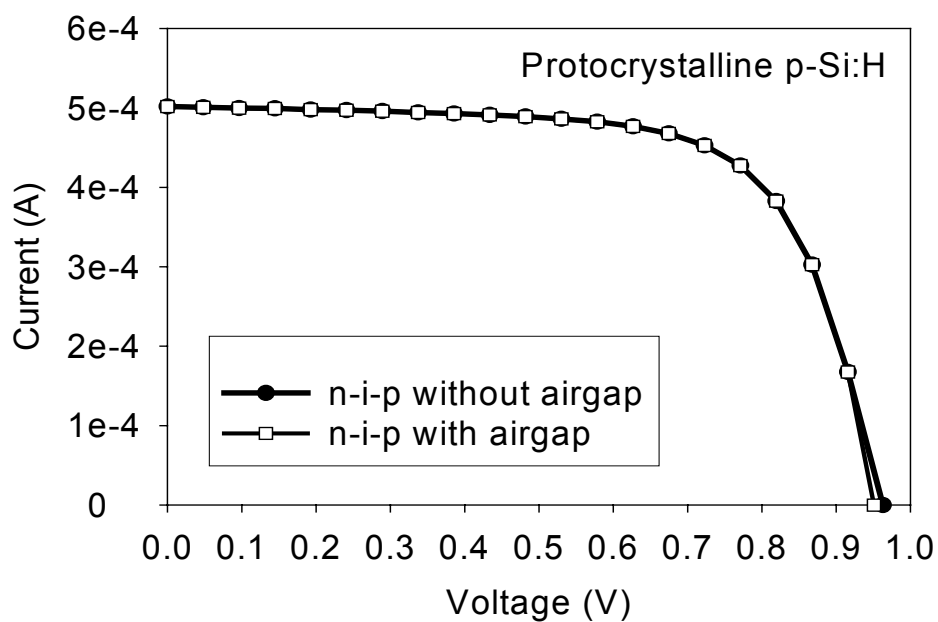


**Figure 10b.** 1 sun light I-V characteristics of protocrystalline-p n-i-p solar cells with and without a vacuum break between the deposition of the i- and p-layers.

## Task 2

### Process Deposition Phase Diagrams for the Optimization of a-Si:H-Based Materials and Solar Cells

The deposition phase diagram describes the accumulated thicknesses at which different microstructural and phase transitions are observed during the Si:H film growth process. In such a diagram, the transition thicknesses are plotted as continuous functions of a key deposition parameter. In low temperature PECVD, the  $H_2$ -dilution gas flow ratio  $R=[H_2]/[SiH_4]$  is used as the abscissa of the phase diagram since it exerts the greatest control over the phase of the film -- from a-Si:H at low  $R$  to  $\mu$ c-Si:H at high  $R$ . Over a wide range in  $R$ , however, Si microcrystallites have been observed to nucleate from within the growing a-Si:H phase after a critical phase-transition thickness that decreases with increasing  $R$ . As a result, the amorphous-to-(mixed-phase microcrystalline)  $[a \rightarrow (a+\mu c)]$  transition boundary is not vertical, but instead exhibits a negative slope vs.  $R$  in the  $R$ - $d_b$  plane, where  $d_b$  designates the bulk layer thickness. This in turn implies that the optimum preparation procedures for the a-Si:H and  $\mu$ c-Si:H i-layers depend on the desired thickness of the i-layers, and paves the way for multi-step optimization<sup>13</sup>.

The phase diagrams have led to the concept of *protocrystalline* Si:H deposition. There are three important characteristics of this film growth regime<sup>14</sup>.

- (1) As its name implies, the protocrystalline growth regime is one in which a-Si:H is deposited initially, but given sufficient accumulated thickness, microcrystallites nucleate from the amorphous phase. Thus, the growing film will ultimately evolve first to mixed-phase  $(a+\mu c)$ -Si:H and finally to single-phase  $\mu$ c-Si:H. Once the  $a \rightarrow (a+\mu c)$  transition is detected, however, the growing material is no longer considered protocrystalline.
- (2) A second characteristic of the protocrystalline growth regime is the substrate dependence of the phase of the growing material. If the Si:H film grows in the protocrystalline regime on a freshly-deposited amorphous film substrate (such as  $R=0$  a-Si:H), the same deposition conditions would lead to single-phase microcrystalline silicon growth on a freshly-deposited  $\mu$ c-Si:H substrate film. Thus, under protocrystalline growth conditions, local epitaxy is favored on a c-Si substrate; however, crystallite nucleation is suppressed on an amorphous substrate.
- (3) A third characteristic of the protocrystalline growth regime is the observed enhanced degree of nuclei coalescence that yields the smoothest surfaces among a-Si:H films. Thus, the dielectric discontinuity between the ambient and bulk film is sharpest under protocrystalline growth conditions. Such a characteristic can best be detected, however, by using oxide-covered c-Si wafer substrates. (The presence of the oxide suppresses Si crystallite nucleation in the protocrystalline regime relative to clean c-Si or  $\mu$ c-Si:H so that the protocrystalline state can be observed.) By using c-Si substrates, the very smooth wafer surfaces prevent the development of substrate-induced roughness in the film that masks the nuclei coalescence behavior.

In addition to the unique evolutionary growth behavior exhibited under the protocrystalline Si:H deposition conditions, the protocrystalline material itself exhibits unique optoelectronic properties when deposited under optimized low rf plasma power conditions. These properties are often difficult to measure because one must use the

<sup>13</sup> J. Koh, Y. Lee, H. Fujiwara, C. R. Wronski, and R. W. Collins, Appl. Phys. Lett. **73** (1998) 1526.

<sup>14</sup> Y. Lu, S. Kim, M. Gunes, Y. Lee, C. R. Wronski, and R. W. Collins, Mater. Res. Soc. Symp. Proc. **336** (1994) 595.

appropriate substrate and thickness to ensure that the film is protocrystalline throughout its thickness and has not crossed the  $a \rightarrow (a+\mu c)$  transition during the growth process. First, the optical gaps of protocrystalline Si:H are larger than conventional materials due to the increase in gap with increasing  $H_2$ -dilution ratio  $R$ . In addition, the width of the broad Lorentzian-shaped peak in the imaginary part of the dielectric function  $\epsilon_2$  is narrower in protocrystalline Si:H than in conventional a-Si:H materials. This suggests that the relaxation time of the excited electron and hole in the bands is the longest. The Si bond-packing density is not the highest in protocrystalline Si:H, however, suggesting the presence of voids that are observed to increase in density with increasing  $R$ . Apparently these voids are not detrimental to the electronic properties. Perhaps the key feature of the protocrystalline Si:H is its relative stability to light induced degradation, as observed for films in their electron mobility-lifetime products and similarly for solar cells in their fill factors.

## Overview

Figure 11 shows the overlying surface roughness layer thickness  $d_s$  versus the bulk layer thickness  $d_b$  for three Si:H depositions as deduced by RTSE using a rotating compensator multichannel ellipsometer. The depositions include (a) two i-layers, one prepared at  $R=0$  and the other at  $R=10$ , that remain single-phase a-Si:H throughout growth, and (b) an i-layer prepared at  $R=20$  that evolves through all three growth regimes: first single-phase a-Si:H, then mixed-phase  $(a+\mu c)$ -Si:H, and finally single-phase  $\mu c$ -Si:H. For these three depositions, the substrates were c-Si wafers with intact native oxides, held at a temperature of  $T=200^\circ\text{C}$ . The rf power was set at  $P=0.08\text{ W/cm}^2$ , the lowest level for a stable plasma. A low partial pressure of  $\text{SiH}_4$  within the range of  $p(\text{SiH}_4)=0.03\text{--}0.07\text{ Torr}$  was maintained versus  $R$ ; thus, the total pressure increased from  $p_{\text{tot}}=0.07\text{ Torr}$  for  $R=0$  to  $p_{\text{tot}}=0.9\text{ Torr}$  for  $R=40$ . With this combination of variables, the a-Si:H deposition rates were  $\sim 1.2\text{ \AA/s}$  at  $R=0$  and  $0.5\text{ \AA/s}$  at  $R=10$  just before the transition to mixed-phase  $(a+\mu c)$ -Si:H deposition for a thick layer.

The smoothening behavior in the first  $\sim 100\text{ \AA}$  of film growth for all three depositions in Fig. 11 is attributed to the coalescence of initial amorphous nuclei that form as clusters on the c-Si substrates. A detailed understanding of this process has been established previously<sup>15,16</sup>. The weak roughening onset at  $d_b \sim 250\text{ \AA}$  for the  $R=0$  a-Si:H film in Fig. 11(a) corresponds to a surface morphological transition versus  $d_b$ , but without a change in the phase of the growing film. As a result, this transition is denoted as "a $\rightarrow$ a" to indicate that the film is a-Si:H on both sides of the transition. For this  $R=0$  film, a simple two-layer [(uniform-bulk)/(surface-roughness)] optical model was applied to analyze the RTSE data set. For the  $R=20$  film in Fig. 11(b), the roughening onset at  $d_b \sim 300\text{ \AA}$  corresponds instead to the  $a \rightarrow (a+\mu c)$  transition, and the smoothening onset near  $d_b \sim 1900\text{ \AA}$  corresponds to the  $(a+\mu c) \rightarrow \mu c$  transition. For this film, an optical model with a graded bulk layer was applied to analyze the RTSE data set, as will be described in greater detail later. For the  $R=10$  deposition in Fig. 11(a), a stable surface is observed after initial nuclei coalescence (i.e., for  $d_b > 100\text{ \AA}$ ), indicating that any roughening onset

<sup>7</sup> R. W. Collins in: H. Fritzsche, ed., *Amorphous Silicon and Related Materials* Vol. 1B (World Scientific, Singapore, 1988) 1003

<sup>16</sup> J. Koh, A. S. Ferlauto, P. I. Rovira, C. R. Wronski, and R. W. Collins, *Appl. Phys. Lett.* **75** 2286 (1999).

due to the  $a \rightarrow a$  or the  $a \rightarrow (a + \mu c)$  transition must occur for  $d_b > 4000 \text{ \AA}$ , i.e., greater than the typical thicknesses of the i-layers used in a-Si:H solar cells. Thus, the RTSE data analysis for the  $R=10$  deposition proceeded in the same way as that for the  $R=0$  deposition.

The general features of the microstructural and phase evolution as deduced from the analysis of RTSE data such as those of Fig. 11 are enumerated (I-VI) with further details as follows.

(I) *Coalescence of initial amorphous nuclei.* Coalescence of nucleation-induced microstructure is observed as a smoothening effect during a-Si:H film growth in the first  $\sim 100 \text{ \AA}$  of bulk layer thickness. The magnitude of this smoothening effect can be characterized by  $\Delta d_s = d_s(2.5 \text{ \AA}) - d_s(100 \text{ \AA})$  [where  $d_s(x)$  is the value of  $d_s$  when  $d_b = x$ ]. The value of  $\Delta d_s$  increases with increasing  $R$  in general; thus, the maximum  $\Delta d_s$  values are observed for protocrystalline Si:H. This material exhibits the highest electronic performance for applications as i-layers in solar cells -- as long as protocrystalline growth is maintained throughout deposition to the desired thickness. An increase in  $\Delta d_s$  has been proposed to reflect an increase in the surface diffusion length of the adsorbed radicals that form the film<sup>17</sup>.

(II) *Coalescence of initial microcrystalline nuclei.* An even larger smoothening effect can be observed upon structural coalescence of clusters that nucleate directly on the substrate as microcrystalline silicon ( $\mu c$ -Si:H). This larger effect can be observed for depositions at higher  $R$  values than those depicted in Fig. 11. In this case, a much larger  $d_s$  value is typically observed at the onset of bulk layer growth ( $\sim 45\text{-}60 \text{ \AA}$  vs.  $15\text{-}20 \text{ \AA}$ , for a-Si:H nucleation), due to a lower initial nucleation density compared to that of the a-Si:H films. The physical mechanisms that control amorphous and microcrystalline cluster coalescence are likely to be different (e.g., surface diffusion vs. competitive space filling, respectively).

(III) *Stable surface growth.* Under a narrowly-defined set of deposition conditions [specifically, in Fig. 11(a) for  $R=10$ ,  $T=200^\circ\text{C}$ , and minimum rf plasma power  $P=0.08 \text{ W/cm}^2$ ], the a-Si:H surface remains smooth and stable with  $< 1 \text{ \AA}$  change in the roughness layer thickness from the end of coalescence throughout thick film growth, e.g., from 100 to 4000  $\text{\AA}$  in the example of Fig. 11(a). When the stable surface regime is present, it is found to occur at an  $R$  value just prior to the  $a \rightarrow (a + \mu c)$  transition for thick films. Under these conditions, highest performance and stability i-layer materials for solar cells are obtained.

(IV) *Amorphous roughening transition.* If one starts with a deposition exhibiting the stable-surface conditions, for example ( $R=10$ ,  $T=200^\circ\text{C}$ ,  $P=0.08 \text{ W/cm}^2$ ) in Fig. 11(a), and gradually decreases  $R$  or increases  $P$  in successive depositions so that the material properties and stability degrade, then a roughening transition is detected that gradually shifts to lower  $d_b$  in the successive depositions. The growing film is amorphous on both sides of the transition, and the associated surface microstructural changes are correlated with reductions in the performance and stability of such films as i-layers in solar cells. A shift in the  $a \rightarrow a$  roughening transition to lower  $d_b$  appears to reflect a reduction in the surface diffusion length of the adsorbed radicals.

<sup>17</sup> Y. Li, I. An, H. V. Nguyen, C. R. Wronski, and R. W. Collins, Phys. Rev. Lett. **68** (1992) 2814.

(V) *Amorphous-to-(mixed-phase-microcrystalline) (a+ $\mu$ c) transition.* At moderate to high values of R, however, a different type of roughening transition is observed in which crystallites nucleate from the growing amorphous phase. Because the nucleation density is usually low and the crystallites grow preferentially, the crystalline protrusions generate a surface roughness layer that increases rapidly in thickness with  $d_b$ . Once the growing film crosses this transition and the crystallite volume fraction exceeds a critical value, the material becomes unsuitable as an i-layer component of an a-Si:H-based solar cell.

(VI) *(Mixed-phase)-to-(single-phase-microcrystalline) transition.* For thin films that have already undergone the a $\rightarrow$ (a+ $\mu$ c) transition, a second transition is possible that occurs at even greater bulk layer thickness. In this transition, the crystalline protrusions that extend above the surface have become large enough to make contact, leading to a crystallite coalescence process with continued film growth. This process is manifested in the data as a transition from surface roughening to smoothening during mixed-phase film growth. Once the crystallites have coalesced to cover the growing film surface completely, single-phase  $\mu$ c-Si:H growth proceeds with a resumption of surface roughening. For optimum  $\mu$ c-Si:H i-layers in solar cells, one generally seeks to deposit the film using the lowest R value possible while maintaining the film within the microcrystalline growth regime throughout the deposition<sup>18,19</sup>.

The first phase diagrams developed to guide a-Si:H deposition vs. R included only feature (V), i.e., the amorphous-to-(mixed-phase-microcrystalline) (a+ $\mu$ c) transition<sup>1,4</sup>. More recently features (IV), (V), and (VI) in the above paragraphs have been included in so-called *extended* phase diagrams that provide deeper insights into the electronic quality of a-Si:H prepared near the a $\rightarrow$ (a+ $\mu$ c) transition, as well as provide the thickness ranges and conditions under which single-phase  $\mu$ c-Si:H films are obtained<sup>20,21</sup>.

### Amorphous Roughening Transition during Film Growth

In the first part of this section, it is demonstrated that the R=0 and R=10 a-Si:H films [Fig. 12(a)] can be described correctly in terms of a two-layer optical model [(uniform bulk)/(surface roughness)]. As a result, the roughening transition observed for the R=0 film describes a surface morphological transition without an evolution of the bulk properties of the growing material across the transition.

Figure 12(a) shows the unbiased estimator of the mean square deviation between the experimental and best fit ellipsometric spectra (1.5 - 4.7 eV) versus bulk layer thickness for the R=0 and R=10 depositions of Fig. 12(a). The unbiased estimator describes the quality of the best fit to the RTSE data, whereby the fit is based on the assumption of a two-layer optical model [(uniform bulk)/(surface roughness)] with a thickness-independent bulk layer dielectric function. This dielectric function is extracted by numerical inversion near  $d_b=200$  Å – thus, the fit is nearly perfect for that thickness. Figure 12(a) shows that the fits remain good throughout the deposition process (for

<sup>18</sup> O. Vetterl, F. Finger, R. Carius, P. Hapke, L. Houben, O. Kluth, A. Lambertz, A. Muck, B. Rech, and H. Wagner, Sol. Energy Mater. Sol. Cells **62** (2000) 97.

<sup>19</sup> O. Vetterl, R. Carius, L. Houben, C. Scholten, M. Luysberg, A. Lambertz, F. Finger, and H. Wagner, Mater. Res. Soc. Symp. Proc. **609** (2000) A15.2.1.

<sup>20</sup> A. S. Ferlauto, P. I. Rovira, R. J. Koval, C. R. Wronski, and R. W. Collins, Mater. Res. Soc. Symp. Proc. **609** (2000) A2.2.1.

<sup>21</sup> A. S. Ferlauto, R. J. Koval, C. R. Wronski, and R. W. Collins, Appl. Phys. Lett. **80** (2002) 2666.

comparison see the  $R=20$  deposition of the lower panel), with the result for the  $R=10$  deposition exhibiting the best characteristics. It is concluded that the two-layer model is a close description of reality for the  $R=0$  and  $R=10$  films.

The results in Fig. 12 support the validity of our conclusions based on the statistical data in Fig. 11(a). Figure 13 shows dielectric functions for the  $R=0$  film extracted at two different bulk layer thicknesses,  $d_b=200$  Å (solid line) and  $d_b=1965$  Å (broken line), before and after the  $a \rightarrow a$  transition in the growth process. The results nearly superimpose on the scale of the figure and demonstrate explicitly that the properties of the a-Si:H film are nearly the same above and below the  $a \rightarrow a$  roughening transition. The small differences in Fig. 13, and hence the gradual increase in the biased estimator in Fig. 12, may be attributable to a slightly higher H content in the film near the substrate interface, but this effect is not directly related to the roughening transition.

Next, it is important to emphasize the key role of the  $a \rightarrow a$  roughening transition in the a-Si:H film deposition process and demonstrate typical results as a function of the deposition variable  $R$ . Figure 14 shows the surface roughness evolution as a function of bulk layer thickness for two series of a-Si:H films both deposited on c-Si substrates at  $T=200^\circ\text{C}$ . The first series in Fig. 14(a) employs the conditions of Fig. 11 with minimum power [ $P=0.08$  W/cm<sup>2</sup>] and low SiH<sub>4</sub> partial pressure [ $p(\text{SiH}_4)=0.03\text{--}0.07$  Torr;  $p_{\text{tot}}<0.5$  Torr], and the second series in Fig. 14(b) employs elevated power [ $P=0.34$  W/cm<sup>2</sup>] and high total pressure ( $p_{\text{tot}}=4$  Torr). For the latter series, the total pressure is controlled, rather than the partial pressure of SiH<sub>4</sub> as in the series of Figs. 11 and 14(a). With the combination of variables used for Fig. 14(b), the deposition rate is 3.4 Å/s for an i-layer at the maximum  $R$  value of 60 just before the onset of mixed-phase ( $a+\mu\text{c}$ )-Si:H deposition (assuming a desired 4000 Å thickness). This rate is a factor of  $\sim 7$  higher than that obtained at the corresponding maximum  $R$  value ( $R=10$ ) under the lowest power, low pressure conditions for the depositions of Fig. 14(a). In both parts of Fig. 14, an  $a \rightarrow a$  roughening transition is clearly observed for each deposition, and this transition shifts to increasing bulk layer thickness with increasing  $R$ . In fact in Fig. 14(b) at  $R=60$ , just before the  $a \rightarrow (a+\mu\text{c})$  transition, the surface of the film is stable to a bulk layer thickness of  $d_b \sim 3000$  Å.

The shapes of the curves in Fig. 14, and the development of features (I), (III), and (IV) above can be understood from continuum models of film growth in the following general way (see, e.g., <sup>17-20</sup>). Low amplitude surface modulations  $A(\lambda, t)$  of spatial wavelength  $\lambda$  less than a critical value ( $\lambda_0$ ) are unstable and decay as a function of time  $t$  (or thickness) according to  $A(\lambda, t) \sim A_0(\lambda) \exp\{\omega(\lambda)t\}$ , where  $\omega(\lambda) < 0$  for  $\lambda < \lambda_0$ . Features with  $\lambda > \lambda_0$ , such that  $\omega(\lambda) > 0$ , are enhanced (until the low amplitude approximation breaks down). Typically, the highest rate of enhancement occurs for features with wavelength just above  $\lambda_0$ , and the development of features with this correlation length generates the  $a \rightarrow a$  roughening transition. Under most deposition conditions, the correlation length associated with the initial nuclei is less than  $\lambda_0$  and the smoothening of these surface features generates feature (I) described above.

In more specific models, the smoothening effects can be attributed to a *chemical* vapor deposition (CVD) effect, specifically surface diffusion which exhibits a  $(-a_4\lambda^{-4})$  term in  $\omega(\lambda)$ , and the roughening effects can be attributed to a *physical* vapor deposition (PVD) effect, specifically shadowing due to the atomic size which exhibits a  $(+a_2\lambda^{-2})$

term in  $\omega(\lambda)^{22,23}$ . Considering a simple model with only these two sources of roughness evolution, the diffusion length  $L$  is determined by the balance of the two terms (i.e., by  $\omega=0$  or  $L=\lambda_0$ ). In more complicated models, the diffusion length does not enter in such a straightforward manner<sup>24,25</sup>. In any case, when the surface diffusion length increases in the a-Si:H deposition process, the onset of roughening shifts to longer times or greater thicknesses, and this correlates with observed improvements in the electronic properties of the films. Although advances in understanding a-Si:H film growth have been made over the years<sup>26</sup>, uncertainties continue to exist concerning the diffusion mechanisms<sup>27</sup>. In spite of these uncertainties, it has become increasingly clear from the RTSE studies that the longest precursor diffusion lengths are associated with the highest electronic quality and highest stability materials.

### Crystalline Silicon Wafers and Amorphous Silicon Film Substrates

The extended phase diagram is depicted in Fig. 15 for Si:H growth on oxide-covered c-Si wafer substrates held at 200°C. This diagram was deduced from results including those in Fig. 11, and so is appropriate for Si:H depositions at low rf power ( $P=0.08$  W/cm<sup>2</sup>) and a low, nearly constant, partial pressure of SiH<sub>4</sub> [ $p(\text{SiH}_4) = 0.03\text{--}0.07$  Torr]. The diagram of Fig. 15 shows the bulk layer thicknesses at which the  $a \rightarrow a$ ,  $a \rightarrow (a+\mu\text{c})$ , and  $(a+\mu\text{c}) \rightarrow \mu\text{c}$  transitions occur as functions of  $R$  (lines). For  $R < 10$ , the thicknesses corresponding to the  $a \rightarrow a$  transition provide insights into the quality of the a-Si:H, irrespective of the substrate. As suggested by the discussion above, larger  $a \rightarrow a$  transition thicknesses imply longer precursor surface diffusion lengths in the growth process and, thus, higher quality a-Si:H materials for the i-layers of solar cells. In fact, the highest electronic quality material is prepared in the narrow region near  $R=10$  where the a-Si:H surface remains stable throughout the entire deposition to 4000 Å [see Fig. 11(a)]. (The short upward and downward pointing arrows in Fig. 15 indicate transitions that occur at thicknesses above and below the indicated values.)

The a-Si:H prepared at  $R=10$  can be identified as protocrystalline Si:H owing to the fact that if the film were to continue accumulating, then the  $a \rightarrow (a+\mu\text{c})$  transition would eventually be traversed as suggested by ex situ measurements of films  $> 1$  μm thick. Furthermore, if the  $R=10$  deposition is performed on a single-phase μc-Si:H substrate (rather than on oxide-covered c-Si as in Fig. 15), then the μc-Si:H phase would continue to propagate. Only by reducing  $R$  to 5 (outside the protocrystalline growth regime) can one effectively suppress the μc-Si:H phase.

From the discussion of the previous paragraph, it is evident that for  $R \geq 10$  in Fig. 15, the phase evolution is very sensitive to the nature of the substrate, and in this deposition regime it is important to consider substrates that correspond more closely to the a-Si<sub>1-x</sub>C<sub>x</sub>:H p-layer often used for p-i-n cells (or the a-Si:H n-layer often used for n-i-p cells). Figure 16 shows the corresponding extended phase diagram for an  $R=0$  a-Si:H substrate. This substrate is relevant when considering the optimization of i-layers for devices. However, the starting roughness on the a-Si:H substrate makes it difficult to

<sup>22</sup> A. Mazor, D. J. Srolovitz, P. S. Hagan, and B. G. Bukiet, Phys. Rev. Lett. **60** (1988) 424

<sup>23</sup> R. W. Collins and B.-Y. Yang, J. Vac. Sci. Technol. B **7** (1989) 1155.

<sup>24</sup> W. M. Tong and R. S. Williams, Annu. Rev. Phys. Chem. **45** (1994) 401.

<sup>25</sup> B. J. Palmer and R. G. Gordon, Thin Solid Films **158** (1988) 313.

<sup>26</sup> A. Matsuda, J. Vac. Sci. Technol. A **16** (1998) 365.

<sup>27</sup> J. Robertson, J. Appl. Phys. **87** (2000) 2608.

detect the weak  $a \rightarrow a$  roughening transition at low  $R$  as in Figs. 11(a) and 15. As a result, this transition is not shown in Fig. 16. Fortunately, insights in this region of low  $R$  can be obtained from the analyses of depositions on c-Si substrates, owing to the relative substrate independence of the a-Si:H growth process at the lower  $R$  values.

A comparison of Figs. 15 and 16 show clearly the substrate dependence of the phase evolution of the Si:H films. First, at the lowest  $R$  for which the  $a \rightarrow (a+\mu c)$  is detected,  $R=15$ , this transition occurs at a lower thickness for the c-Si substrate (1500 Å for c-Si vs. 3000 Å for the  $R=0$  a-Si:H substrate film). This suggests a higher microcrystallite nucleation density from the amorphous phase when deposition is performed on c-Si. This effect is preserved with increasing  $R$ . For  $R=40$ , microcrystallites nucleate immediately on the c-Si wafer substrate without an a-Si:H interlayer; however, the  $a \rightarrow (a+\mu c)$ , and  $(a+\mu c) \rightarrow \mu c$  transitions occur near 200 and 750 Å for the  $R=0$  a-Si:H film substrate, respectively. Overall the thickness and substrate dependences of the film properties, as well as the graded structures of films that enter the mixed-phase growth regime, lead to difficulties in characterizing the basic properties of the optimum solar cell materials. Under such conditions, identical layer thicknesses and similar substrates must be employed for both the materials and the device structures.

### Optimization Principles for Optimum Solar Cell Fabrication

In Fig. 16, the optimum one-step i-layers for solar cells are prepared in the protocrystalline regime at the maximum possible  $R$  value while avoiding the  $a \rightarrow (a+\mu c)$  transition for the desired thickness. Thus, it is important to emphasize that the optimum conditions of i-layer deposition depend on the desired thickness. In fact, this is one of the most important insights provided by RTSE measurements and the resulting deposition phase diagrams that had not been fully appreciated in previous studies. Returning to Fig. 16, the optimum  $H_2$ -dilution for an i-layer thickness of 4000 Å corresponds to  $R \sim 10$ , the stable surface growth condition in Figs. 11(a) and 15. Figure 16 also demonstrates how optimum two-step i-layers 4000 Å thick can be designed for p-i-n cells on the basis of the phase diagram (see long vertical arrows). These steps include a 200 Å  $R=40$  i-layer at the interface to the p-layer, followed by a 3800 Å thick bulk i-layer with  $R=10$ . This two-step i-layer provides the highest product of open-circuit voltage ( $V_{oc}$ ) and fill factor (FF) in both the annealed and fully light-soaked states (see Fig. 17 for device results).

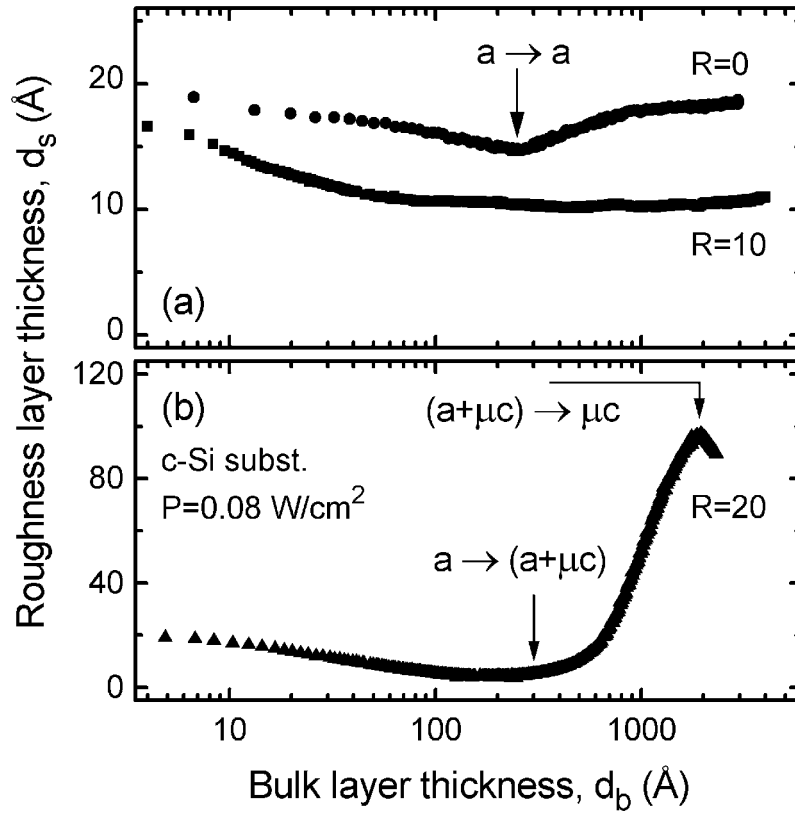
It is important to note, however, that the application of a single phase boundary as in Fig. 16 for guiding the two-step i-layer is an oversimplification. In fact, upon deposition of the  $R=40$  i-layer, the phase boundary for the subsequent  $R=10$  i-layer deposition is shifted to somewhat lower  $R$  compared with that for the  $R=0$  substrate film. This effect arises owing to the substrate dependence of the phase boundary. The  $R=40$  layer is more ordered than the  $R=0$  layer, and this appears to promote a more ordered  $R=10$  layer, and as a result, the  $a \rightarrow (a+\mu c)$  transition occurs at lower  $d_b$  for fixed  $R$ . The  $R=10$  value for the second step i-layer is sufficiently low, however, to avoid being affected by this shift.

Figure 17 demonstrates more clearly the one-step and two-step optimization processes for a-Si:H p-i-n solar cells. This figure depicts  $V_{oc}$  and FF, the latter in both the annealed state (circles) and after degradation with 1 sun for 100 hours (squares), for Si:H p-i-n solar cells incorporating one-step (4000 Å) i-layers plotted as a function of i-layer  $R$  (open symbols) and for cells incorporating two-step (100-200 Å / 3900-3800 Å) interface/bulk i-layers plotted as a function of interface i-layer  $R$  (closed symbols). The

vertical lines denote the  $R$  values corresponding to the  $a \rightarrow (a+\mu c)$  transitions for the bulk  $i$ -layer with  $d_b=4000$  Å (left) and for the interface  $i$ -layer with  $d_b=200$  Å (right). In fact,  $V_{oc}$  increases with increasing  $R$  for the near-interface material as long as the  $a \rightarrow (a+\mu c)$  transition is not traversed. This effect is believed to be due to two mechanisms, namely the widening of the gap and the narrowing of the band tails with increasing  $R$  for the protocrystalline materials. This interpretation is supported by the Kramers-Kronig consistent analysis of the dielectric functions which reveals the former mechanism directly, and the latter indirectly through a narrowing of the Lorentz oscillator component of the protocrystalline Si:H dielectric function. Details of such analyses appear elsewhere<sup>28</sup>. The decreases in  $V_{oc}$  and FF that occur for the one-step and two-step  $i$ -layers for  $R$  values above these transition lines are attributed to the development of microcrystallinity in the bulk and interface  $i$ -layers with increasing thickness. Thus, Fig. 17 clearly demonstrates that the optimum  $i$ -layers in one-step and two-step solar cells are deposited at the maximum possible  $R$  value that can be sustained without crossing the  $a \rightarrow (a+\mu c)$  transition for the desired thickness.

---

<sup>28</sup> A. S. Ferlauto, J. Koh, P. I. Rovira, C. R. Wronski, R. W. Collins, and G. Ganguly, *J. Non-Cryst. Solids* **266-269** (2000) 269.



**Figure 11.** Surface roughness layer thickness ( $d_s$ ) versus bulk layer thickness ( $d_b$ ) from RTSE data collected during the deposition of (a) uniform a-Si:H with  $R=0$  and  $R=10$ , and (b) structurally-graded  $(a \rightarrow \mu c)$ -Si:H with  $R=20$ , all on c-Si substrates held at  $200^\circ\text{C}$ .

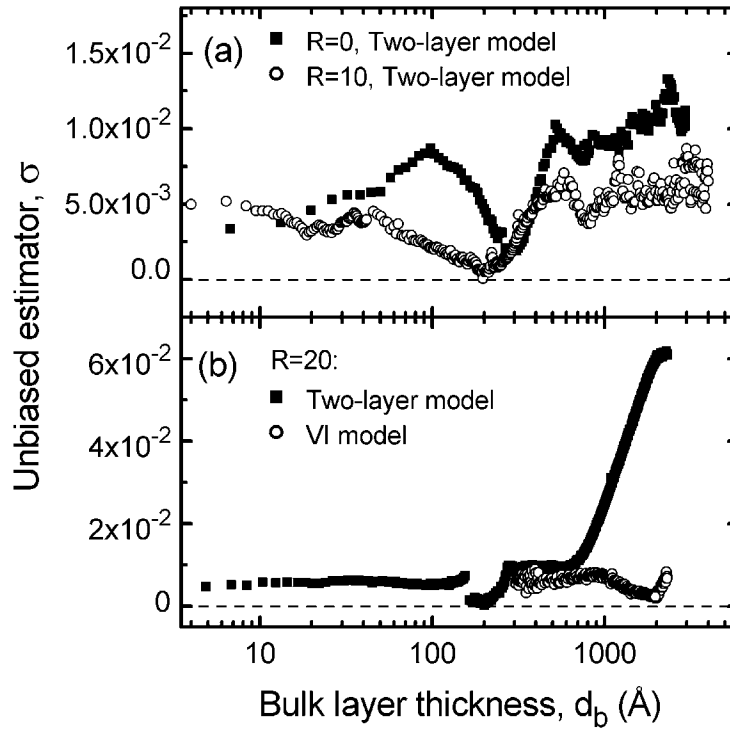


**Figure 12.** Unbiased estimator of the mean square deviation versus time obtained in the RTSE analyses of (a) the uniform R=0 and R=10 a-Si:H films of Fig. 11(a) applying a conventional two-layer optical model, and (b) the graded R=20 Si:H film of Fig. 11(b) applying a two-layer virtual interface model. Also shown in (b) are results obtained when the conventional two-layer model is applied to the R=20 film.

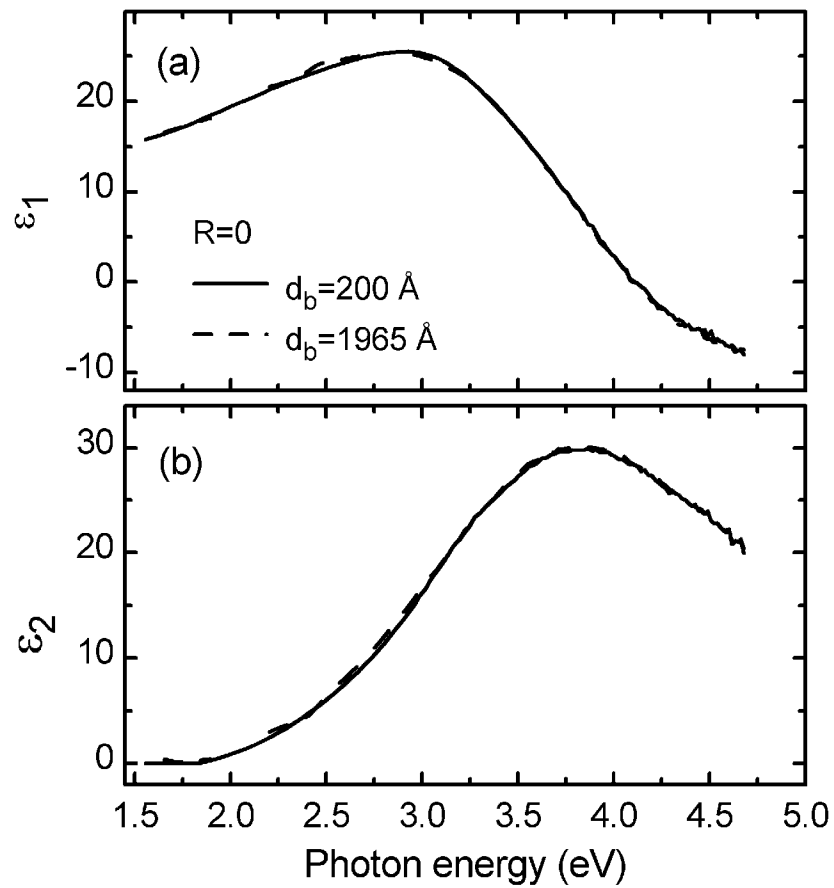


**Figure 13.** (a) Real and (b) imaginary parts of the dielectric functions at 200°C for the  $R=0$  a-Si:H film deposited on c-Si from Fig. 11(a). These results were obtained by RTSE, applying a conventional two-layer model and exact inversion at the thicknesses indicated.

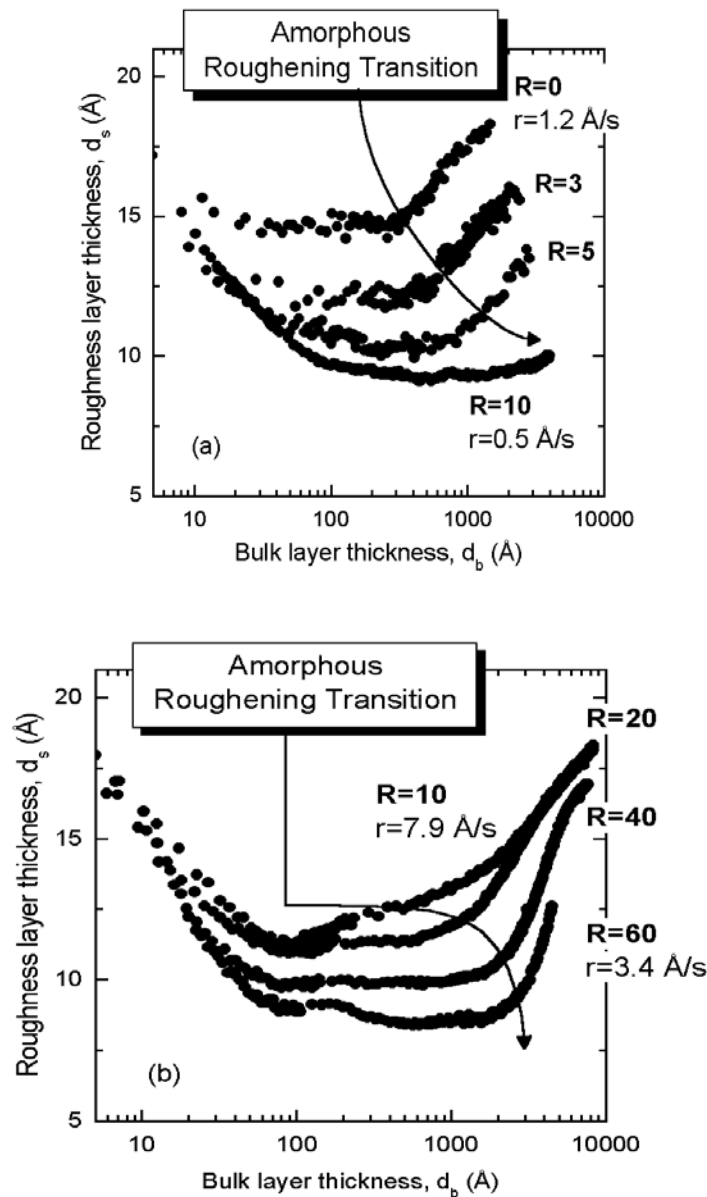


**Figure 14.** Surface roughness layer thickness ( $d_s$ ) versus bulk layer thickness ( $d_b$ ) for two series of a-Si:H films both deposited on c-Si substrates at  $T=200^\circ\text{C}$ . In (a), the conditions of Fig. 11 are employed, i.e., minimum rf plasma power [ $P=0.08$  W/cm<sup>2</sup>] and low SiH<sub>4</sub> partial pressures [ $p(\text{SiH}_4)=0.03\text{--}0.07$  Torr;  $p_{\text{tot}}<0.5$  Torr]. In (b), elevated power [ $P=0.34$  W/cm<sup>2</sup>] and a high total pressure [ $p_{\text{tot}}=4$  Torr] are employed.

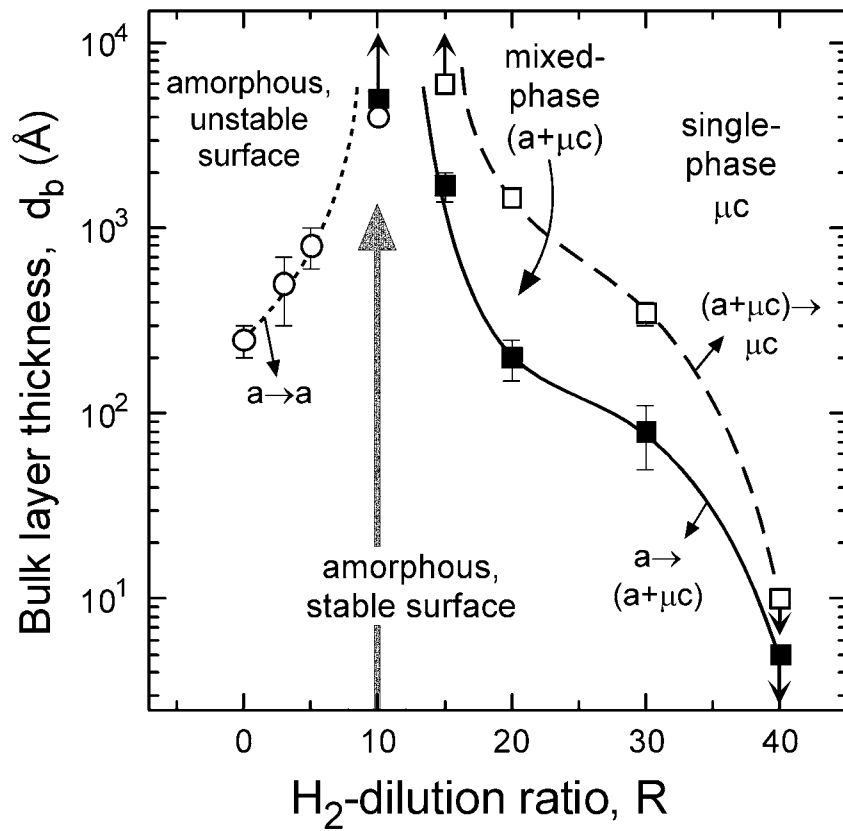


**Figure 15.** Extended phase diagram in the plane of  $R$  and  $d_b$  for PECVD Si:H prepared at a low rf plasma power of  $P=0.08 \text{ W/cm}^2$  and a low partial pressure of  $p(\text{SiH}_4)=0.03\text{-}0.07$  Torr. The substrates are oxide-covered c-Si wafers held at  $200^\circ\text{C}$ . The dotted, solid, and dashed lines identify the  $a \rightarrow a$ ,  $a \rightarrow (a+\mu c)$ , and  $(a+\mu c) \rightarrow \mu c$  transitions, respectively. The (up, down) arrows connected to data points indicate that the transition occurs (above, below) the identified thicknesses.

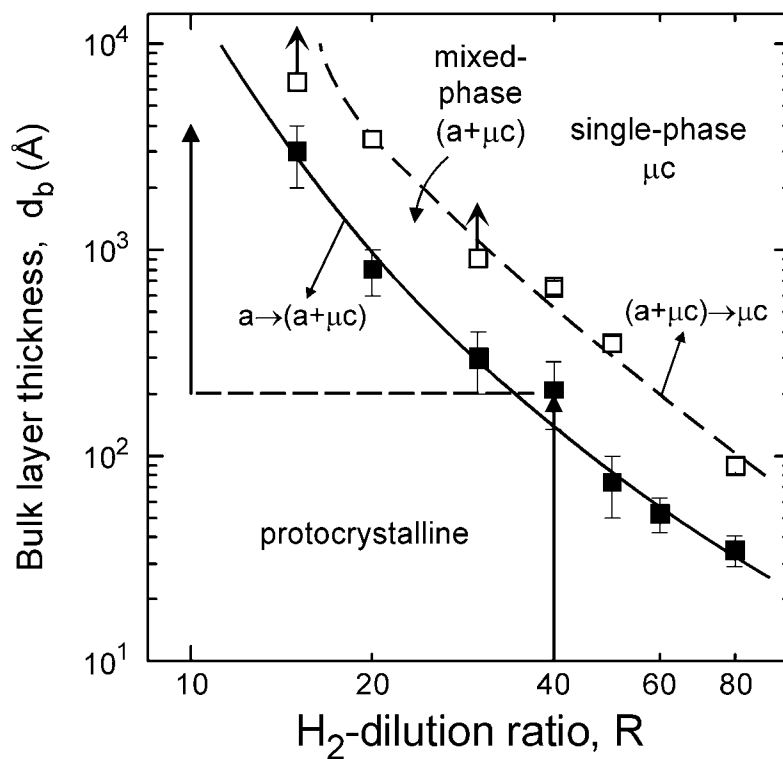


**Figure 16.** Extended phase diagram in the plane of  $R$  and  $d_b$  for Si:H depositions with  $R \geq 10$  at a low rf plasma power of  $P=0.08$  W/cm<sup>2</sup> and low partial pressure of  $p(\text{SiH}_4)=0.03$ - $0.07$  Torr. The substrates are  $R=0$  a-Si:H films held at 200°C. The solid and dashed lines identify the  $a \rightarrow (a+\mu c)$  and  $(a+\mu c) \rightarrow \mu c$  transitions, respectively. The up arrows connected to data points indicate that the transition occurs above the identified thickness values.

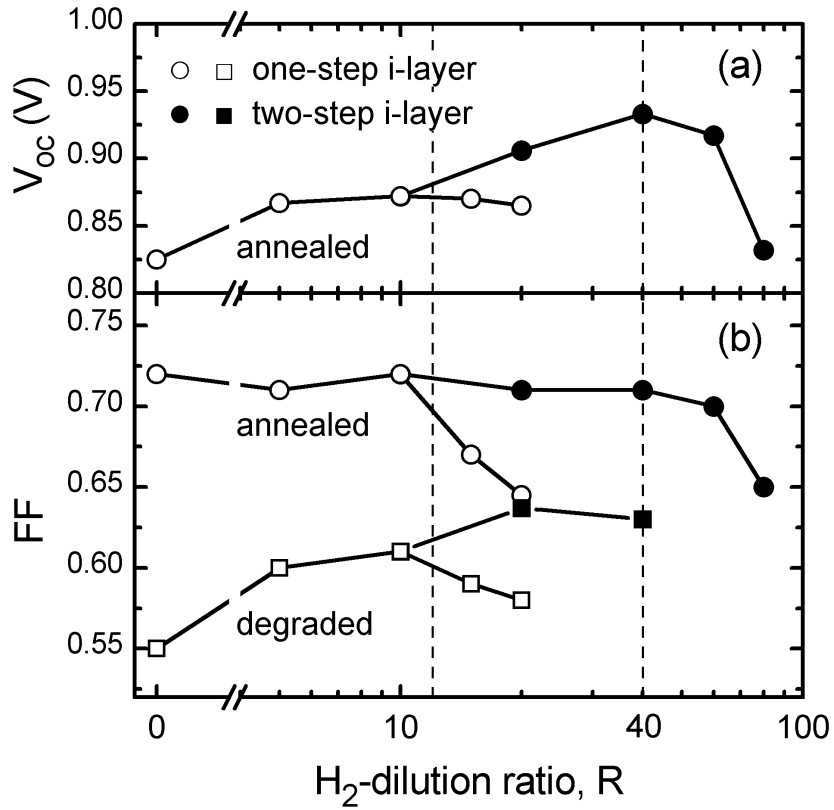


**Figure 17.** (a) Open circuit voltage  $V_{oc}$  and (b) fill-factor FF in annealed states (circles) and 100 hr AM1.5 degraded states (squares) for Si:H p-i-n solar cells incorporating one-step (4000 Å) i-layers versus the i-layer R (open symbols), and for cells incorporating two-step (100-200 Å)/(3900-3800 Å) interface/bulk i-layers versus the interface i-layer R (closed symbols). The vertical lines identify the  $a \rightarrow (a+\mu c)$  transitions for 4000 Å and 200 Å thick i-layers.

### Task 3.

#### Device Loss Mechanisms

To understand the device loss mechanisms in a-Si:H based solar cells it is important to be able to analyze all the cell characteristics in a manner which is self-consistent for different cell structures and relate them to the properties of their constituent materials. Key to this is the identification, separation and quantification of the recombination processes occurring in the bulk and interfaces; adequate characterization of the intrinsic material properties; and a better understanding of the defects responsible for SWE. In considering the operation of solar cells it is critical to address the important issues raised by the predictions of the defect thermodynamic model. The spatially non-uniform distribution of defects, such as have recently been inferred from drive level capacitance profiling<sup>29</sup> and dark current voltage characteristics<sup>30</sup>, not only have very serious consequences on the interpretation of results on solar cells but also on the ability to correlate them with those on the corresponding intrinsic thin films.

Detailed studies were carried out on the forward bias dark current ( $J_D - V$ ) characteristics of both p-i-n (superstrate) and n-i-p (substrate) p a-SiC:H solar cell structures with different a-Si:H buffer layers and  $R = 0$ ,  $R = 10$  intrinsic layers having thickness from 0.2 to 1.5  $\mu\text{m}$ . By controlling the recombination at the p/i interfaces through changing the band gap of the 200  $\text{\AA}$  a-Si:H i-layers adjacent to the a-SiC:H p-contact it was possible to clearly separate the contributions of the intrinsic layers from those of the p/i interfaces to the  $J_D - V$  characteristics. The  $J_D - V$  characteristics were measured using a four-probe technique that eliminates series resistance contributions thus allowing the diode currents to be accurately evaluated even at far forward bias. In addition, care was taken in these measurements not to introduce SWE defects into the cell structures with carrier injection at the higher forward biases.

Systematic changes in the  $J_D - V$  characteristics of the cell structures with  $R=0$  and  $R=10$  i-layers are obtained, just as in the 1 sun  $V_{oc}$ , when the band gap of the a-Si:H at the p/i interface is varied between 1.78 and 1.95 eV. This is illustrated in Fig. 18 with the results on p-i-n cell structures with a 4000  $\text{\AA}$   $R = 10$  i-layers in which the 200  $\text{\AA}$  at the p/i interface consist of  $R = 0$ ,  $R = 10$  and  $R = 40$  a-Si:H. Similar systematic changes in the  $J_D - V$  characteristics are also obtained with the cells having  $R = 0$  i-layers.

In  $J_D - V$  characteristics, such as in Fig. 18, it is possible to distinguish between the regimes corresponding to the recombination in the bulk and that at the p/i interfaces. It is also possible to identify the limitations imposed by the injection of carriers of high forward bias as well as transition from diffusive to drift current transport<sup>31</sup>. The kind of dependence of  $J_D$  on  $V$  associated with the recombination at the p/i interfaces can be seen in Fig. 18 from the results on the cell with the  $R = 0$  layer at the p/i interface whose large recombination dominates  $J_D$  over a wide voltage range. These currents, which are much higher than those with  $R = 10$  and  $R = 40$  a-Si:H at the p/i interfaces, also exhibit an effective diode quality factor  $m^*$  of 1.2. The effects of reducing this recombination results in the dramatically different  $J_D - V$  characteristics, as seen for the other two cell structures, where the bulk contributions can be identified. In the case of the  $R = 10$  p/i interface there is an extended region up to  $\sim 0.5$  V with an effective diode quality factor

<sup>29</sup> R. S. Crandall, J. Yang and S. Guha, *Mat. Res. Soc. Symp. Proc.*, **664**, A.19.2.1 (2001).

<sup>30</sup> M. A. Kroon and R. A. C. M. M. Van Swaaij, *J. Appl. Phys.*, **90**, 994 (1992).

<sup>31</sup> K. Lips, *Mat. Res. Soc. Symp. Proc.*, **37**, 455 (1995).

m of 1.4 that decreases to a value closer to  $m^*$  before being limited by carrier injection and the change from diffusive to drift transport. Further reduction of the recombination at the p/i interface by the  $R = 40$  layer extends the regime with  $m = 1.4$  to higher voltages. In addition it can be seen in Fig. 18 that there is superposition of the currents up to  $\sim 0.5$  V between the cell with  $R = 10$  and  $R = 40$  p/i interface layer, clearly indicating that these currents are due to carrier recombination in the bulk. Such bulk recombination and the voltage range over which it is present in the  $R = 40$  cell could be confirmed by the increase in  $J_D$  resulting from the introduction of light induced bulk defect as discussed later.

The  $J_D - V$  characteristics of the cells with  $R = 10$  and  $R = 0$  i-layers where the currents are determined by the bulk are consistent with the recombination through *spatially uniform densities of defects* having a continuous distribution of gap states.

The dark forward bias currents in p-i-n solar cells have been shown by Lips<sup>32</sup> to be determined by diffusion/recombination. The recombination can occur both in the bulk and at the p/i and n/i interfaces. Here only the former is considered since there is extensive evidence that the recombination at the p/i interfaces is more important than that at the n/i interfaces. Even though the recombination occurring at the p/i interfaces and in the bulk are both described by the Shockley-Reed-Hall (SRH) recombination mechanism, where the electrons and holes recombine through the defect states in the gap, their contributions to the diode quality factor of the dark current characteristics are distinctly different. In SRH the carrier recombination rate is determined by the product of the electron and hole concentrations,  $n$  and  $p$  respectively, which can be expressed as  $np/(Rn+p)\tau_{no}$ , where  $R$  is the ratio of the electron to hole capture cross section and  $\tau_{no}$  is the electron capture time by the recombination center that depends on the defect density. The concentration of the electrons and holes in the bulk change exponentially with potential drop across the i-layer,  $\phi$ <sup>33</sup>. In a-Si:H solar cells with low defect densities and absence of externally applied bias, the built-in potential  $V_{bi}$  distributes itself uniformly as  $\phi$  across the bulk of the i-layer with small potential drops  $\Delta V_n$  and  $\Delta V_p$  at the n and p contacts due to the space charge associated with the high carrier densities  $n_0$  and  $p_0$ , respectively. These potential drops constitute the barriers for the injection of electrons and holes from the n and p contacts into the bulk of the i-layer. This is illustrated in the schematic band diagram for the i-layer of p-i-n cells under forward bias shown in Fig. 19. Since  $V_{bi}-V=\phi+\Delta V_n+\Delta V_p$  and both  $\Delta V_n$  and  $\Delta V_p$  are essentially independent of bias,  $\phi$  decreases with voltage  $V$  as  $V_{bi}-V-\Delta V_n-\Delta V_p$ . For small values of  $\Delta V_n$ ,  $\Delta V_p$  relative to  $V_{bi}-V$ ,  $\phi=V_{bi}-V$ , which leads to the exponential dependence of  $J_D$  on  $V$ .

In the case of recombination at the p/i interface, the large density of holes adjacent to the p-contact remains constant with the applied forward bias. As a consequence the recombination current depends solely on the electron concentration there which increases exponentially with the potential drop across the whole i-layer. Thus, in the case of interface dominated currents, the effective diode quality factors such as  $m^*$  are close to one (values somewhat larger than one are due to some other current limiting factors which are not discussed here). It has been well established that for the dark currents dominated by bulk recombination, on the other hand, the diode quality factor is 2 if the recombination is through a *single* defect.

<sup>32</sup> K. Lips, Mat. Res. Soc. Symp. Proc. **377**, 455 (1995).

<sup>33</sup> J. Deng, J. M. Pearce, R. J. Koval, V. Vlahos, R.W. Collins, and C. R. Wronski, Appl. Phys. Lett. May 2003 (in press).

However, in the  $J_D - V$  characteristics of Fig. 18 dominated by bulk recombination the effective diode quality factor  $m$  is 1.4, a value which lies between 1 and 2. This can be explained with just the presence of a continuous distribution of gap states in the a-Si:H  $i$  layer without the necessity of having a spatially varying density of defects in the  $i$ -layer. It was shown both numerically by Hack and Shur<sup>34</sup> and analytically by Berkel et al.<sup>35</sup> that a spatially uniform distribution of defects which has an exponential energy distribution of states around mid-gap results in diode quality factors over an extended range of forward bias which have constant values between 1 and 2. In SRH type recombination, the localized states that act as recombination centers are those located between the electron and hole quasi-Fermi levels, the separation of which is equal to the applied voltage. As the applied voltage and the splitting of the quasi-Fermi levels are increased there is a corresponding continuous increase in the number of gap states acting as recombination centers. In the case of an exponential distribution of states around mid-gap the increase in the number of recombination centers enhances the current by an exponential term which changes the diode quality factor from 2 to a lower value with an offset which depends on the exponential form in the energy distribution of the gap states.

In the case of a distribution which is significantly different from an exponential form,  $d(\log J_D)/dV$  is no longer constant so that the diode quality factor will no longer have the same value over an extended voltage range. However, in the results obtained for both  $R = 10$  and  $R = 0$  cells where the recombination is dominated by that in the  $i$ -layers  $d(\log J_D)/dV$  is approximately constant over extended regions of voltage. This indicates that the distributions of the gap states around mid-gap are similar, although not identical, to that of an exponential form such as for instance the Gaussian distributions suggested by the studies on the corresponding thin film  $i$  layers<sup>36</sup>.

At high current densities and forward bias, there are clear deviations from the exponential dependence on  $V$  in the dark current. This occurs when  $V_{bi} - V = \Delta V_n + \Delta V_p$  which corresponds to  $\phi = 0$ . Subsequent increases in  $V$  invert the field across the  $i$ -layer thus introducing the field driven drift currents<sup>37</sup>. In addition, at high values of  $J_D$  the potential barriers associated with  $\Delta V_n$  and  $\Delta V_p$  begin to limit the carrier injection from the contacts into the  $i$ -layer. The height of these barriers depends on  $n_0$ ,  $p_0$  and the defect density in the  $i$ -layer which is small in high quality cells. As a consequence, the effect is not significant until very high current levels. However, in low quality cells, where these barriers are high due to a large density of defects, their effects become significant at lower current levels.

A major convenience brought by the defect pool model in explaining a non-integer value of the diode quality factor  $m$ , and the reported absences of the dependence of  $J_D - V$  characteristics on the thickness of the  $i$ -layer, is that it allows the maximum recombination to occur at a fixed position near the  $p/i$  interface because of the very large density of defect there. However, a clear dependence of the dark currents on the thickness of the  $i$ -layers is obtained in the cells studied here which is inconsistent with the presence of such large densities of defects near the  $p/i$  interface.

The “elusive” dependence of  $J_D - V$  characteristics on thickness was obtained in cell structures with both  $R = 0$  and  $R = 10$   $i$ -layers. Such a thickness dependence is

<sup>34</sup> M. Hack and M. Shur, *J. Appl. Phys.* **54**, 5858 (1983).

<sup>35</sup> C. van Berkel, M. J. Powell, A. R. Franklin, and I. D. French, *J. Appl. Phys.* **73**, 5264 (1993).

<sup>36</sup> L. Jiao, Charged Defect States in Hydrogenated Amorphous Silicon Materials for Solar Cells, PhD Thesis, The Pennsylvania State University, (1998).

<sup>37</sup> K. Lips, *Mat. Res. Soc. Symp. Proc.* **377**, 455 (1995).

illustrated in Fig. 20 where the results are shown for p-i-n cell structures, with R = 0 i layers 0.4, 0.8 and 1.5  $\mu\text{m}$  thick, in which the recombination has been minimized by having R = 40 a-Si:H at the p/i interface. A systematic increase in the bulk recombination currents can be clearly seen as the i-layer thickness is increased. Also shown in the inset is the decrease in the corresponding far forward bias currents which also exhibit a dependence on thickness expected when the transport ceases to be diffusion/recombination and becomes drift dominated.

The above results clearly indicate the absence of very large densities of defects and correspondingly very large electric fields at the p/i, n/i interface regions. Further evidence for the absence of the spatial distributions of defects in the intrinsic layers of a-Si:H solar cells predicted by thermodynamic equilibration was obtained from the equivalence of the  $J_D - V$  characteristics in p-i-n and n-i-p solar cells. These are found with both R = 0 and R = 10 i layer cells having different p/i interfaces and is illustrated in Fig. 21 with the results on the cells having a 4000 Å thick R = 10 i-layer and R = 10 and R = 40 at the p/i interface.

In view of the above results which clearly establish *homogeneous distributions of defects* in the i layers of the p-i-n and n-i-p a-Si:H solar cells, the properties that are clearly identified and confirmed as those of the bulk can be directly correlated with those of the corresponding i-layer films.

The transport of the carriers in the case of photocurrents is distinctly different from those injected from the contacts since they are created throughout the bulk of the i-layer. They are subject to a drift field E and are swept out towards the contacts as a net drift current<sup>38</sup>. In i-layers with low defect densities, the space charge has only a small effect on the electric field distribution so that  $E = \phi/L$  where  $\phi$  is the potential drop across the i-layer and L its thickness. The photo-current  $J_L$  is determined by the densities of electrons and holes that reach the contacts before recombining, where the probability of undergoing recombination depends on their effective lifetime,  $\tau$ , and transit time  $T_{tr}$ . This current  $J_L$  can be written as  $J_L = J_G - J_{RG}$  where  $J_G$  is the photocurrent created by the generation rate of carriers, G, due to the absorbed photons in the bulk.  $J_{RG}$  is the recombination current in the bulk which is determined by  $T_{tr}$  and  $\tau$ .  $J_G$  depends only on the intensity of the illumination and is independent on the electric field E(V) while  $J_{RG}$  depends on E since  $T_{tr} \propto 1/E$ . Under short circuit conditions the effective transit time  $T_{tr} \propto 1/V_{bi}$ . In high quality a-Si:H cells  $J_{RG}$  is significantly lower than  $J_G$  where this is indicated by quantum efficiencies under short circuit conditions of virtually 100% for carriers generated in the bulk. For  $J_{RG} \ll J_G$ ,  $J_{sc} = J_G$  which makes  $J_{sc}$  directly proportional to the illumination intensity as is observed in high quality cells.

Under a forward bias V across the i-layer, as  $T_{tr}$  increases, so does  $J_{RG}$ . At the same time the balance between the drift and diffusive currents from the high densities of  $n_0$ ,  $p_0$  carriers is disturbed so that diffusion currents,  $J_{diff}$ , are introduced in the opposite direction to the photo-generated currents, as shown in Fig. 22.  $J_L$  then becomes:

$$J_L(V) = J_G - J_{RG}(V) - J_{diff}(V) \quad (1)$$

Since the mechanism governing this  $J_{diff}$  is exactly the same as that of the diffusion current  $J_D$  in the dark, as discussed earlier, they increase exponentially with V. If the diffusive transport under illumination is the same as that in the dark  $J_{diff}(V) = J_D(V)$ . As

<sup>38</sup> D. E. Carlson and C. R. Wronski, "Topics in Applied Physics", Vol. 36, M. H. Brodsky ed., Springer-Verlag, New York, 1979.

both  $J_{RG}$  and  $J_{diff}$  increase with  $V$ ,  $J_L$  decreases until it becomes zero at  $V=V_{oc}$ . Under open circuit conditions the relation becomes

$$J_{sc} = J_G = J_{RG}(V_{oc}) + J_{diff}(V_{oc}) \quad (2)$$

and if  $J_{diff} \gg J_{RG}$ ,

$$J_{sc} = J_{diff}(V=V_{oc}) = J_D(V=V_{oc}) \quad (3)$$

so that superposition is present between  $J_{sc}$  versus  $V_{oc}$  and  $J_D$  versus  $V$ . This occurs even though the superposition principle is not valid in a-Si:H solar cells for *all* values of  $V$  due to the voltage dependent contributions of  $J_{RG}$  to  $J_L$ .

Superposition between  $J_{sc}-V_{oc}$  and  $J_D-V$ , however, will not also be present if at  $V=V_{oc}$ ,  $J_{RG}$  is comparable to or larger than  $J_{diff}$ . This can occur at high illumination levels when  $V_{oc}$  approaches  $V_{bi}$  so that the small values of  $E$  present in the bulk result in  $T_{tr} > \tau$  which leads to large values of  $J_{RG}$ . At the same time the high forward bias currents in the  $J_D-V$  characteristics encounter limitations on carrier injection imposed by the potential barriers  $\Delta V_n$  and  $\Delta V_p$ . Both of these effects contribute to a split between the two characteristics since the limitations of  $J_{RG}$  on  $V_{oc}$  move the  $J_{sc}-V_{oc}$  to lower values of  $V_{oc}$ , and the limitations on carrier injection on the other hand move  $J_D-V$  to higher values of  $V$ . Increase in the density of defects in the i-layer, with the corresponding increases in  $J_{RG}$  and  $\Delta V_n$ ,  $\Delta V_p$  at the n and p contacts, introduce a split between the  $J_{sc}-V_{oc}$  and  $J_D-V$  characteristics at lower voltages. At sufficiently large defect densities this can thus limit such superposition to very low values of  $V_{oc}$  and  $V$ .

The validity of the mechanisms just described has been established with results on the superposition of  $J_{sc}-V_{oc}$  and  $J_D-V$  characteristics obtained on high quality a-Si:H cells which illustrate. Shown in Fig. 23 are the results for two p-i-n solar cells, one with  $R=0$  intrinsic layer and the other with  $R=10$  intrinsic bulk layer, which exhibit excellent superposition between  $J_{sc}-V_{oc}$  and  $J_D-V$  characteristics. These characteristics, which are from the cells in the annealed state, have regions of superposition from 0.2 V to 0.7 V and 0.2 to 0.8 V, respectively. Because the  $R=0$  i-layer has a smaller band gap (1.78 eV) than that of  $R=10$  (1.86 eV), the intrinsic carrier concentrations in the  $R=0$  cell are about a factor of ten higher. Since the defect densities in the two i-layers are very similar the dark forward bias currents are thus about ten times higher for the cell with  $R=0$  i-layer. It can also be seen in Fig. 23 that the split between  $J_{sc}-V_{oc}$  and  $J_D-V$  in the cell with  $R=0$  i-layer occurs at a smaller voltage than that for the cell with  $R=10$  i-layer. However these splits occur at essentially the same current level ( $\sim 10^{-4}$  A/cm<sup>2</sup>) for both cells. This is an indication that the split between the  $J_{sc}-V_{oc}$  and  $J_D-V$  characteristics is due to the dark currents becoming limited by the barriers adjacent to the n and p contacts. This effect is also reflected in the  $J_{sc}-V_{oc}$  characteristic remaining in an exponential form while the  $J_D-V$  characteristics do not. It can be pointed out that such limitation on carrier injection can be identified and reliably characterized only by using the four-probe technique so that the effects of series resistance on  $J_D-V$  are eliminated.

The potential barriers that limit the carrier injection are determined by the space charge which is directly related to the densities of defects in the i-layer. Any increase in density of these defects leads to larger  $\Delta V_n$  and  $\Delta V_p$  which reduces the carrier injection. In order to confirm that the split in  $J_{sc}-V_{oc}$  and  $J_D-V$  in Fig. 23 is due to such field distortions the densities of gap states in the i-layer of the  $R=10$  of Fig. 23 were increased

with light induced degradation. The results for the  $J_{sc}$ - $V_{oc}$  and  $J_D$ - $V$  characteristics obtained for the annealed state and that after nine hours of degradation with 1 sun intensity of red light are shown in Fig. 24 over the voltage range of interest. It can be seen in Fig. 24 that after introducing the light induced defects, as expected, there is an increase in the bulk recombination currents in the dark and the separation between  $J_{sc}$ - $V_{oc}$  and  $J_D$ - $V$  characteristics move to a lower voltage, from 0.8 to 0.6 V, and lower  $J_{sc}$  from  $10^{-4}$  to  $10^{-6}$  A/cm<sup>2</sup>. These higher densities of defects not only increase the field distortions and potential barriers at the n and p but also reduce the carrier lifetimes. Consequently the changes observed in Fig. 24 include both the effects with the increase in  $J_{RG}$  in these cells to be smaller.

The effect of the higher density of defects on the split can be more clearly observed in Fig. 25, where the results are shown for the annealed state and the degraded state of the p-i-n cell with  $R = 10$  intrinsic layer and a  $R = 0$  p/i interface layer. Since the presence of the undiluted  $R = 0$  interface layer greatly enhances the recombination current at the p/i interface, due to the smaller energy gap of the undiluted material as discussed earlier, the limitation imposed on the dark current by the barrier at this interface becomes more pronounced. This is reflected in the Fig. 25 where the  $J_{sc} - V_{oc}$  characteristics at the high voltages remains essentially the same after degradation but the dark currents bend down dramatically, thus making the split between  $J_{sc} - V_{oc}$  and  $J_D - V$  much more pronounced than in Fig. 23.

In order to verify the self-consistency of the mechanisms presented for the superposition of  $J_{sc}$ - $V_{oc}$  and  $J_D$ - $V$  characteristics in the a-Si:H p-i-n solar cells numerical simulations were carried on these characteristics. The parameters used in the simulation were those by Jiao<sup>39</sup> except that the distribution near mid gap now consisted of both donor,  $N_D$ , and acceptor  $N_A$ , states. The electron capture cross-sections used are  $10^{-16}$  cm<sup>2</sup> and  $10^{-14}$  cm<sup>2</sup> for the  $N_A$  and  $N_D$  states respectively while their hole capture cross-sections are  $10^{-14}$  cm<sup>2</sup> and  $10^{-16}$  cm<sup>2</sup>. The results obtained with  $N_D$ ,  $N_A$  of  $5 \times 10^{15}$  cm<sup>-3</sup> and an intrinsic band gap of 1.86 eV, corresponding to the  $R=10$  cell, are shown in Fig. 26. It can be clearly seen in the figure that, consistent with the experimental results, there is excellent superposition between  $J_{sc}$ - $V_{oc}$  and  $J_D$ - $V$  over the voltage and current regime such as in Fig. 23. Simulations were also carried out in which only the densities of the donor and acceptor states near mid-gap were changed. As the defect density of these states is increased, corresponding to a degradation of the cell, the split between  $J_{sc}$ - $V_{oc}$  and  $J_D$ - $V$  moves systematically to smaller and smaller voltages until there is no superposition between the characteristics even at the lowest voltages. This is found to occur when the defect density exceeds  $2 \times 10^{17}$  cm<sup>-3</sup>, a forty-fold increase, which is shown in Fig. 27. To verify the key role played by the limitations imposed by the space-charge-induced barriers at the contacts in determining the absence of superposition, the space charge effects present in this case were reduced by decreasing the defect density from  $2 \times 10^{17}$  cm<sup>-3</sup> back to  $5 \times 10^{15}$  cm<sup>-3</sup>, the level used for Fig. 26. However at the same time, by increasing the  $N_D$ ,  $N_A$  capture cross-sections by a factor of forty the carrier lifetimes were reduced by the same factor. The corresponding results are shown in Fig. 28 where it can be seen that now there is a regime of superposition between the  $J_{sc}$ - $V_{oc}$  and  $J_D$ - $V$  where the subsequent separation between them is much smaller than in Fig. 27. This illustrates the importance of the space-charge-induced barriers at the n, p contacts on the

<sup>39</sup> L. Jiao, "Charged Defect States in Hydrogenated Amorphous Silicon Materials for Solar Cells", PhD Thesis, The Pennsylvania State University, 1998.

superposition and their effects relative to those of the photo-generated carrier lifetime contributing to  $J_{RG}$ .

## 1 Sun Open Circuit Voltage Characteristics

The effect of the p/i interfaces on the magnitude and stability of 1 sun open circuit voltage ( $V_{oc}$ ) in the cell structures discussed above were also identified. Systematic increases in  $V_{oc}$  are obtained with the reduction in the contributions of the p/i interface recombination observed in the  $J_D$ - $V$  and  $J_{sc}$ - $V_{oc}$  characteristics. In both the p-i-n and n-i-p solar cells the 1 sun  $V_{oc}$  increased from 0.85 to 0.89 and 0.92 for a-Si:H buffer layer of  $R=0$ ,  $R=10$ , and  $R=40$  respectively. As illustrated in Fig. 29, all of these 1 sun  $V_{oc}$ s are stable, decreasing in magnitude by less than 10mV over 100 hours of 1 sun illumination, a time in which the bulk recombination reaches a degraded steady state. The results clearly indicate that these 1 sun  $V_{oc}$ s are limited by the recombination at the p/i interfaces and that they are not affected by increased recombination in the bulk due to the Staebler-Wronski Effect (SWE), as discussed above. Because the recombination at the p/i interface depends on a variety of unknown parameters related to the p contact and the transport of carriers across the interface, it is difficult to clearly identify mechanisms determining its nature. However, it is noteworthy that the decreases in recombination expected for wider bandgap of a-Si:H at the p/i interface caused by higher hydrogen dilution ratios results in the systematic increases in  $V_{oc}$ .

Evidence was found that lower recombination at the p/i interfaces is present in the case of protocrystalline p-Si:H contacts than that obtained with the a-SiC:H p-contacts and the  $R=40$  buffer layer. As discussed in Task 1, this is reflected not only in higher  $V_{oc}$  values of 0.95 to 0.96 but also in the kinetics of their light induced changes also shown in Fig. 29. It can be seen in Fig. 29 that after the apparent initial absence of any change in  $V_{oc}$  there is an onset of degradation which reaches a degraded steady state (DSS) in the same time frame as the light induced changes in the bulk i-layer. In the initial regime, the  $V_{oc}$  is limited by the recombination either at the p/i interface or in the tail states. The decrease and the time taken to reach DSS can be attributed to the increase in the recombination due to the light induced defects in the bulk, which becomes sufficient to limit the  $V_{oc}$ .

## Correlations between Solar Cell and Thin Film a-Si:H Properties

There have been very few studies to date in which the results on thin films have been *directly* correlated with those on cells having identically-prepared i-layer materials. This is particularly true for results in which both films and cells are degraded under 1 sun illumination so that both the kinetics and the degraded steady states (DSS) under solar cell operating conditions can be directly correlated. Previous attempts to connect the light induced changes in a-Si:H to the degradation in solar cells have focused on the creation of dangling bonds,  $D^0$ , near midgap in relation to the changes in efficiencies (fill factors) of cells. This has been and is being done in spite of the reported lack of such correlations by von Roedern<sup>40</sup> and Yang et al.<sup>41</sup> Attempts by Wyrsh et al.<sup>42</sup> at correlating the light induced changes in *effective* mobility-lifetime products, representing the transport of both

<sup>40</sup> B. von Roedern, *Appl. Phys. Lett.* **62**, 1368 (1993)

<sup>41</sup> J. Yang, X. Xu, and S. Guha, *Mat. Res. Soc. Symp. Proc.* **336**, 687 (1994).

<sup>42</sup> N. Wyrsh, N. Beck, C. Hof, M. Goerlitzer, and A. Shah, *J. Non-Cryst. Solids* **198-200**, 238 (1996).

holes and electrons in films with the changes in cells, had somewhat better success but still left many unanswered questions. The correlations between the properties of a-Si:H thin films and those of corresponding solar cells is however complicated by the presence of the different defect states and their continuous distribution of gap states. Despite the extensive studies for over 25 years these defects have not been adequately characterized in both films and solar cells.

Direct correlations are being established between the light induced changes under 1 sun illumination in the properties of a-Si:H and those in the characteristics of p-i-n cells incorporating identically-prepared i-layers. These correlations are obtained after account is taken of the effect that the location of the electron and hole quasi-Fermi levels has on the carrier recombination that occurs through the different gap states. The changes in midgap state densities are being studied on the films with subgap absorption and are directly correlated with changes in the dark I-V characteristics under forward bias. In this case small quasi-Fermi level splitting is present so the recombination of the injected carriers is determined by the midgap states in the bulk of the i-layer. The changes in the electron mobility–lifetime products measured on the films are correlated with changes in the fill factor measured on cells. This is being carried out under the same conditions with large quasi-Fermi level splitting present and recombination occurring through states spanning a wide region of the gap, such as that occurs under 1 sun illumination. In addition, the question as to whether the rates at which defects are created under 1 sun illumination are the *same* in thin films as in the identically-prepared i-layers of the corresponding solar cells is being addressed. This is accomplished by studying the kinetics of the characteristics of films and cells during illumination to a degraded steady state (DSS).

Correlations have been obtained between the kinetics of light induced changes in electron  $\mu\tau$  products with those fill factors for different intrinsic layers and for different temperatures of degradation. This indicates that the light induced changes in the FF under 1 sun illumination, controlled by carrier recombination in the i-layer, can be correlated with the changes in the corresponding film. However, in order to do this, it is necessary to ensure that both are characterized with comparable quasi-Fermi level splitting. Since the FF's are determined by both electron and hole transport, it is somewhat surprising that direct correlations are found between the FF's and the electron  $\mu\tau$  products, the latter obtained with  $G=10^{19}$ - $10^{20}$   $\text{cm}^{-3}\text{s}^{-1}$  which corresponds to 1 sun illumination. Indeed, such correlations are found not only for cells having different thicknesses, in which case the FF's are directly related to the i-layer, but also for degradations carried out at different temperatures between 25°C and 100°C. This is illustrated by plotting  $1/\mu\tau$  versus FF as in Figs. 30 and 31. The quantity  $1/\mu\tau$  is proportional to the defects that act as recombination centers.

No comparable correlations are found when comparing the kinetics of FF with those of subgap absorption magnitude and in particular the commonly used  $\alpha(1.2)$ . Direct correlations, however, are being established between the light induced changes in the cell  $J_D$ -V characteristics and those in the corresponding thin film materials whose  $\mu\tau$  products and  $\alpha(E)$  are being characterized in detail. As discussed earlier the  $J_D$ -V characteristics can be directly related to carrier recombination in the bulk i-layers and their light induced changes not only reflect the evolution of the defect states but also offer an additional “probe” for characterizing them in a self-consistent manner with results on the films. The kinetics of the light induced changes in  $J_D$ -V characteristics are illustrated in Fig. 32 where the  $J_D$ -V characteristics for a p-i-n cell with R=10 i-layer at its annealed

state and after 1 sun degradation are shown. The monotonic increases in the current reach the DSS in the same time frame as the light induced changes in thin films and also exhibit complete reversibility upon annealing. The evolution of the currents and their dependence of bias (quasi-Fermi level splitting) is being carefully analyzed to obtain direct information about the densities and energy distribution of the light induced gap states. In parallel, as discussed in the next section, detailed analysis is being carried out on the evolution of the corresponding changes in  $\alpha(E)$  studied on the thin film intrinsic layers.

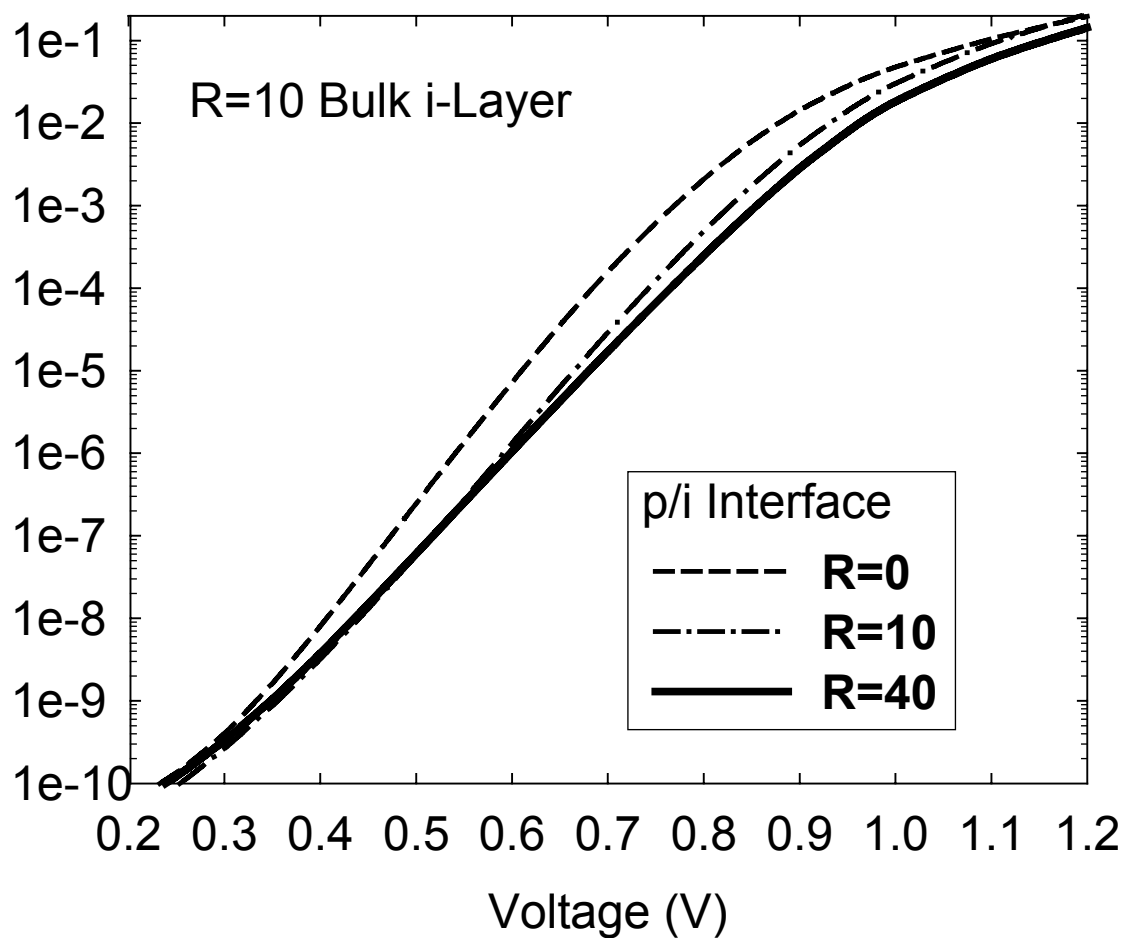


**Figure 18.**  $J_D - V$  characteristics for p-i-n cell structures with 4000 Å  $R = 10$  a-Si:H i layers and  $R = 0, 10$  and  $40$  a-Si:H at the p/i interfaces.

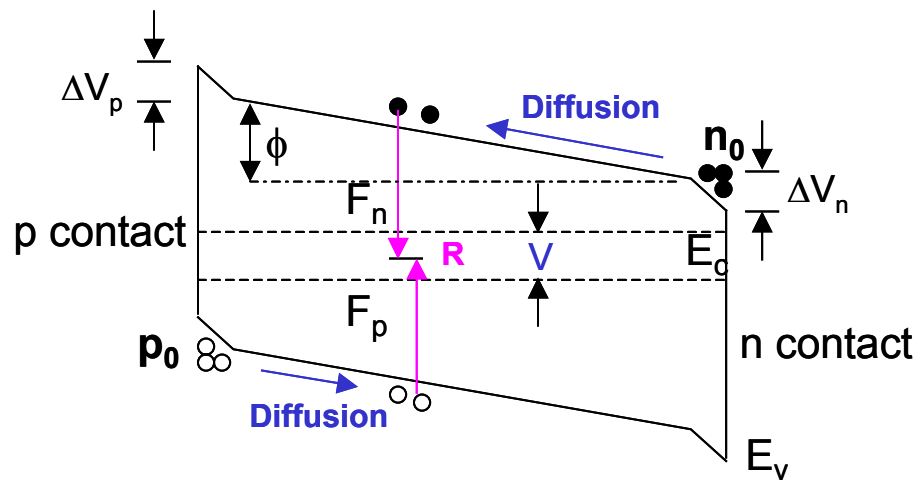


**Figure 19.** Schematic band diagram for i-layer of p-i-n cells under forward bias in the dark.

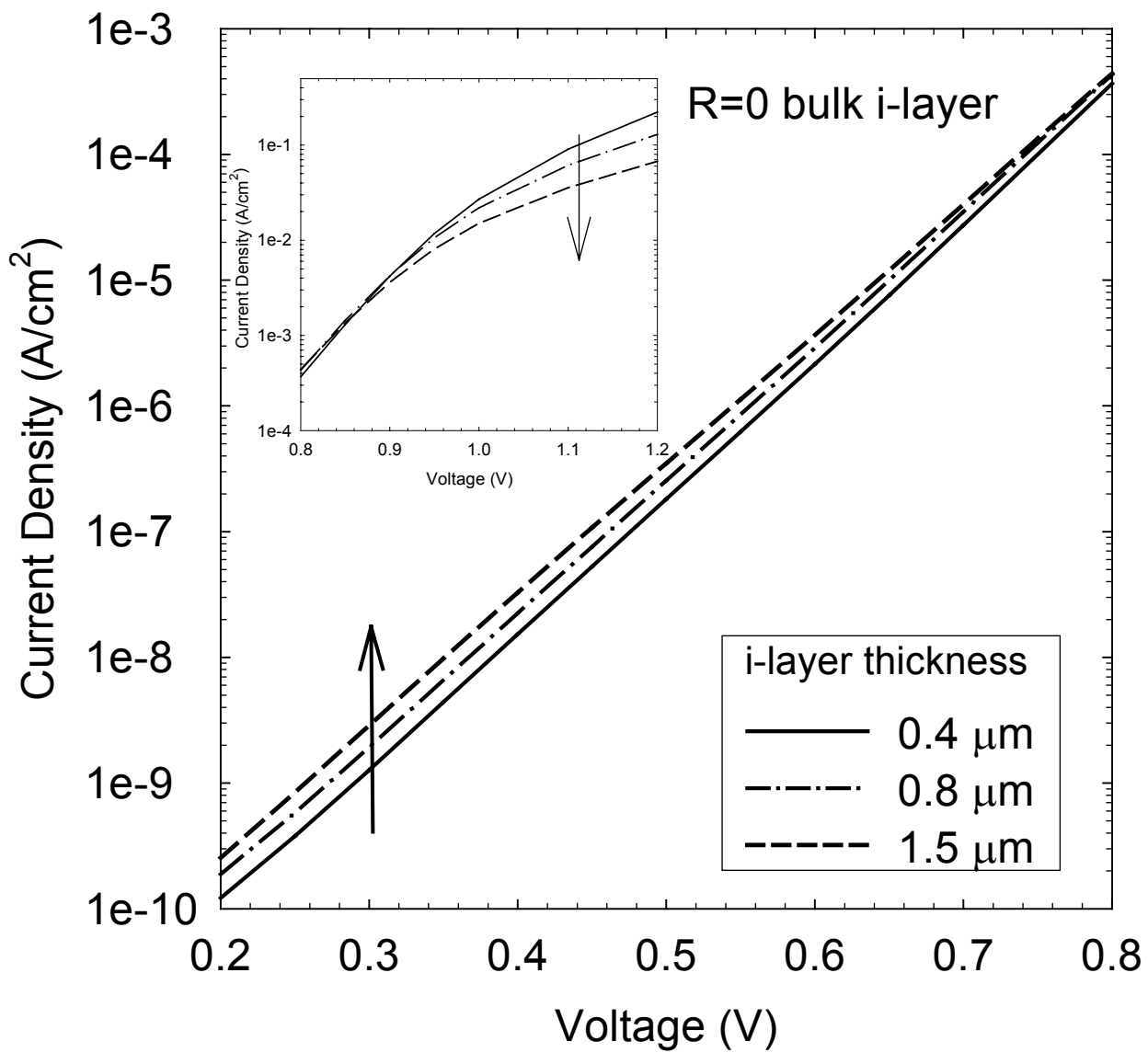


**Figure 20.**  $J_D - V$  characteristics of p-i-n cell structures with 0.4, 0.8 and 1.5  $\mu m$  thick a-Si:H i layers and  $R = 40$  a-Si:H at the p/i interfaces.

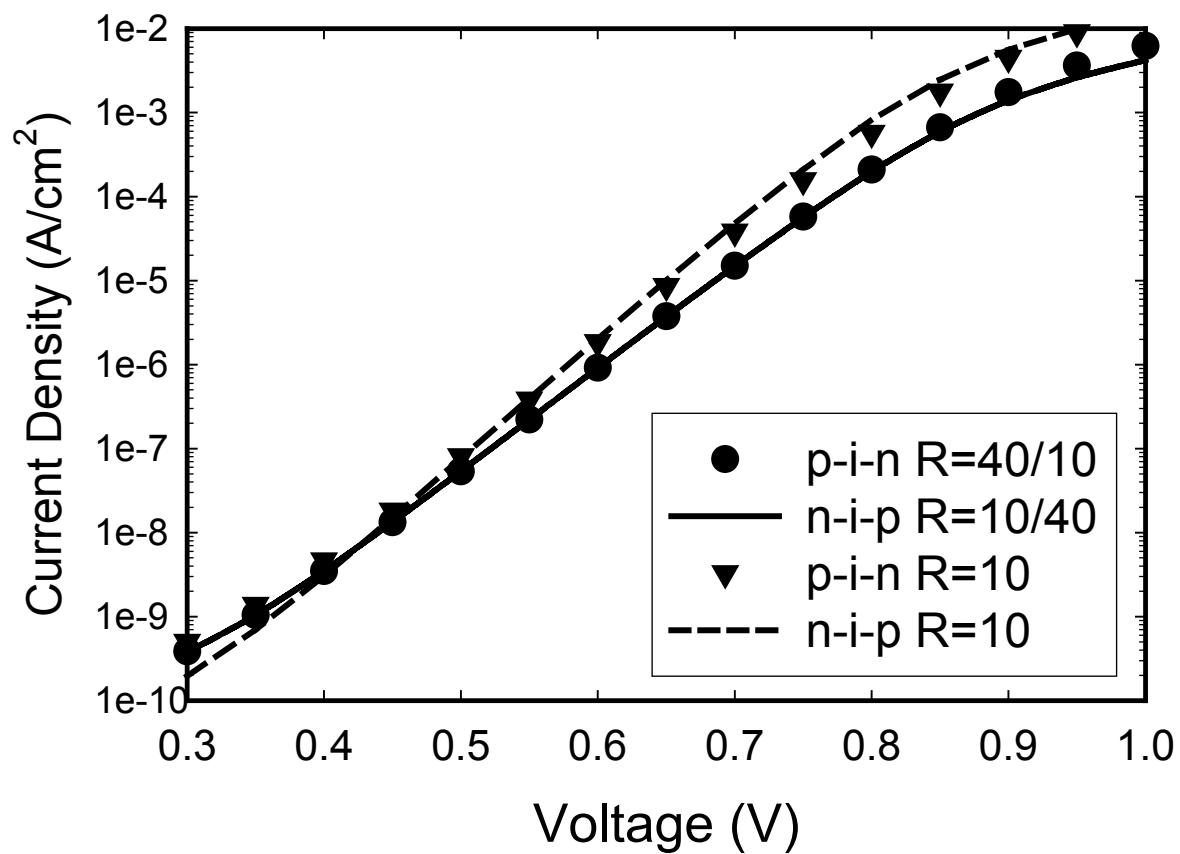


**Figure 21.**  $J_D - V$  characteristics of p-i-n and n-i-p cell structures with  $0.4 \mu\text{m}$   $R = 10$  i-layers and  $R = 10, 40$  a-Si:H at the p/i interfaces.

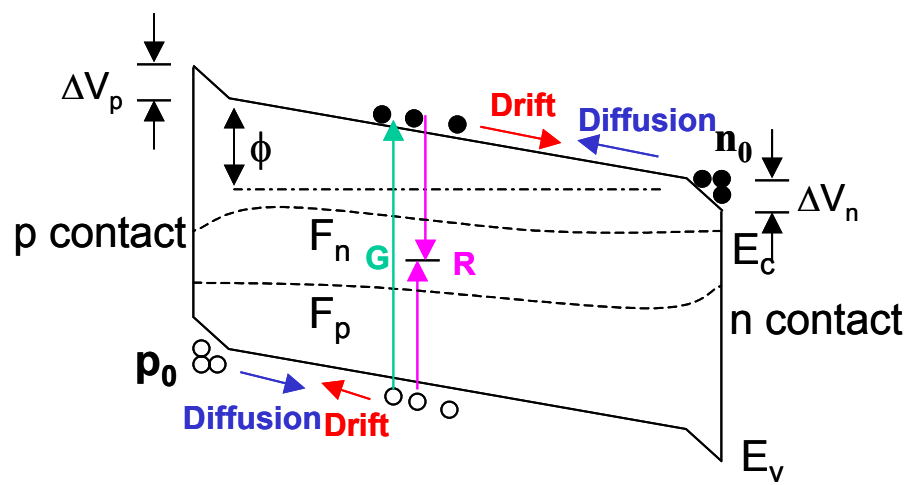


**Figure 22.** Schematic band diagram for i-layer of p-i-n cells under forward bias and illumination.

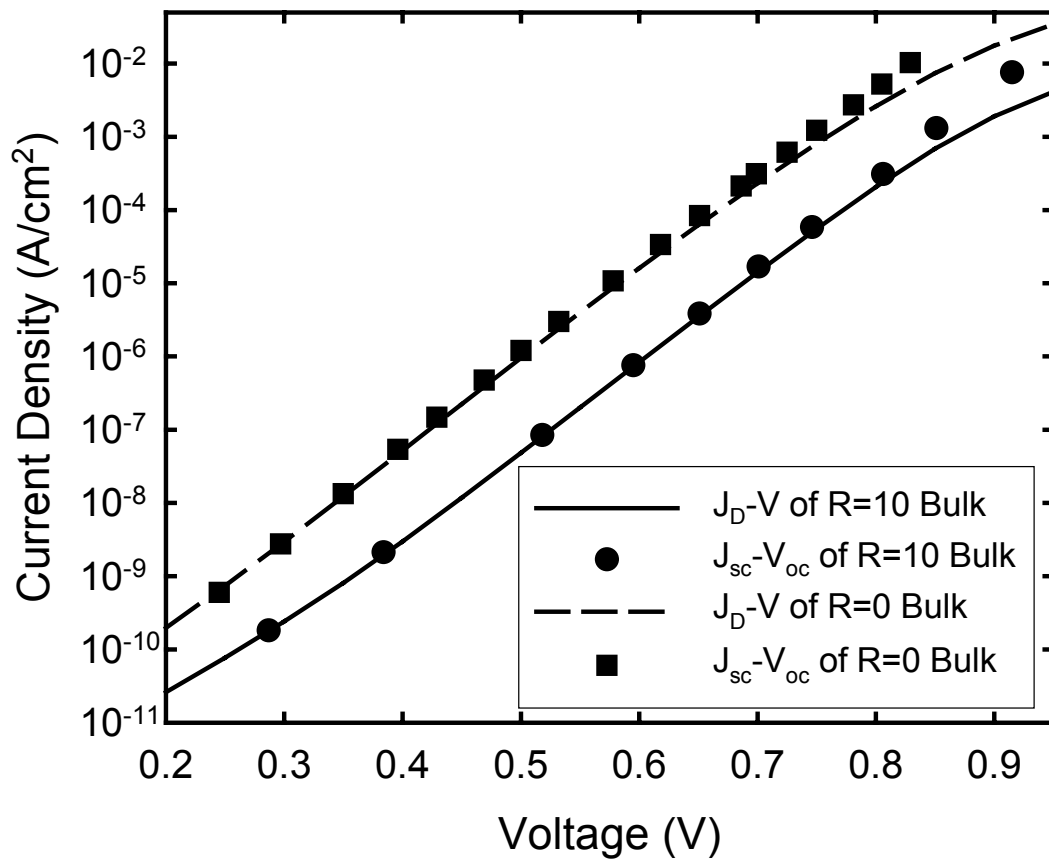


**Figure 23.**  $J_{sc}$ - $V_{oc}$  and  $J_D$ - $V$  characteristics of p-i-n cells with 4000 Å R=0, R=10 i-layers.

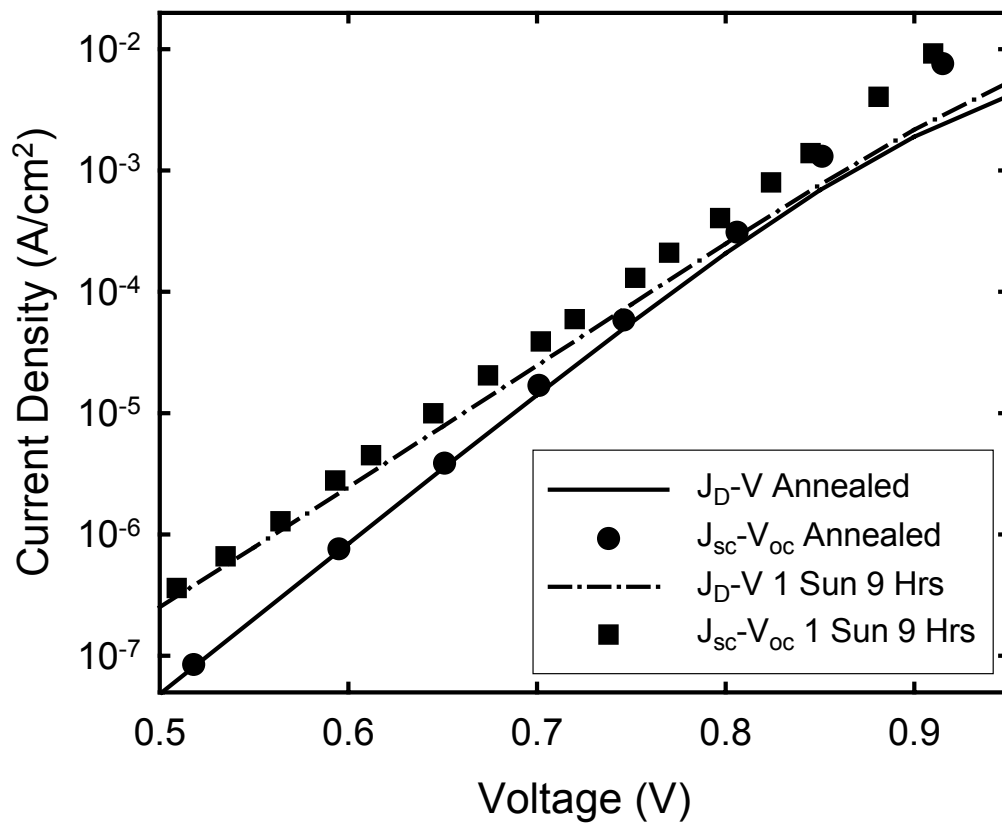


**Figure 24.**  $J_{sc}$ - $V_{oc}$  and  $J_D$ - $V$  characteristics of the p-i-n cell with R =10 i-layer of Fig. 23 before and after 1 sun red light degradation.

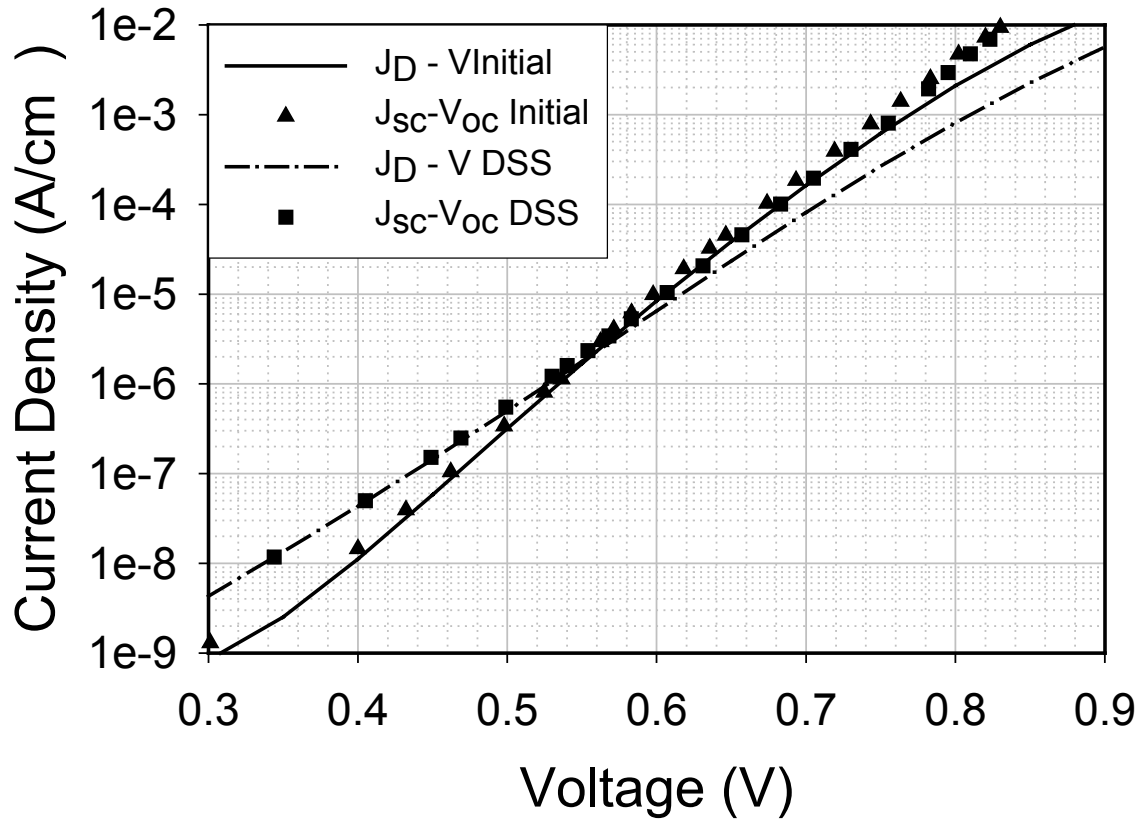


**Figure 25.**  $J_{\text{sc}} - V_{\text{oc}}$  and  $J_D - V$  characteristics of a p-i-n cell with  $R = 10$ ,  $4000 \text{ \AA}$  i- layer and  $R = 0$  p/i interface before and after degradation with 1 sun of red light.

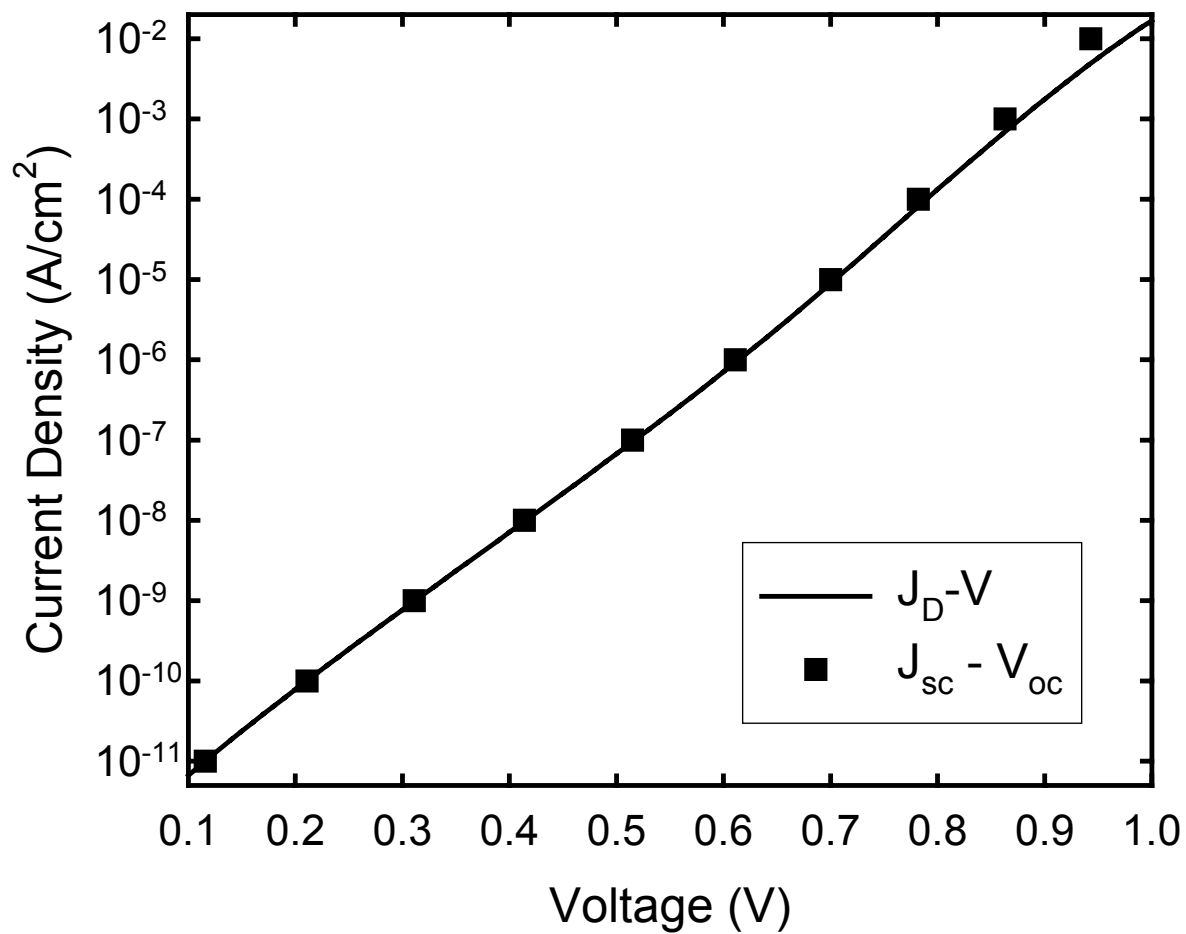


**Figure 26.** Simulated  $J_{sc}-V_{oc}$  and  $J_D-V$  characteristics of a p-i-n cell with a 4000 Å i-layer that has a band gap of 1.86 eV.

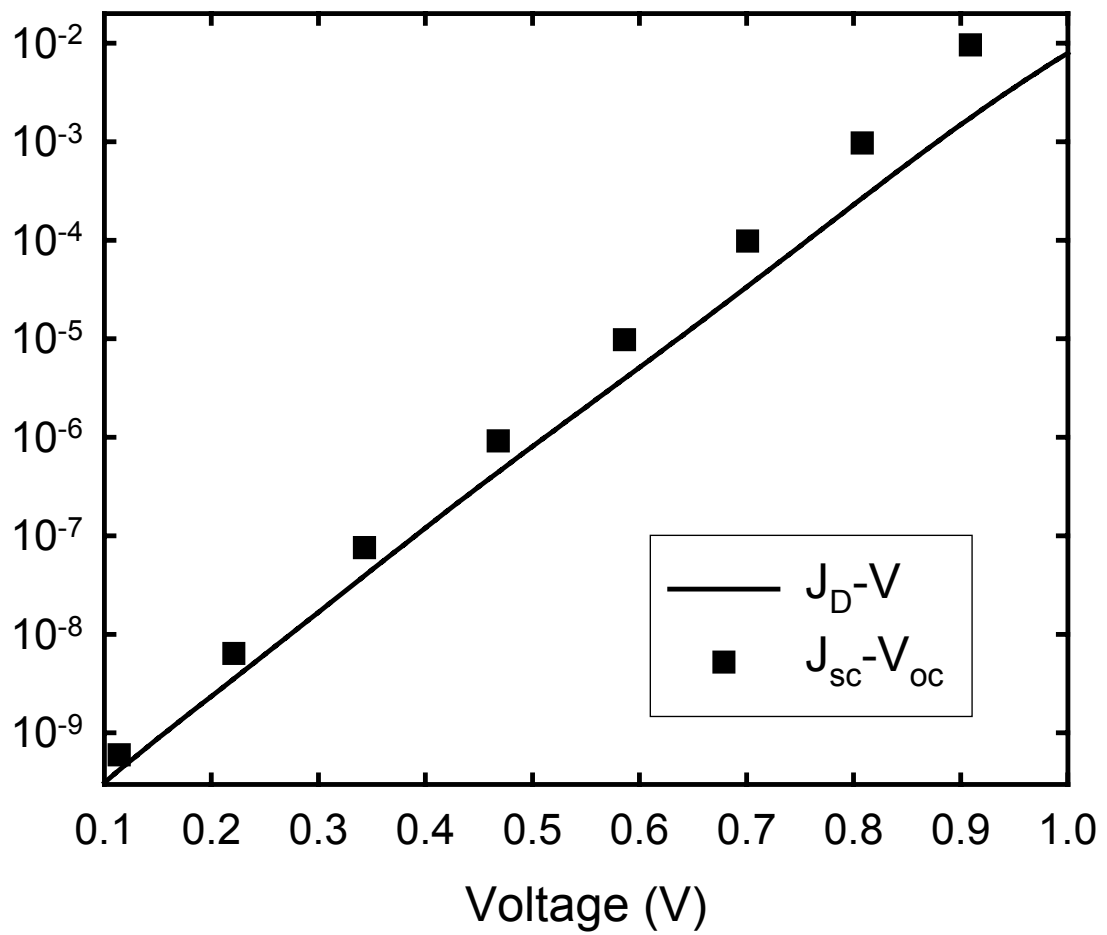


**Figure 27.** Simulated  $J_{sc}-V_{oc}$  and  $J_D-V$  characteristics of the p-i-n cell in Fig. 26 but with  $N_D$ ,  $N_A$  densities 40 times higher.

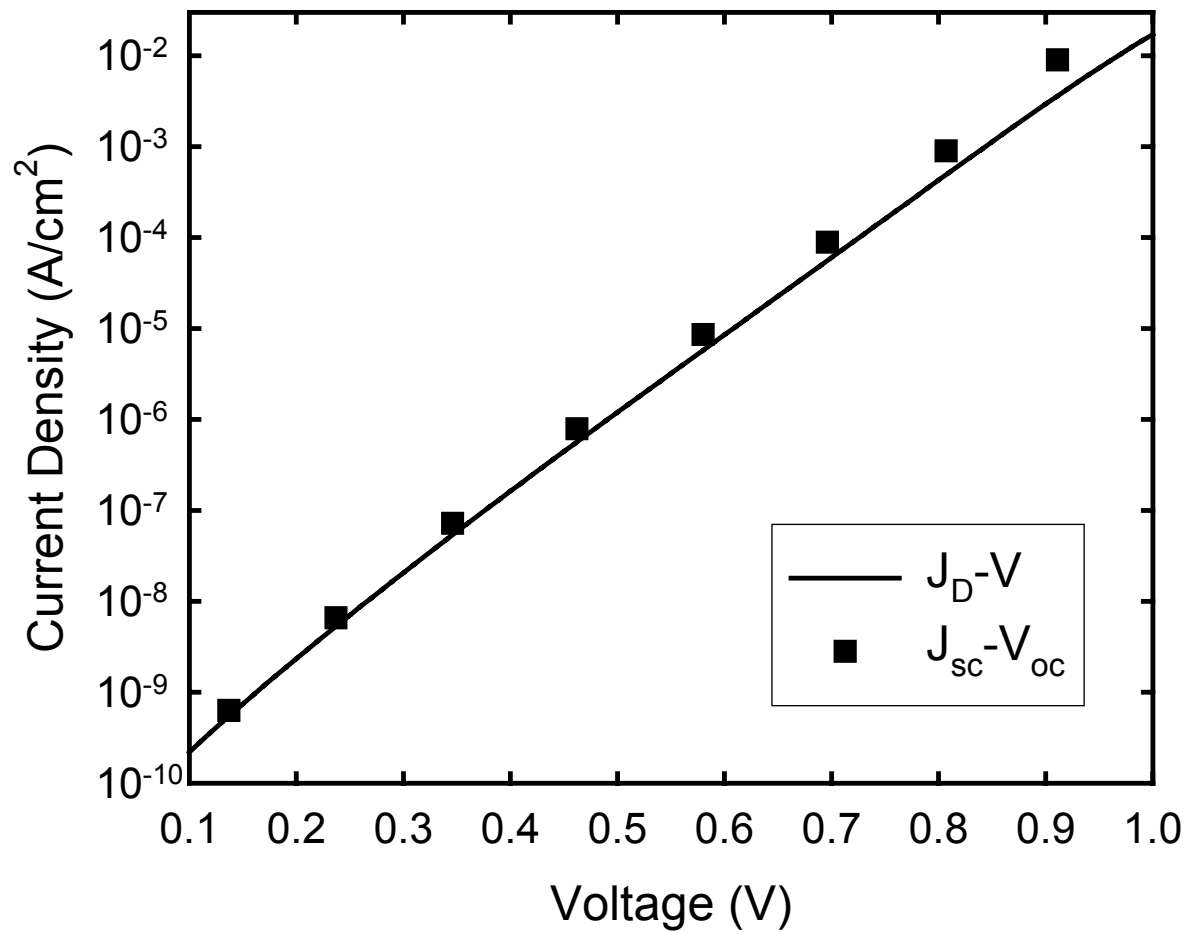


**Figure 28.** Simulated  $J_{sc}-V_{oc}$  and  $J_D-V$  characteristics of a p-i-n cell in Fig. 26 but with  $N_D$ ,  $N_A$  capture cross-sections 40 times higher.

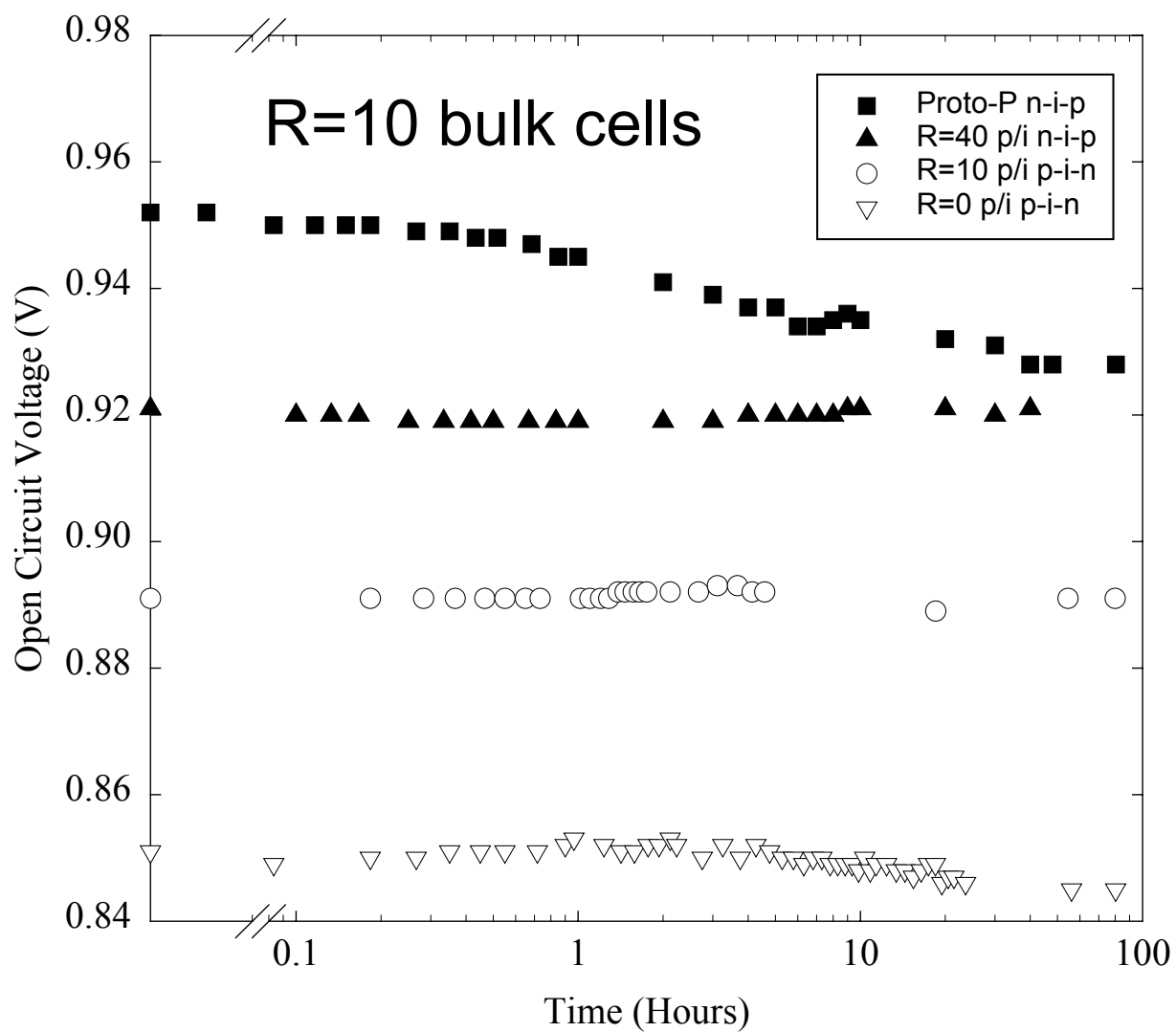


**Figure 29.** Open circuit voltage as a function of 1 sun illumination time for R=10 bulk p a-SiC:H p-i-n cells with R=0, R=10, and R=40 p/i interfaces and a p protocrystalline Si:H n-i-p cell.

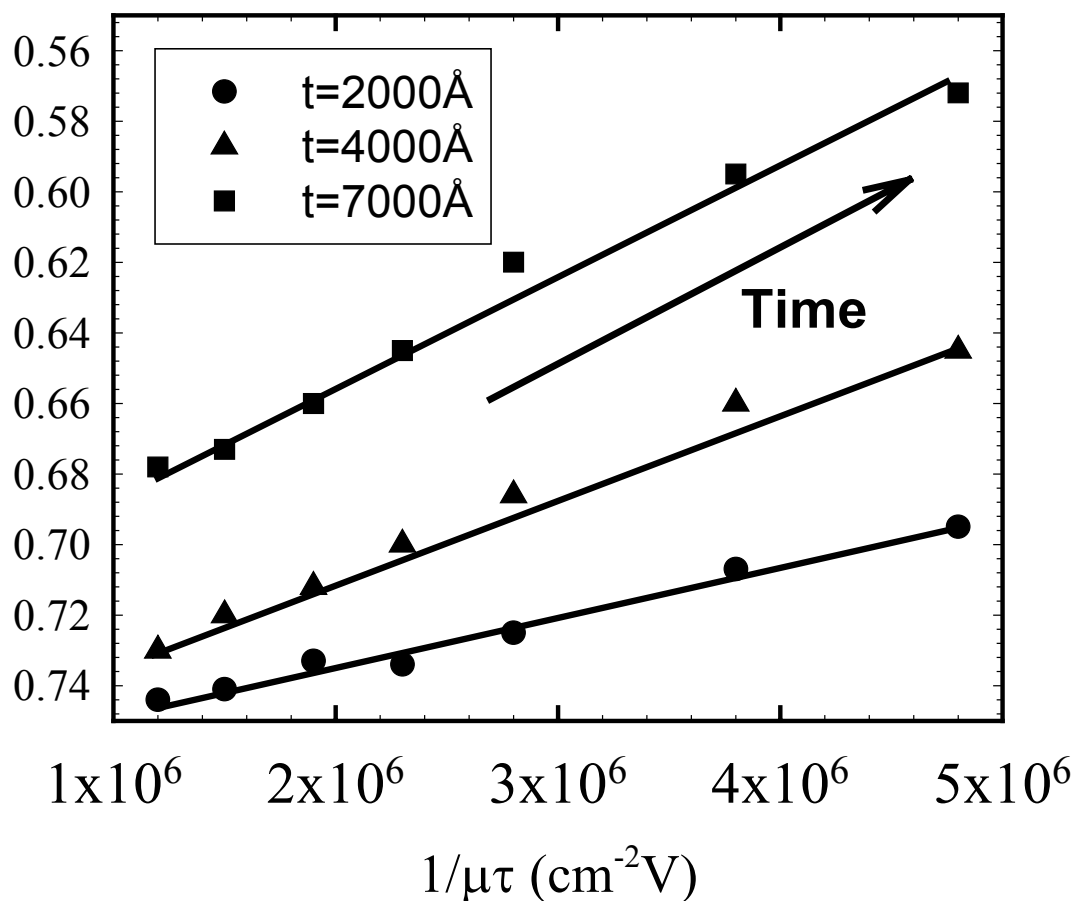


**Figure 30.** The relationship of  $1/\mu\tau$  for an  $R=10$  film to the fill factors of the corresponding p-i-n solar cells with i layer thicknesses of 0.2, 0.4, 0.7  $\mu\text{m}$ . Degradation is performed under 1 sun illumination at  $25^\circ\text{C}$ .

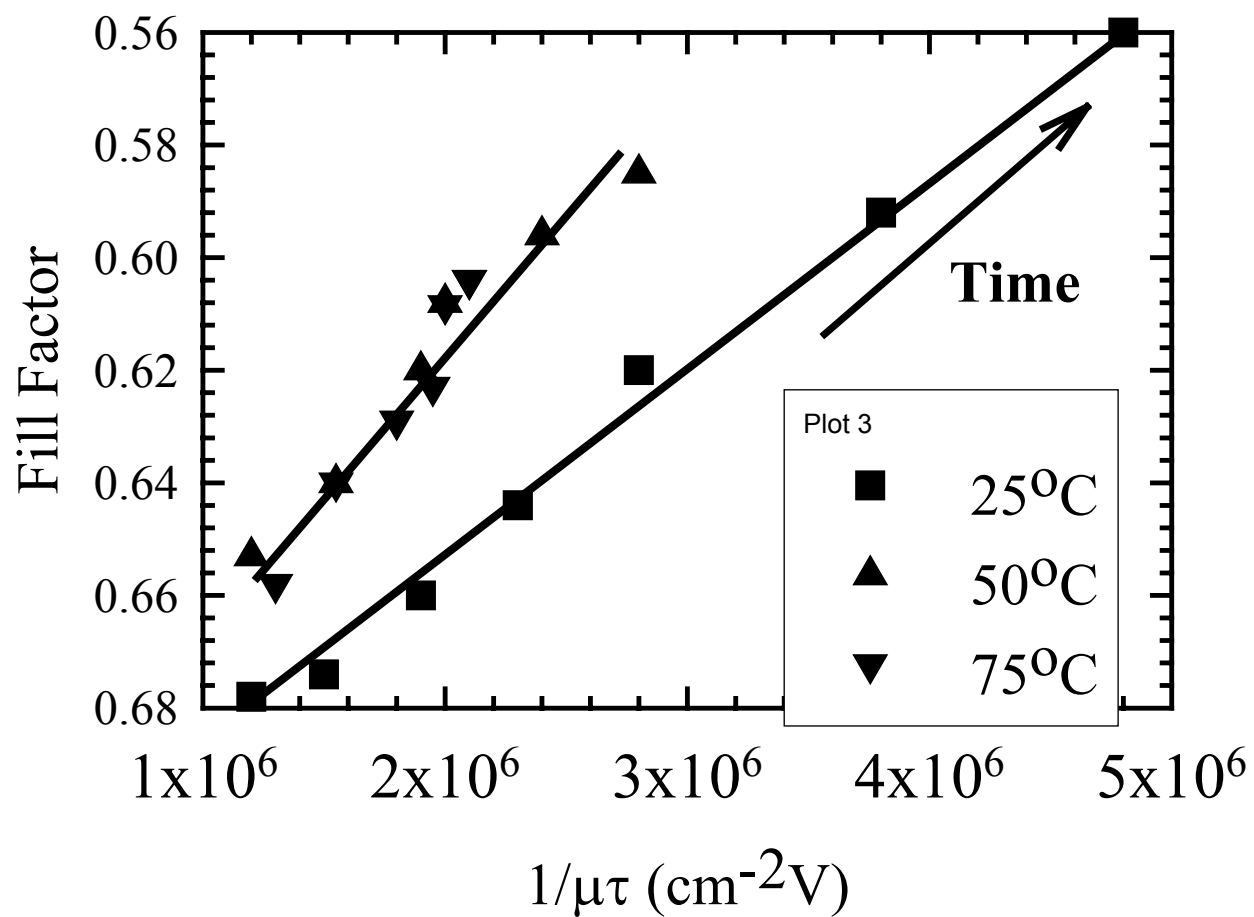


**Figure 31.** The relationship of  $1/\mu\tau$  for an R=10 film to the fill factors of the corresponding p-i-n solar cell with a  $0.7\mu\text{m}$  i layer. Degradation is performed under 1 sun illumination at 25, 50 and 75°C.

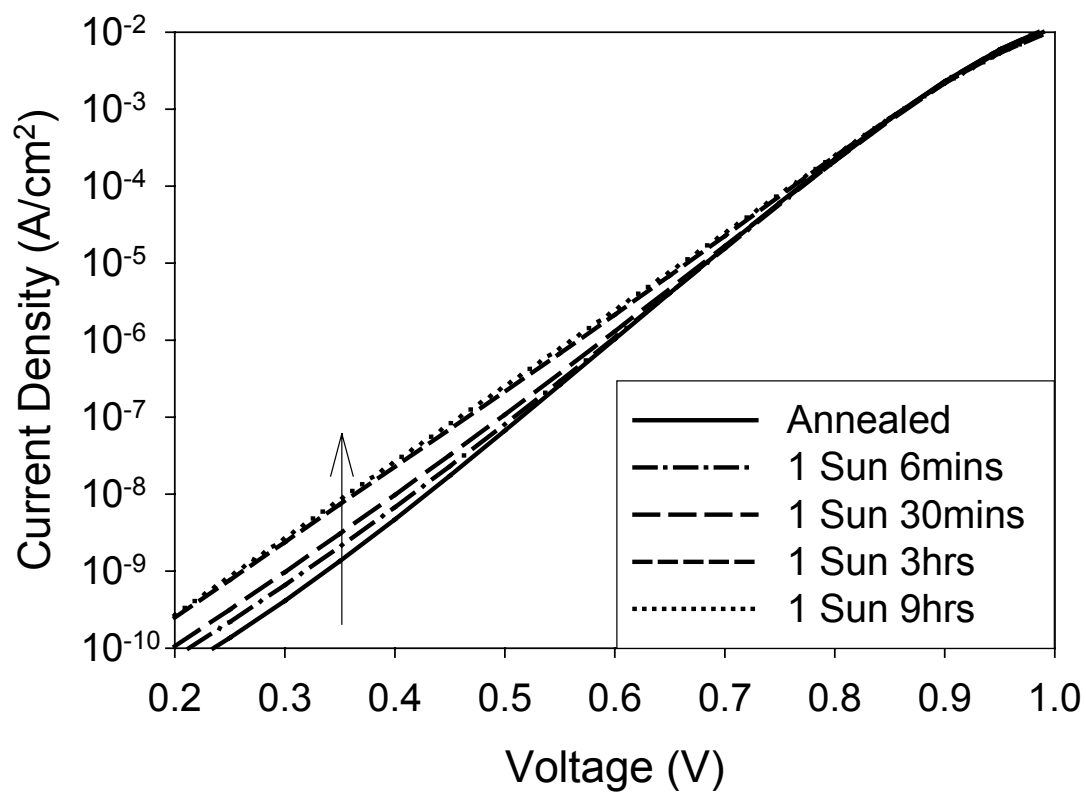


**Figure 32.**  $J_D$ -V characteristics for a p-i-n cell with R=10 i-layer at its annealed state and after 1 sun degradation.

## Task 4

### Novel Analysis of RTSE applied to Amorphous-to-Microcrystalline Phase Transition Region

For thin films based on a-Si:H, researchers have established an effective procedure for obtaining optimum i-layers by rf plasma-enhanced chemical vapor deposition (PECVD) for incorporation into the highest performance, highest stability p-i-n and n-i-p solar cells<sup>43,44,45</sup>. In this procedure, the maximum possible H<sub>2</sub>-dilution ratio  $R=[H_2]/[SiH_4]$  is employed, but without crossing the amorphous-to-(mixed-phase microcrystalline) boundary [a→(a+μc)] that is inevitably encountered above a certain value of R, depending on the other PECVD conditions. Subsequently, it has been found that with this optimization principle, the film microstructure and phase may evolve with thickness and may depend sensitively on the substrate, particularly if the value of R is set too high or the film is grown too thick<sup>46,47</sup>. Because of the possible dependence of the film properties on the accumulated thickness during growth and because of the graded nature of the final film, it is difficult to optimize the deposition procedure by trial-and-error. Under these conditions, real time analysis of film growth is of great utility to the researcher.

In this study, we describe the use of deposition phase diagrams, deduced by real time spectroscopic ellipsometry (RTSE), as conceptual tools for the optimization of the component layers of a-Si:H-based solar cells. Such phase diagrams are also expected to be useful in the fabrication of the components of μc-Si:H solar cells, since the optimum conditions for these materials are often defined relative to the (a+μc)→μc phase boundary in parameter space<sup>48</sup>.

### Analysis of the Evolution of (a+μc)-Si:H films

The conventional two-layer [(uniform bulk)/(surface roughness)] optical model used in RTSE data analysis is no longer correct once the film traverses the phase boundary from the single-phase amorphous (protocrystalline) Si:H growth regime into the mixed-phase (a+μc)-Si:H regime. In order to extract the volume fraction of μc-Si:H in the graded mixed-phase regime, it is easiest to track the dielectric function of the top-most growing material throughout the film deposition. This is an ideal application for the virtual interface (VI) approach to RTSE data analysis<sup>49</sup>. Figures 33-35 depict the final results of such an analysis.

Figure 33 compares the (a) real and (b) imaginary parts of the dielectric functions ( $\epsilon_1$ ,  $\epsilon_2$ ) for the pure phases obtained in analyses of RTSE data acquired during the deposition of an R=20 Si:H film on a c-Si substrate. This film evolves from single-phase a-Si:H to mixed-phase (a+μc)-Si:H and then to single-phase μc-Si:H throughout growth

<sup>43</sup> Y. Lu, S. Kim, M. Gunes, Y. Lee, C.R. Wronski, and R.W. Collins, *Mater. Res. Soc. Symp. Proc.* **336**, 595 (1994).

<sup>44</sup> D.V. Tsu, B.S. Chao, S.R. Ovshinsky, S. Guha, and J. Yang, *Appl. Phys. Lett.* **71**, 1317 (1997).

<sup>45</sup> J. Koh, Y. Lee, H. Fujiwara, C.R. Wronski, and R.W. Collins, *Appl. Phys. Lett.* **73**, 1526 (1998).

<sup>46</sup> J. Koh, A.S. Ferlauto, P.I. Rovira, C.R. Wronski, and R.W. Collins, *Appl. Phys. Lett.* **75**, 2286 (1999).

<sup>47</sup> J. Yang, K. Lord, S. Guha, and S.R. Ovshinsky, *Mater. Res. Soc. Symp. Proc.* **609**, A15.4 (2000).

<sup>48</sup> O. Vetterl, F. Finger, R. Carius, P. Hapke, L. Houben, O. Kluth, A. Lambertz, A. Muck, B. Rech, and H. Wagner, *Sol. Energy Mater. Sol. Cells* **62**, 97 (2000).

<sup>49</sup> H. Fujiwara, J. Koh, C.R. Wronski, and R.W. Collins, *Appl. Phys. Lett.* **70**, 2150 (1997).

to 2300 Å in thickness. The dielectric function of the pure a-Si:H phase in Fig. 33 was determined by applying the conventional two-layer (uniform bulk)/(roughness) model to analyze the RTSE data collected in the protocrystalline Si:H growth regime  $0 < d_b < 200$  Å, before the onset of the  $a \rightarrow (a+\mu c)$  transition. The dielectric function of the pure  $\mu c$ -Si:H phase in Fig. 33 was obtained from data collected after crystallite contact, i.e., during coalescence ( $d_b > 1900$  Å). In this latter case, only the top  $\sim 200$  Å of the film was analyzed, also by applying a two-layer growth model (bulk)/(roughness). In this case, however, the complicated history of the underlying graded layer is buried within a fictitious uniform substrate [or pseudo-substrate] located beneath a fictitious interface [or virtual interface]. The correct surface roughness layer thicknesses -- required in order to extract the  $(\epsilon_1, \epsilon_2)$  spectra of Fig. 33 -- were determined by applying a global error minimization routine within which the entire VI analysis was embedded. The differences between the two dielectric functions in Fig. 33 support an interpretation in terms of phase evolution during film growth. The solid lines in Fig. 33 represent best fit analytical models for the two dielectric functions.

Figure 34 shows the evolution of the volume fraction of  $\mu c$ -Si:H in the R=20 film of Fig. 33 throughout the growth regime starting from the  $a \rightarrow (a+\mu c)$  transition and ending near the  $(a+\mu c) \rightarrow \mu c$  transition. In the analysis that led to these results, a two-layer VI model similar to that described in the previous paragraph was applied. This model consists of a pseudo-substrate, incorporating the history of graded layer deposition, a  $\sim 30$  Å thick outerlayer, modeled as a mixture of a-Si:H and  $\mu c$ -Si:H of variable volume fractions  $1-f_{\mu c}$  and  $f_{\mu c}$ , respectively, and a surface roughness layer, modeled as a mixture of the outerlayer material and void with fixed volume fractions of  $1-f_{sv}$  and  $f_{sv}$ , respectively. The dielectric function of the pseudo-substrate is determined as its pseudo-dielectric function (corrected for surface roughness, but not for the graded structure). The dielectric functions of the two layers are determined from their component volume fractions and dielectric functions via the Bruggeman effective medium theory.

Evidently, the evolution of the surface roughness layer thickness  $d_s$  shown in Fig. 35(a) for the deposition of Figs. 33 and 34 provides higher sensitivity to the presence of microcrystallinity, since it reveals an  $a \rightarrow (a+\mu c)$  transition at  $\sim 300$  Å, whereas the  $\mu c$ -Si:H volume fraction in Fig. 34 first extends above zero for  $d_b \sim 700$  Å. The solid line in Fig. 34 is the result for  $f_{\mu c}$  versus  $d_b$  established using a cone model of microcrystallite evolution. Figure 35(b) identifies how this microcrystallite cone model is constructed. In this model, it is assumed that all microcrystalline nuclei originate at the  $a \rightarrow (a+\mu c)$  transition layer thickness [ $\sim 300$  Å, from Fig. 35(a)]. The area density of such nuclei is assumed to be  $N_d$ , and the nuclei are assumed to grow preferentially at the expense of the surrounding a-Si:H phase with a constant, thickness-independent cone angle,  $\theta$ . The cones are assumed to be spherically capped whereby the cap radius  $r$  evolves with bulk layer thickness according to  $r = d_b - d_{b,trans}$ . Applying this geometry,  $N_d$  and  $\theta$  can be deduced from the values of  $\Delta d_b = d_{b,coal} - d_{b,trans}$  and  $\Delta d_s = d_{s,coal} - d_{s,trans}$ . Here,  $d_{b,trans}$  and  $d_{s,trans}$  are the bulk and surface roughness layer thicknesses at the  $a \rightarrow (a+\mu c)$  transition and  $d_{b,coal}$  and  $d_{s,coal}$  are the corresponding values at the  $(a+\mu c) \rightarrow \mu c$  transition. For example, for the deposition of Figs. 33-35, values of  $\theta = 19^\circ$  and  $N_d = 1.1 \times 10^{10} \text{ cm}^{-2}$  are determined.

Figure 36 presents results for the cone angle  $\theta$  and the nucleation density  $N_d$  plotted as a function of the  $a \rightarrow (a+\mu c)$  transition thickness for a series of Si:H films prepared on both c-Si and R=0 a-Si:H substrates under different conditions of  $H_2$ -dilution, plasma power, and substrate temperature. Results deduced solely from RTSE using the approach

of Figs. 33-35 are compared with those from cross-sectional transmission electron microscopy (XTEM) and from atomic force microscopy (AFM). In Fig. 36, the solid and open symbols represent results from this work and from Fujiwara et al.<sup>50</sup>, respectively. Evidently the nucleation density decreases significantly with increasing  $a \rightarrow (a+\mu c)$  transition thickness, yet the crystallite cone angle is nearly constant between  $15^\circ$  and  $20^\circ$ . Figure 36 reveals consistency between the indirect (but real time) optical measurements and the direct (but ex situ) structural measurements, providing strong support for the generality of the cone growth model for microcrystallinity as depicted in Fig. 35(b).

## Devices Comparisons

Once the film traverses the phase boundary from the protocrystalline Si:H growth regime into the mixed-phase  $(a+\mu c)$ -Si:H growth regime as in the case of the three depositions of Fig. 37, the two-layer [(uniform bulk)/(surface roughness)] optical model used widely for analysis of the RTSE data for purely amorphous films is no longer valid. In order to extract the volume fraction  $f_{\mu c}$  of microcrystalline Si:H in the mixed-phase growth region, it is easiest to track the dielectric function of the top-most growing material throughout the film deposition. This is an ideal application for the two-layer virtual interface (VI) approach to RTSE data analysis. This approach has been described in detail previously.

To demonstrate the outcome of such analyses, Fig. 38 shows  $f_{\mu c}$  vs. depth into the Si:H i-layer for three two-step ( $R=40$  interface)/( $R=20$  bulk) i-layers as they pass through the  $(a+\mu c)$ -Si:H growth regime. The substrates are  $R=0$  a-Si:H films that simulate the underlying p-layers of the p-i-n cell. The structures are distinguished by the thickness  $d_i$  of the  $R=40$  interface i-layer, selected as  $d_i=400$ , 150, or 0 Å, whereas the total i-layer thickness is fixed at 4000 Å. Figure 39 shows results for the dark current-voltage (J-V) characteristics of the corresponding Si:H p-i-n solar cells of this series, i.e., cells having two-step ( $R=40$  interface)/( $R=20$  bulk) i-layers. For the cell with the highest currents in Fig. 38 (inverted triangles, with  $d_i=400$  Å), the associated two-step i-layer structure measured by RTSE exhibits the  $a \rightarrow (a+\mu c)$  transition after 200 Å of  $R=40$  deposition and the  $(a+\mu c) \rightarrow \mu c$  transition after 950 Å of total i-layer deposition (see Fig. 38). For comparison purposes, the cell with the lowest currents in Fig. 39 (squares) was fabricated using the optimum two-step ( $R=40$  interface)/( $R=10$  bulk) a-Si:H i-layer (hereafter designated the "optimum cell").

Computer simulations of the J-V characteristics for these cells were also carried out, and the results are shown in Fig. 39 as the solid lines. The optimum cell could be considered in terms of a uniform a-Si:H i-layer with a mobility gap of 1.86 eV. Results for the other three cells on the other hand were modeled assuming an a-Si:H i-layer at the p/i interface with the same mobility gap as the i-layer of the optimum cell and a bulk  $\mu c$ -Si:H i-layer with a mobility gap of 1.15 eV. This simple model for the solar cells reproduces the overall features of the J-V curves. Table II includes a comparison of the RTSE and J-V simulation results for the three Si:H p-i-n solar cells with two-step ( $R=40$ )/( $R=20$ ) 4000 Å i-layers of Figs. 38 and 39. The table compares the thickness of the a-Si:H i-layer component nearest the p/i interface, as deduced from the device modeling, with the i-layer thickness required to reach a microcrystalline Si:H volume fraction of  $f_{\mu c} = 0.2$ , as deduced from RTSE. This value was chosen because it gave the

<sup>50</sup> H. Fujiwara, Y. Toyoshima, M. Kondo, and A. Matsuda, *Phys. Rev. B* **60**, 13598 (1999)

best overall agreement with the device modeling results (which exhibit quite large error bars due to correlation in the simulations). This good agreement suggests that once  $f_{\mu c}$  approaches  $\sim 0.2$ , transport is dominated by the microcrystalline phase.

### Phase Diagrams for p-Type Doped Si:H Films

Deposition phase diagrams can also be developed for doped Si:H films. The p-type films are of great interest owing to the sensitive effects of the structure and properties of the p-layer on the open circuit voltage of the solar cell as discussed in Task 1. The details of the development of these diagrams are similar to those for the i-layers as described in Task 2 and so only the final results will be presented here.

Figure 40 provides the deposition phase diagram for p-type Si:H prepared with a doping gas flow ratio of  $D=[BF_3]/[SiH_4]=0.2$  on top of  $R=0$  a-Si:H, a structure intended for incorporation in n-i-p solar cells. The diagram in Fig. 40 includes both the  $a \rightarrow (a+\mu c)$  transition (solid line) and the  $(a+\mu c) \rightarrow \mu c$  transition (broken line). The doping level was set at  $D=0.2$  in this case in order to achieve high conductivity, not only in single-phase  $\mu c$ -Si:H films, but also in the protocrystalline Si:H films. The superimposed phase diagram in Fig. 40 for undoped Si:H prepared under otherwise identical conditions demonstrates that doping shifts the transition boundaries to much higher  $R$  values and thicknesses, apparently due to the incorporation of boron in the p-layer. Figure 40 shows that the optimum (maximum  $R$ ) protocrystalline Si:H in a 200 Å doped layer is obtained at  $R=150$  (solid vertical arrow). In contrast, single-phase  $\mu c$ -Si:H cannot be obtained immediately even at  $R=200$ .

Figure 41 shows  $V_{oc}$  plotted as a function of  $R$  for solar cells incorporating  $D=0.2$  p-layers (open squares) prepared in the same way as those in Fig. 40, along with the results for solar cells with  $D=0.1$  p-layers (closed circles)<sup>51</sup>. A comparison of the phase diagram in Fig. 16 with the corresponding results in Fig. 41 for  $D=0.2$  shows that the optimum p-layer deposition is clearly within the protocrystalline Si:H regime. Thus, the optimization principle for p-layers is the same as that established for i-layers. Specifically, the p-layer should be deposited at the maximum  $R$  value possible without crossing the  $a \rightarrow (a+\mu c)$  transition for the desired p-layer thickness.

The continuous decrease in  $V_{oc}$  for the n-i-p solar cells with p-layers deposited at  $D=0.1$  in Fig. 41 contrasts with the behavior for  $D=0.2$ . This decrease may arise from a shift to lower  $R$  in the  $a \rightarrow (a+\mu c)$  transition such that all p-layers with  $D=0.1$  and  $R > 50$  are mixed-phase  $(a+\mu c)$ -Si:H having increasing volume fraction of microcrystallinity with increasing  $R$ . Ex situ SE measurements of the  $D=0.1$ ,  $R=100$  p-layer in the actual n-i-p device configuration, however, show that this layer is fully amorphous and so this first explanation cannot be valid. Alternatively, the decrease in  $V_{oc}$  may be attributed to a decrease in the conductivity and an increase in the conductivity activation energy with  $R$  due to insufficient doping that is observed only in the protocrystalline Si:H growth regime. Such an effect is supported by direct conductivity measurements of 200 Å p-layers with  $D=[BF_3]/[SiH_4]=0.1$  in selected i/p structures. Based on this effect, one can conclude that even higher  $V_{oc}$  values than the optimum in Fig. 41 may be possible in depositions that combine higher  $D$  and  $R$  values than 0.2 and 150, respectively.

Figure 42 shows the extended phase diagram for the deposition of p-type Si:H with  $D=[B(CH_3)_3]/[SiH_4]=0.02$  on ZnO-coated glass, a structure intended for incorporation in

<sup>51</sup> R.J. Koval, C. Chen, G.M. Ferreira, A.S. Ferlauto, J.M. Pearce, P.I. Rovira, C.R. Wronski, and R.W. Collins, *Appl. Phys. Lett.* **81**, 1258 (2002).

p-i-n solar cells<sup>52</sup>. The diagram in Fig. 42 includes both the  $a \rightarrow (a+\mu c)$  transition (solid line) and the  $(a+\mu c) \rightarrow \mu c$  transition (broken line). In this case, ZnO is used as the transparent conducting substrate film rather than the more conventional SnO<sub>2</sub> since the former is much more resistant to reduction by atomic H and H<sub>2</sub> ions in the plasmas used for the deposition of  $(a+\mu c)$ -Si:H and  $\mu c$ -Si:H at high R values. The doping level was set to obtain a high conductivity [ $>0.01 (\Omega \text{ cm})^{-1}$ ] and low activation energies [ $<0.1 \text{ eV}$ ] in 200-300 Å p-layers deposited at high R (R=200) on R=0 a-Si:H substrate films in a process designed such that microcrystallite nucleation is immediate. In Fig. 42, the transition lines are shifted to much higher thickness and R compared to those for undoped a-Si:H. In this case, the shift can be attributed to the incorporation of both boron and carbon from the dopant gas which suppresses the nucleation of microcrystallites. Figure 42 further shows that protocrystalline Si:H in a 200 Å doped layer can be obtained at R=100-120. Based on the comparisons of Figs. 40 and 41, this is expected to be the desired R for the p-layers of p-i-n cells prepared with D=0.02; however, higher values of D may be required for effective p-type doping in the protocrystalline growth regime.

### New Dual Beam Photoconductivity Apparatus

Up to now the studies at Penn State utilized a dual beam photoconductivity apparatus which allows the probing of gap states up to 0.8eV from the conduction band. It is thus only able to obtain information about the defects at and below midgap in diluted and undiluted a-Si:H. A new dual beam photoconductivity apparatus is being constructed. This DBP apparatus will allow gap states to be probed well above midgap of a-Si:H as well as allow the study of a-SiGe:H alloy materials. A schematic of this apparatus is shown in Figure 43.

---

<sup>52</sup> P.I. Rovira, A.S. Ferlauto, R.J. Koval, C.R. Wronski, R.W. Collins, and G. Ganguly, *Mater. Res. Soc. Symp. Proc.* **609**, A19.6 (2000).

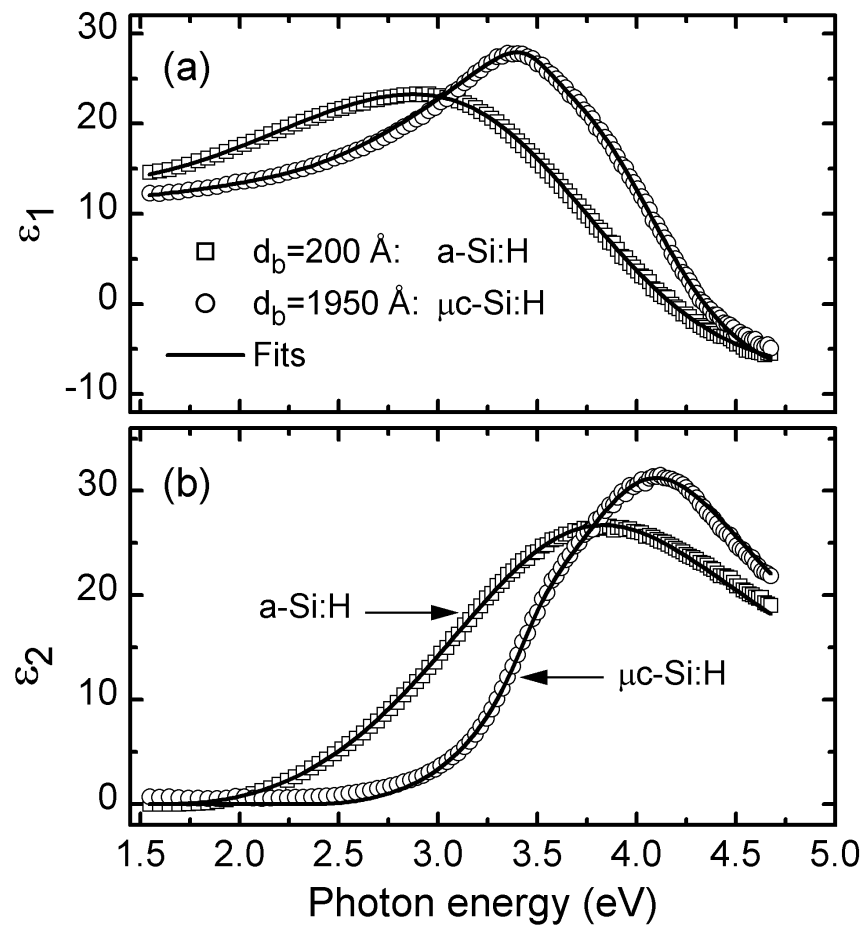


**Figure 33.** (a) Real and (b) imaginary parts of the dielectric functions of the pure phases for an R=20 Si:H deposition on c-Si. The solid lines are fits using analytical models for the dielectric functions.

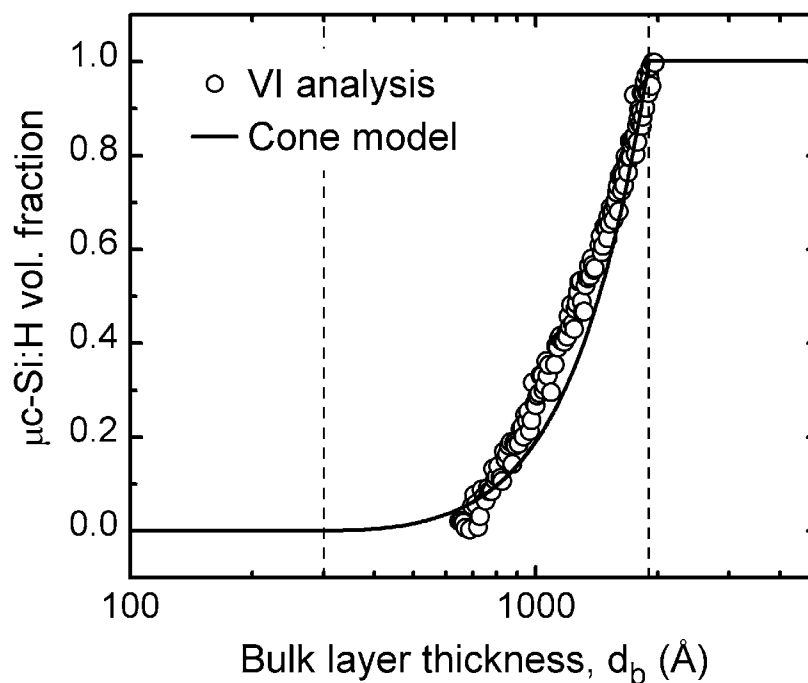


**Figure 34.** Depth profile in the volume fraction of the microcrystalline phase throughout the mixed-phase (a+ $\mu$ c)-Si:H growth regime for the R=20 Si:H deposition on c-Si from Fig. 35 (points). In order to extract the volume fraction of  $\mu$ c-Si:H, the dielectric function of the top-most growing material was tracked throughout the film deposition. Also shown as the solid line is the prediction of the microcrystallite cone growth model depicted in Figure 35.

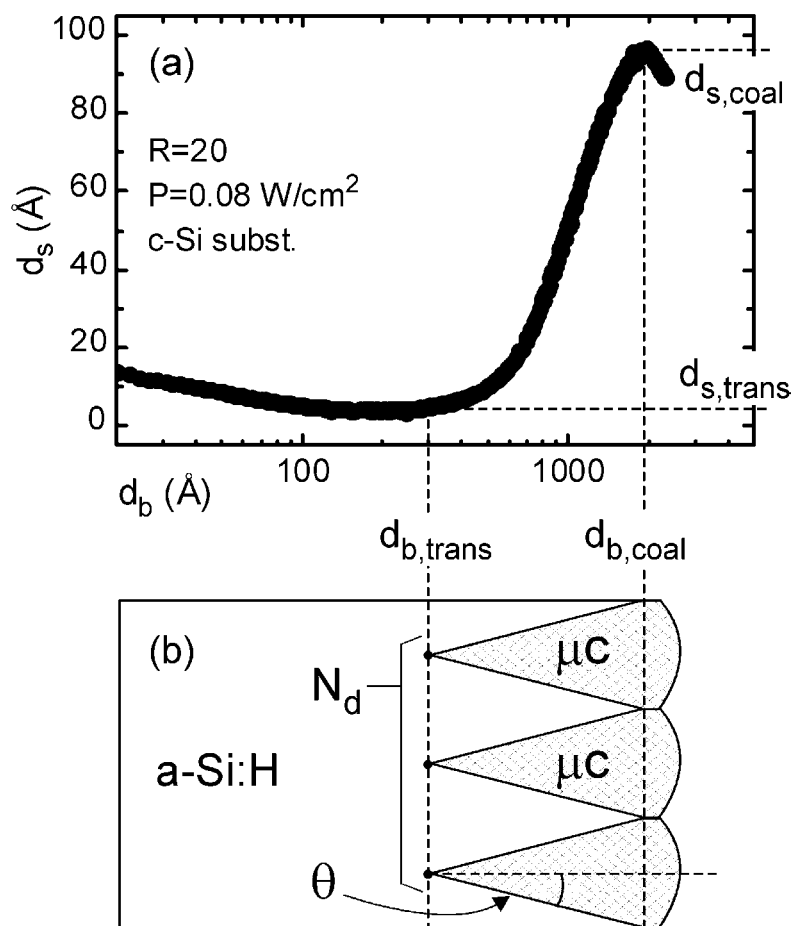


**Figure 35.** (a) Surface roughness thickness versus bulk layer thickness for the  $R=20$  Si:H deposition of Figs. 34 and 35; (b) schematic of the cone growth model used to estimate the microcrystallite nuclei density and cone angle.

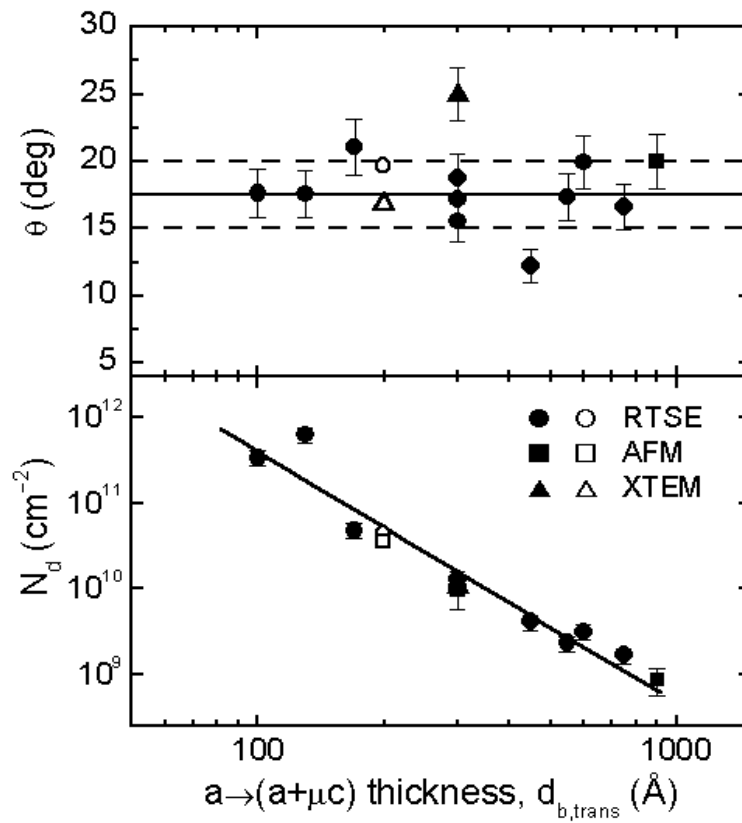


**Figure 36.** Cone angle  $\theta$  (top panel) and nucleation density  $N_d$  (bottom panel) versus the  $a \rightarrow (a+\mu c)$  transition thickness  $d_{b,trans}$  for Si:H films deposited under different conditions on both c-Si wafers and R=0 a-Si:H. The values for  $\theta$  and  $N_d$  are deduced from RTSE (circles), XTEM (triangles) and AFM (squares).

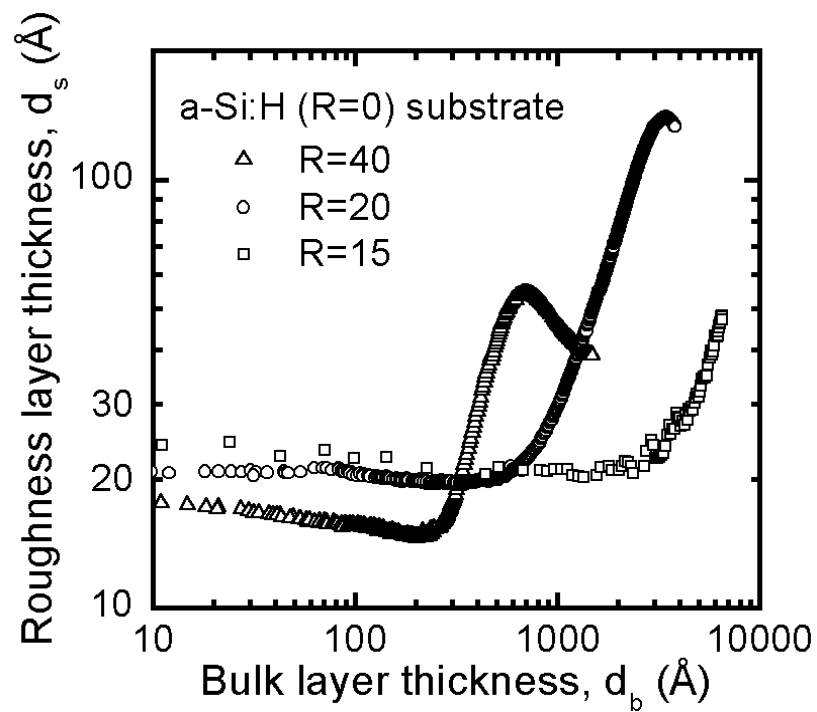


**Figure 37.** Surface roughness layer thickness ( $d_s$ ) versus bulk layer thickness ( $d_b$ ) extracted in analyses of RTSE data collected during the deposition of Si:H with  $R=15$ , 20, and 40, all on  $R=0$  a-Si:H substrate films.

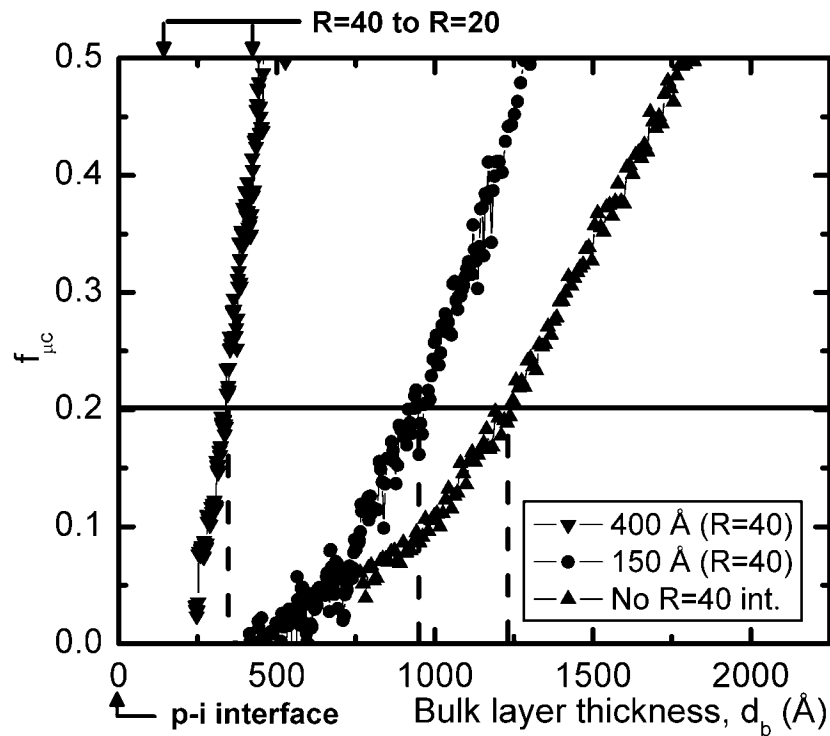


**Figure 38.** Evolution of the microcrystalline Si:H volume fraction  $f_{\mu c}$  in the i-layer for 4000 Å two-step R=40/20 i-layer structures on R=0 a-Si:H substrates. The thicknesses  $d_i$  of the R=40 p/i interface layer are  $d_i=400$ , 150, and 0 Å.

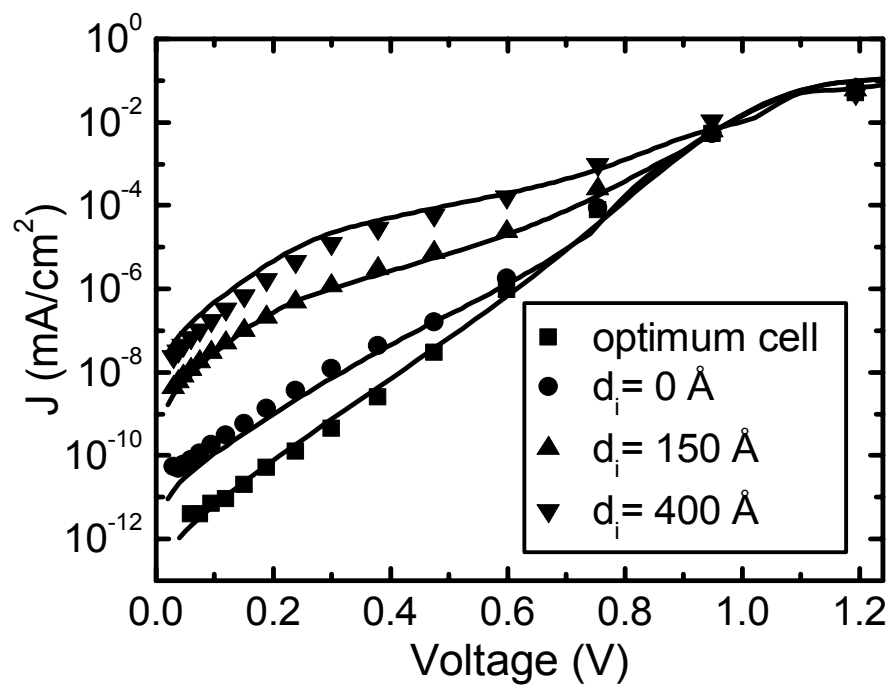


**Figure 39.** Experimental (symbols) and simulated (lines) dark J-V characteristics for four Si:H p-i-n solar cells. The squares denote a standard cell that incorporates an optimized [R=40 (200 Å)]/[R=10 (3800 Å)] a-Si:H i-layer, and the three other cells incorporate [R=40 ( $d_i$ )]/[R=20 (4000- $d_i$ ) Å] Si:H i-layers where  $d_i = 0$  Å (circles), 150 Å (triangles), and 400 Å (inverted triangles) as in Fig. 38.

**Table II.** Correlation of RTSE and device modeling results for p-i-n cells with 4000 Å two-step R=40/20 i-layers in which the R=40 interface thickness is varied.

First step: R=40 thickness (Å)	<b>RTSE:</b> $d_b$ (Å) when $f_{\mu c}=0.2$	<b>Device Modeling:</b> Heterojunction position from p/i (Å)
0	$1240 \pm 30$	$1300 \pm 300$
150	$950 \pm 30$	$700 \pm 200$
400	$330 \pm 20$	$400 \pm 100$

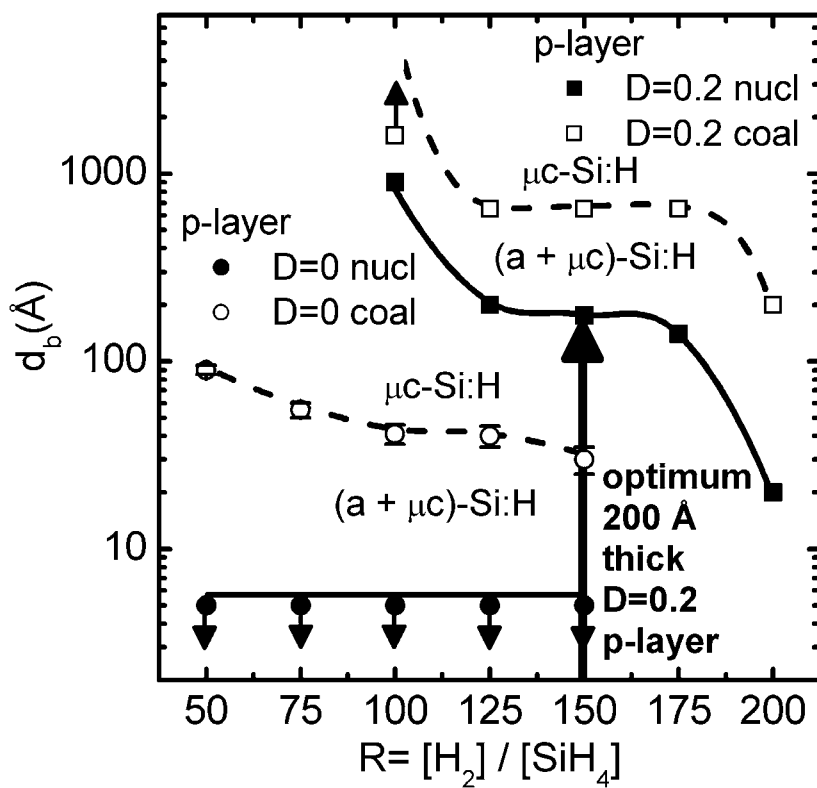


**Figure 40.** Superimposed extended phase diagrams for the deposition of Si:H p-layers on  $R=0$  a-Si:H films held at  $200^\circ\text{C}$ . The doping gas ratio was either  $D=[BF_3]/[SiH_4] = 0.2$  (squares) or  $D=0$  (undoped; circles).

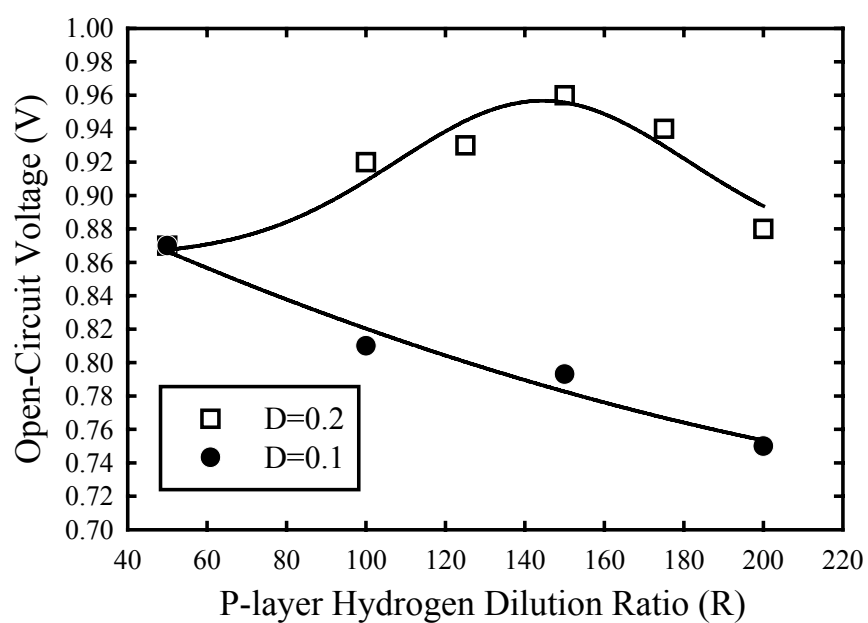


**Figure 41.** Open-circuit voltages of n-i-p cells incorporating  $\sim 200$  Å thick p-layers deposited with variable R. Doping flow ratios of  $D=[\text{BF}_3]/[\text{SiH}_4]=0.1$  or 0.2 were used for the two series, and other conditions matched those of Fig. 40.

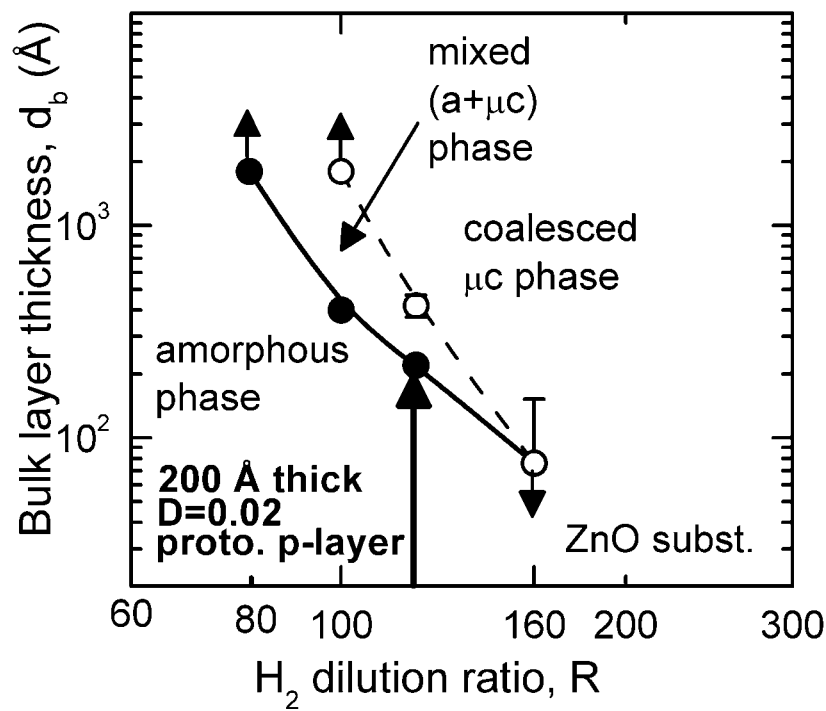


**Figure 42.** Phase diagram for Si:H p-layer deposition on ZnO at 200°C. The doping ratio was  $D=[B(CH_3)_3]/[SiH_4]=0.02$  and the rf power was  $P=0.23 \text{ W/cm}^2$ . The solid and dashed lines identify the  $a \rightarrow (a+\mu c)$  and  $(a+\mu c) \rightarrow \mu c$  transitions.

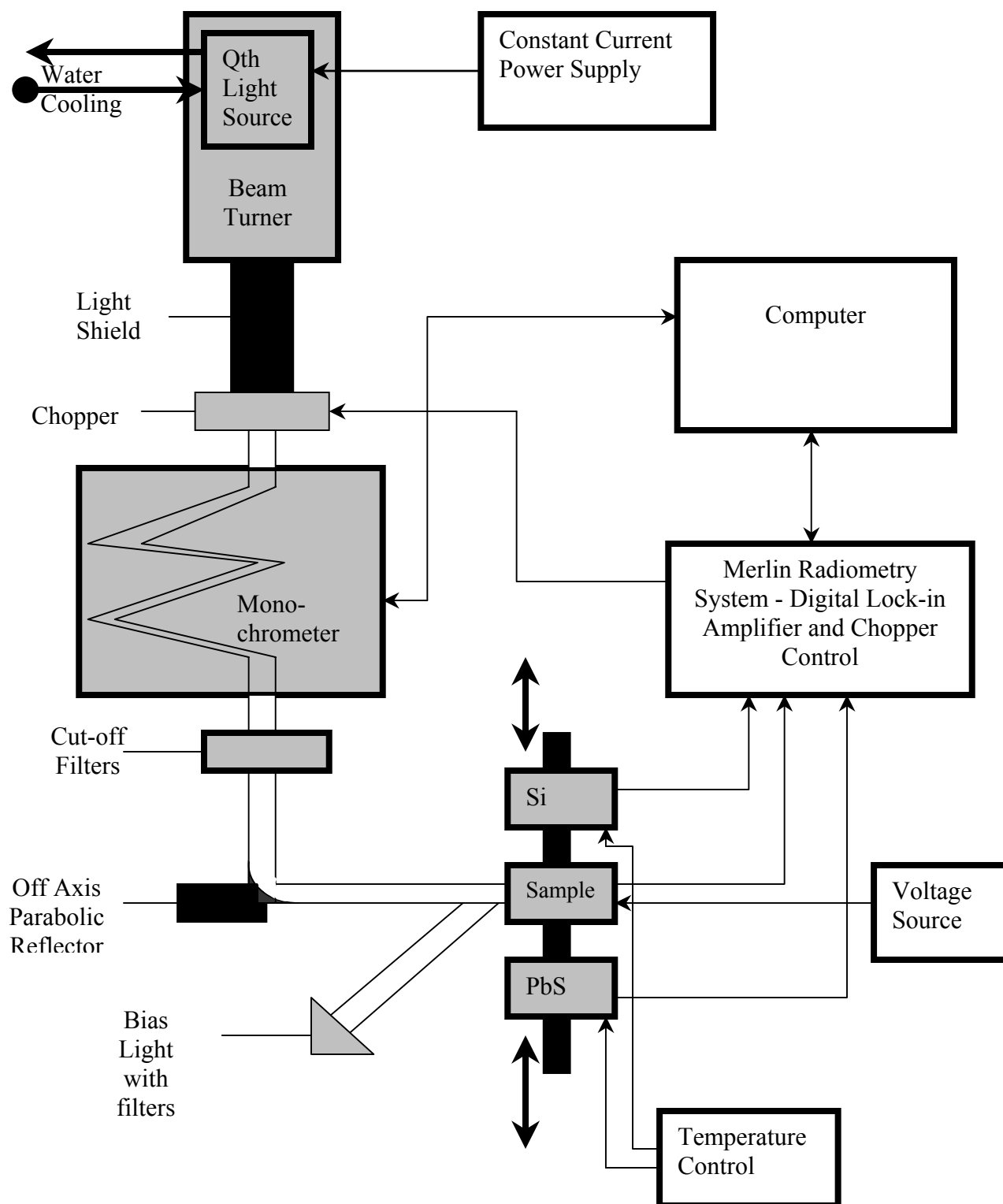


**Figure 43.** Schematic diagram of the new dual beam photoconductivity apparatus

## List of Publications

1. J. M. Pearce, R. J. Koval, X. Niu, S. J. May, R.W. Collins, and C. R. Wronski, "The 'Fast' and 'Slow' Light Induced Defects in Diluted and Undiluted Hydrogenated Amorphous Silicon Solar Cells and Materials", *17<sup>th</sup> European Photovoltaic Solar Energy Conference Proceedings*, 3, pp. 2842-2845, 2002.
2. J. M. Pearce, R. J. Koval, R.W. Collins, C. R. Wronski, M.M. Al-Jassim, and K.M. Jones "Correlation of Light-Induced Changes in a-Si:H Films with Characteristics of Corresponding Solar Cells" *29<sup>th</sup> IEEE Photovoltaic Specialists Conf. Proc.*, (IEEE, 2002) pp. 1098-1101, 2002.
3. R. J. Koval, J. M. Pearce, C. Chen, G. M. Ferreira, A. S. Ferlauto, R. W. Collins, and C.R. Wronski, "Microstructurally Engineered p-layers for Obtaining High Open-Circuit Voltages in a-Si:H n-i-p Solar Cells", *29<sup>th</sup> IEEE Photovoltaic Specialists Conf. Proc.*, (IEEE, 2002) pp. 1090-1093, 2002.
4. R. J. Koval, C. Chen, G. M. Ferreira, A. S. Ferlauto, J. M. Pearce, P. I. Rovira, C. R. Wronski, and R. W. Collins, "Protocrystalline Si:H p-type Layers for Maximization of the Open Circuit Voltage of a-Si:H n-i-p Solar Cells", *Mat. Res. Soc. Proc.* **715**, A6.1, 2002.
5. R. J. Koval, C. Chen, G. M. Ferreira, A. S. Ferlauto, J. M. Pearce, P.I. Rovira, R. W. Collins, and C.R. Wronski, "Maximization of the open circuit voltage for a-Si:H n-i-p solar cells by incorporation of protocrystalline Si:H p-type layers", *Appl. Phys. Lett.*, **81**, 1258-1260, 2002.
6. R. J. Koval, A. S. Ferlauto, J. M. Pearce, R. W. Collins, and C. R. Wronski, "Mobility Gap Profiles in Si:H Intrinsic Layers Prepared by H<sub>2</sub>-Dilution of SiH<sub>4</sub>: Effects on the Performance of p-i-n Solar Cells", *Journal of Non-Crystalline Solids*, 299-302, pp. 1136-1141, 2002.
7. J. Deng, J. M. Pearce, R. J. Koval, V. Vlahos, R.W. Collins, and C. R. Wronski, "Absence of carrier recombination associated with the defect pool model in a-Si:H i-layers: Evidence from current-voltage characteristics on p-i-n and n-i-p solar cells", *Appl. Phys. Lett.* May, 2003 (in press).
8. J. Deng, J. M. Pearce, V. Vlahos, R. W. Collins, and C. R. Wronski, "Carrier Transport and Recombination in a-Si:H p-i-n Solar Cells in Dark and Under Illumination", *Mat. Res. Soc. Proc.* **762**, A3.4, 2003.
9. V. Vlahos, J. Deng, J. M. Pearce, R. J. Koval, R. W. Collins and C. R. Wronski, "Recombination in n-i-p (substrate) a-Si:H Solar Cells with Silicon Carbide and Protocrystalline p-layers", *Mat. Res. Soc. Proc.* **762**, A7.2, 2003.
10. C. R. Wronski, J. M. Pearce, R. J. Koval, X. Niu, A. S. Ferlauto, J. Koh, and R. W. Collins "Light Induced Defect Creation Kinetics in Thin Film Protocrystalline Silicon Materials and Their Solar Cells" *Mat. Res. Soc. Proc.* **715**, A13.4, 2002.
11. C. R. Wronski, J. M. Pearce, R. J. Koval, A. S. Ferlauto, and R. W. Collins, "Progress in Amorphous Silicon Based Solar Cell Technology", *Proceedings of Rio 2002: World Climate and Energy Event*, pp. 67-72, 2002.
12. C. R. Wronski, J. M. Pearce, R. J. Koval, A. S. Ferlauto, and R. W. Collins, "Advances in Amorphous Silicon Solar Cells", *5<sup>th</sup> Sanken International Symposium – Frontier Material Science Towards Energy Conversion and Ecological Design*, pp. 5-6, Osaka, 2002.
13. C. R. Wronski, R. W. Collins, J. M. Pearce, J. Deng, V. Vlahos, G. M. Ferreira, and C. Chen, "Optimization of Phase-Engineered a-Si:H-Based Multijunction

- Solar Cells”, *National Center for Photovoltaics Program Review Proceedings*, February 2003.
14. A. S. Ferlauto, G. M. Ferreira, J. M. Pearce, C.R. Wronski, R. W. Collins, X. Deng, and G. Ganguly, “Analytical model for the optical functions of amorphous semiconductors from the near-infrared to ultraviolet: Applications in thin film photovoltaics”, *J. of Appl. Phys.*, **92**, 2424-2436, 2002.
  15. A. S. Ferlauto, R. J. Koval, C. R. Wronski, and R. W. Collins, "Extended Phase Diagrams for Guiding Plasma-Enhanced Chemical Vapor Deposition of Silicon Thin Films for Photovoltaic Applications", *Appl. Phys. Lett.* **80**, 2666-2668 (2002).
  16. A. S. Ferlauto, R. J. Koval, C. R. Wronski, and R. W. Collins, "Phase Diagrams for Si:H Film Growth by Plasma-Enhanced Chemical Vapor Deposition", *Journal of Non-Crystalline Solids*, **299**, 68-73 (2002).
  17. A. S. Ferlauto, G.M. Ferreira, R.J. Koval, J.M. Pearce, C.R. Wronski, R. W. Collins, M.M. Al-Jassim, and K.M. Jones, “Thickness Evolution of the Microstructural and Optical Properties of Si:H Films in the Amorphous-to-Microcrystalline Phase Transition Region” *29<sup>th</sup> IEEE Photovoltaic Specialists Conf. Proc.*, (IEEE, 2002) pp. 1076-1081, 2002.
  18. A.S. Ferlauto, G.M. Ferreira, R.J. Koval, J. M. Pearce, C.R. Wronski, and R.W. Collins, “Evolution of Crystallinity in Mixed-phase (a+ $\mu$ c)-Si:H as Determined by Real Time Ellipsometry”, *Mat. Res. Soc. Proc.* **762**, A5.10, 2003.
  19. G. M. Ferreira, C. Chen, I. An, C. R. Wronski, R. W. Collins, G. Ganguly, J. H. Kwak, and K. S. Lim, "Optical Functions of Transparent Conductors and their Impact on Collection in Amorphous Silicon Solar Cells", *Mat. Res. Soc. Proc.* **762**, A14.5, 2003
  20. C. Chen, I. An, J. A. Zapien, and R. W. Collins, "Analysis of Optical Anisotropy in Reflecting Surfaces by Multichannel Mueller Matrix Ellipsometry", *Optics Letters* (submitted, 2003).
  21. C. Chen, I. An, and R. W. Collins, "Multichannel Mueller Matrix Ellipsometry for Simultaneous Real Time Measurement of Bulk Isotropic and Surface Anisotropic Complex Dielectric Functions of Semiconductors", *Phys. Rev. Lett.* (submitted, 2003).
  22. R. W. Collins, A.S. Ferlauto, G.M. Ferreira, Chi Chen, R.J. Koval, J.M. Pearce, and C.R. Wronski, “Application of Deposition Phase Diagrams for the Optimization of a-Si:H Based Materials and Solar Cells”, *Mat. Res. Soc. Proc.* **762**, A10.1, 2003
  23. R. W. Collins, A. S. Ferlauto, G. M. Ferreira, Chi, Chen, J. Koh, R. J. Koval, Y. Lee, J. M. Pearce, and C. R. Wronski, “Evolution of microstructure and phase in amorphous, protocrystalline, and microcrystalline silicon studied by real time spectroscopic ellipsometry” *Solar Energy Materials and Solar Cells*, (accepted).
  24. R. W. Collins, G.M. Ferreira, J. M. Pearce, A. S. Ferlauto, R. J. Koval, and C. R. Wronski, “Real Time Optics of the Growth of Silicon Thin Films in Photovoltaics: Analysis of the Amorphous-to-Microcrystalline Phase Transition”, *National Center for Photovoltaics Program Review Proceedings*, February 2003.
  25. R. W. Collins and A. S. Ferlauto, "Advances in Plasma-Enhanced Chemical Vapor Deposition of Silicon Films at Low Temperatures", *Current Opinion in Solid State and Material Science*, **6**, 425-437 (2002).

26. R. W. Collins and A. S. Ferlauto, "Optical Physics of Materials", in *Handbook of Ellipsometry*, edited by H. G. Tompkins and E. A. Irene (Noyes, Boston, 2003, in press).
27. R. W. Collins, I. An, J. Lee, and J. A. Zapien "Multichannel Ellipsometry", , in *Handbook of Ellipsometry*, edited by H. G. Tompkins and E. A. Irene (Noyes, Boston, 2003, in press).
28. R. W. Collins, "Ellipsometry", *Optics Encyclopedia* (VCH, New York, submitted, 2003).